A BIOMECHANICALLY BASED ACUTE THORACIC AORTIC DISSECTION POTENTIAL INDEX

by

James R. Thunes

MS Mechanical Engineering, Michigan Technological University,

2011

Submitted to the Graduate Faculty of

the Swanson School of Engineering in partial fulfillment

of the requirements for the degree of

Doctor of Philosophy

University of Pittsburgh

2018

UNIVERSITY OF PITTSBURGH

SWANSON SCHOOL OF ENGINEERING

This dissertation was presented

by

James R. Thunes

It was defended on

April 2, 2018

and approved by

Spandan Maiti, PhD, Assistant Professor, Department of Bioengineering

Steven Abramowitch, PhD, Associate Professor, Department of Bioengineering

James Foulk, PhD, Sandia National Labs

Julie Phillippi, PhD, Assistant Professor, Department of Cardiothoracic Surgery

Anne Robertson, PhD, Professor, Department of Mechanical Engineering

Dissertation Director: Spandan Maiti, PhD, Assistant Professor, Department of Bioengineering

A BIOMECHANICALLY BASED ACUTE THORACIC AORTIC DISSECTION POTENTIAL INDEX

James R. Thunes, PhD

University of Pittsburgh, 2018

Acute thoracic aortic dissection, a separation of the layers of the aortic wall, is a serious medical condition with high mortality. Current clinical practice is a diameter based decision for elective surgery for patients with an orthogonal aortic diameter in excess of 5.5 cm. However, the utility of this metric is limited by the high number of patients experiencing dissection at diameters below this threshold. There thus exists a need for an improved metric for assessing dissection risk. As the dissection event ultimately involves biomechanical failure of the aortic wall, this thesis proposes a biomechanically based dissection potential index derived from both full aorta stress maps and microstructural failure behavior of the tissue. A structural model of the aortic wall, including the repeating lamellar structure of the aortic media was developed. This model was used to determine the aortic tissue biomechanical behavior in both the pre-failure and failure regimes. These model predictions were validated against experimentally determined uniaxial pre-failure elastic response as well as ultimate stress of the vessel wall for three different patient cohorts. The model was next utilized to quantify physiologic strength of the vessel wall subjected to the entire range of physiologically plausible biaxial loading conditions. Interestingly, we discovered that the vessel wall physiologic strength is not statistically different than its uniaxial longitudinal strength. We also found that the biomechanical integrity of the aorta is limited by the longitudinal strength of the aortic wall tissue in regions of high stress biaxiality, defined by the ratio of longitudinal and circumferential stress. We constructed a dissection risk metric, termed dissection potential index (DPI), from the ratio of the longitudinal stress to the longitudinal strength of the

vessel wall. Using patient-specific aorta geometry and aortic stiffness, both determined from clinical CT images of the aorta, the stress map of the aortic wall was evaluated. The dissection potential index (DPI) for these patients was determined by interrogating these maps against cohort-specific longitudinal strength of the tissue. We found that DPI for dissected patients was significantly higher than for an age and BMI matched control cohort. We also observed an increase of the DPI for dissected patients over time. In addition, the model correctly predicted dissection initiation location marked by the surgeons, suggesting that the model captured essential aortic wall failure mechanisms. Surprisingly, the DPI for dissected patients did not correlate with their maximum aortic diameter, demonstrating the limitations of the current diameter based criterion as a predictive risk metric. Further studies with larger cohort of patients will lead to the establishment of DPI as an evidence based clinical metric for early management of dissection potential.

Keywords: collagen network, aorta, aortic dissection, microstructural model, finite element.

TABLE OF CONTENTS

LIST OF TABLES

LIST OF FIGURES

PREFACE

At the beginning of this work it is, I think, fitting to acknowledge some of the people who have made this dissertation a success. Something of this size is not done by a single person and the people who have helped through the process were instrumental in its success, whether their contribution is included in these pages or not. The vast majority of my thanks must go to my advisor, Spandan Maiti. When I first started to consider graduate school, he saw something in me and gave me a chance. From my start during my masters in mechanical engineering at Michigan Tech to here in the Department of Bioengineering at the University of Pittsburgh, I doubt either of us know where this path would lead. I certainly didn't. The walk was not always easy and we took a couple of detours along the way, but somehow through patience, encouragement, and not a small amount of cajolement, we have brought this journal to a close.

I would also like to thank the members of my committee: Drs. Abramowitch, Foulk, Phillippi, and Robertson. Dr, Abramowitch provided a lot of help when I started in the Bioengineering program here at Pitt. Transitioning from mechanical to bioengineering was difficult, but he was always able to explain things in a way that I understood. Dr. Foulk, while I was working with him at Sandia National Labs, was able to take somebody a long way from home and with a daunting task ahead of him and make him shine. I'm sure that my experience at Sandia would not have been half as successful without his guidance. Dr. Phillippi has been instrumental in providing a biological viewpoint on my work. In addition to the experimental data she provided, her insight into the biological aspects of aortic tissue has greatly and will continue to improve any work that I do. Finally I would like to thank Dr. Robertson for her critical questioning of my work. Whenever we met, she was able to suggest improvements or bring up potential problems that I had not considered.

The graduate students and post-docs I have worked with also deserve a hearty thanks. Siladitya Pal, Sameer Damle, Ron Fortunato, Matt Miller, and Gerald Ferrer are only some of the many that have helped me along the way. We have spent a lot of time together over the past years, and all to my benefit. I would also like to acknowledge Alejandro Mota at Sandia National Labs. Like Jay Foulk, he was always willing to sit down and help me with a problem.

Much of the work in my third aim was directly due to the hard work of Drs. Gleason and Emerel. Dr. Gleason was always willing to help improve our work, but Lenny Emerel, as Dr. Gleason's surgical resident, has had an outsized impact on the results in that final chapter. Always willing to answer my surgically naive questions, act as liaison whenever I required more information, and pour through an amazing amount of patient data, he has been an indispensable asset to our work.

It remains only to thank my family. They have been and continue to be supportive throughout this process, although their expressions have become a bit fixed as the years have progressed. Nonetheless, their understanding was what made all of this possible.

1.0 INTRODUCTION

Dissection of the ascending aorta is a disease with high mortality affecting 3-4 per 100,000 people per year [7, 8]. With this condition, a small tear in the intimal layer of the aorta grows radially in the abluminal direction followed by propagation in the longitudinal directions allowing for blood infiltration between the layers of the aortic wall. Mortality in these cases is quite high - 1-1.4% per hour [9], and in excess of 60% after two weeks [10].

Due to the high mortality of patients with aortic dissection, early identification of at-risk patients prior to dissection is of interest. A significant indicator of dissection risk is aortic aneurysm. An aortic aneurysm, defined as an aorta with a diameter in excess of 1.5x the normal diameter, was listed as a contributing cause of 17,215 deaths in the United States in 2009 [11]. Within the University HealthSystem Consortium, a group of more than 100 academic medical centers and affiliates hospitals, 135,000 cases were seen due to aortic aneurysm out of a total of 15 million cases over the five year period from 2003 to 2007 [12]. Additionally, certain populations are known to be at elevated risk. Those with a bicuspid aortic valve (BAV) have a "9-fold increased risk of aortic dissection" with respect to the general population [13]. Genetic connective tissue disorders (such as Marfan's syndrome or Ehlers-Danlos syndrome) are also known to have an increased risk of aortic dissection [14, 15, 16]. Other risk factors for aortic dissection include hypertension [9, 17, 18], gender [19], age [14, 19], and a history of smoking [20].

When deciding whether a surgical intervention is justified, the risk of the surgery must be weighed against the risk of aortic dissection. The current clinical practice is a recommendation of preemptive surgery if the aortic diameter exceeds 5.5 cm [21, 22, 23, 24]. This criterion is based on the sharp increase in dissection and rupture risk of aneurysms with a diameter over 6.0 cm [25, 26]. The recommended diameter is lower for certain high-risk

groups (e.g. 5.0 cm for Marfan's syndrome [21, 22, 27]). Regardless of diameter, surgery is recommended for patients with rapidly growing aneurysms [22].

Aortic diameter may be collected via echocardiogram [28, 12, 29], computed tomography (CT) [30, 12], or magnetic resonance imaging (MRI) [31, 32]. However, there has been growing controversy over the efficacy of the 5.5 cm criterion. Of the patients experiencing aortic dissection or rupture, approximately 60% have and aortic diameter less than the current threshold [33, 34, 35]. This suggests that the current standard is insufficient in predicting dissection and rupture risk. However, recent meta-analysis has suggested that on the basis of aortic diameter alone, the benefits of earlier intervention do not outweigh the increased risk from the surgery [36]. A mechanistic understanding of the dissection and rupture risk is required to address the deficits in the aortic diameter criterion. Biomechanical study of the aorta may provide a more nuance view of the problem. Dissection, at its heart, is a mechanically driven event. Tear propagation in the aortic wall will occur when the *in vivo* stresses exceed the tissue strength. Better understanding of the tissue and *in vivo* loading could allow for more accurate risk assessment.

1.1 CLASSIFICATION OF AORTIC DISSECTION

Aortic dissections are classified by their location in the aorta. Clinically, two major systems are used for classification of aortic dissections: the DeBakey (Figure 1.1a) and Stanford (Figure 1.1b) systems. The figure shows the primary artery (light grey) and the dissected region (dark grey). The location of blood infiltration into the dissected region is shown with arrows. In the DeBakey system, type I dissections are those originating in the ascending aorta and propagating at least to the aortic arch. This type of dissection often propagates significantly farther along the aorta. This is the most common type of aortic dissection (approximately 60% of patients) as well as the most lethal. Type II dissections occur in and are constrained to the ascending aorta and accounts for 10-15% of the total cases. The third type of dissection in the DeBakey system, type III, originate in the descending aorta and

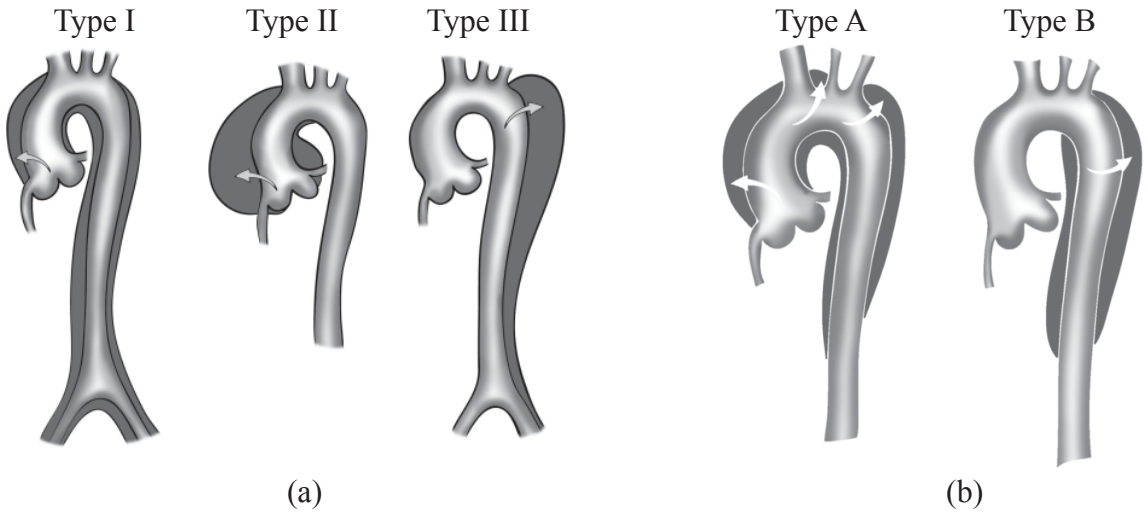

Figure 1.1: (a) The DeBakey dissection classification. (b) The Stanford dissection classification. (reproduced with permission from [3])

primarily propagate distally. Accounting for 25-30% of cases, this is the least lethal of the three types.

Stanford dissections correspond to the dissections in the DeBakey system. Type A dissections for the Stanford system include type I and II from the DeBakey system. Stanford type B dissections are the same as DeBakey type III. The Stanford system is often used to distinguish the type of treatment required. Type A dissections require surgery while type B dissections may be managed pharmacologically in many cases.

Due to the severity of type A dissection (or acute ascending thoracic aortic dissection), this work will focus on this type of dissection.

1.2 ANATOMY OF THE AORTA

Starting from the aortic root (at the heart) and running until it splits into the common illiac arteries, the aorta is the largest artery in the body. The supply of oxygenated blood from

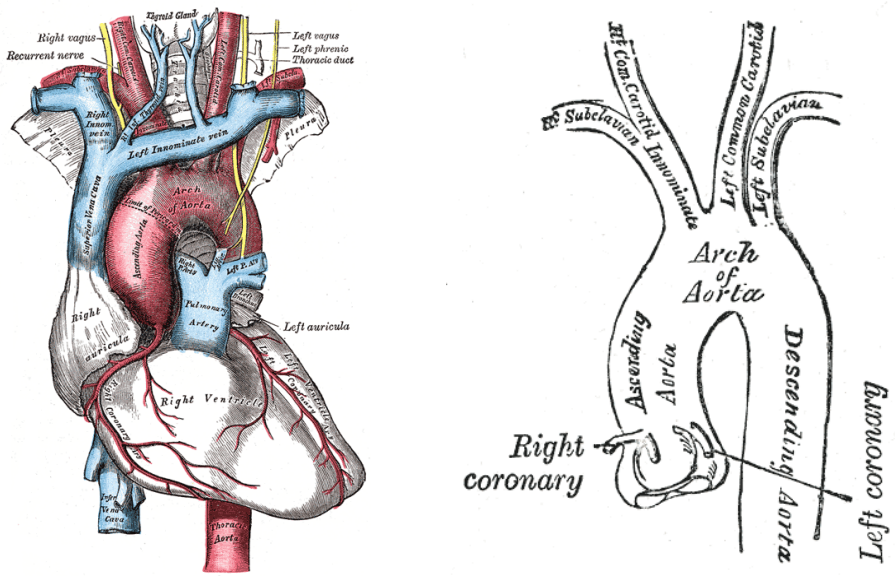

(a) (b)

Figure 1.2: (a) The heart and surrounding vasculature. (b) The thoracic aorta. (from [4])

the left ventricle of the heart flows through the aorta and is then distributed to the rest of the body (Figure 1.2a, shown in red). The aorta may be split into two major regions: the thoracic aorta and the abdominal aorta with the dividing line between the regions being the diaphragm. Superior to the diaphragm is the thoracic aorta and inferior is the abdominal aorta. The thoracic aorta may be further subdivided into the ascending thoracic aorta, the aortic arch and the descending thoracic aorta (Figure 1.2b). The thoracic aorta is approximately 33 cm long (ascending aorta 12 cm) and the abdominal aorta 21 cm. In the healthy population, aortic diameter is approximately 30 mm [37] although this value increases with age at 1-2 mm/year [38].

1.2.1 Aortic valve

The aortic valve is located at the aortic root. During systole, the valve is closed (raising the pressure in the heart as the heart contracts). The valve opens during diastole allowing

blood to flow through the body. Proper function is required for regulation of blood flow. Of the diseases of the aortic valve, the most common are aortic stenosis (narrowing of the valve which increases the force required to pump blood) and aortic regurgitation (in which the valve does not fully close allowing backflow into the heart during systole). Diseases of the aortic valve are of interest in the study of aortic dissection and rupture as they modify the hemodynamics of the aorta and thus may cause deleterious effects in the aortic wall [25, 36]. Of particular interest with regards to aortic dissection and rupture however are the two phenotypes of the aortic valve. Normal aortic valves (tricuspid aortic valves, TAV) are composed of three leaflets aligned with the sinuses of the aortic root. A small portion of the population (1-2% of live births [39]) have an aortic valve in which two of the leaflets are fused. This valve type, known as a bicuspid aortic valve (BAV), is caused by a genetic mutation [40]. In addition to reducing the average age of aortic dissection, bicuspid aortic valves are known to significantly increase the risk of aortic dissection [41].

1.2.2 Ascending thoracic aorta

As the name suggests, the blood in the ascending thoracic aorta travels superiorly from the heart. The start of the aorta, the aortic root, is directly distal to the heart and rises from the left ventricle. Due to the leaflets of the aortic valve, the aorta in this region has three distinct cusps. These cusps, also referred to as the sinuses of Valsalva, split the aorta circumferentially into three approximately equal sections. The sinuses are named after the arteries branching from the aorta in the root. The left and right coronary sinuses are named after the left and right coronary arteries, respectively. No artery branches from the third sinus. For this reason, the third sinus is referred to as the non-coronary sinus. With respect to the aorta, the right and non-coronary sinuses are predominantly aligned with the greater curvature of the aorta while the left coronary sinus is aligned with the lesser curvature. Above the aortic root is the sinotubular junction. In this region, the aorta transitions from the sinus structure of the aortic root to the approximately circular cross-section of the remainder of the aorta. The ascending thoracic aorta is the location of Stanford Type A (DeBakey Type I and II) dissections. The most common location for these types of dissection is near the STJ

and on the greater curvature of the aorta. Distal to the ascending thoracic aorta is the aortic arch, the descending thoracic aorta, and the abdominal aorta. While dissection may occur in these regions (e.g. Type B dissection) this thesis will focus on dissections originating in the ascending thoracic aorta.

1.2.3 Microstructure of the ascending thoracic aorta

As with other soft tissues in the body, the aorta is a complex structure of vascular smooth muscle cells (VSMCs), matrix proteins (including collagen and elastin), and proteoglycans. The aortic wall is composed of three primary layers: the intima, media, and adventitia. The innermost layer, the intima, is an epithelial layer and does not contribute significantly to the load bearing capacity of the aortic wall. In the middle of the aortic wall is the media, composed of a repeating structure called the lamellar unit (LU) [42, 43, 44]. The LU is a layer of smooth muscle cells bounded by networks of collagen and dense sheets of elastin fibers (called elastic lamellae). The number of lamellae in the thoracic aorta is approximately 60 [45, 46]. Lamellar unit thickness is 14 μm[46]. The outermost layer of the aorta (the adventitia) is composed of a dense 3D network of collagen fibers. Total thickness of the aorta (a mean thickness of 2.23 ± 0.48 mm[47]) is approximately 50% media and 50% adventitia with the thickness of the intima significantly less than the other layers.

Of the components of aortic tissue, the primary mechanical structures are the elastin and collagen fiber networks. With respect to collagen, elastin fibers are two orders of magnitude softer. Elastin governs the low stiffness response of the tissue and is responsible for the elasticity of the tissue. In contrast, collagen is significantly stiffer. Within the tissue, collagen fibers have a pronounced tortuosity and do not start bearing load until they are uncrimped. Further, the collagen fibers bear load only in tension. The collagen fibers govern the high stiffness region of the mechanical response of the tissue. Together, the elastin and collagen fibers describe the typical nonlinear mechanical response of aortic tissue: an initial low stiffness region governed by elastin followed by a high stiffness region governed by collagen [48, 49].

1.3 TREATMENT OF AORTIC DISSECTION

Of 591 patients presenting with an acute Type A aortic dissection in a study of the IRAD database, only 12.4% had a known aortic aneurysm[33]. If aneurysm is known, patients undergo close monitoring of the aneurysm for diameter or rapid growth. Additionally, they are often prescribed medication to manage hypertension (e.g. beta-blockers) and cholesterol (statins) [50, 51, 52] although efficacy of these treatments are not wholly settled [53]. Due to the increased risk of dissection with tobacco use, cessation is suggested for habitual users [26].

Treatment of aortic dissections depend upon the location. Type B dissection is often treated pharmacologically - initial control of hypertension via beta-blockers with long-term antihypertensive medication for continued treatment. The high mortality in Stanford Type A dissections are due to the quick growth. For these reasons, patients presenting with this type of dissection require immediate surgical repair. Surgical repair can include replacement of the ascending aorta, aortic arch, and/or the aortic valve depending on the extent of the dissection. Surgery for those patients in higher risk groups often include replacement of a greater percentage of the aorta due to the relatively lower quality of the aortic tissue.

Patients presenting with an aortic dissection are often non-symptomatic prior to dissection. If patients at elevated risk of dissection (i.e. those with an aortic aneurysm) are identified before dissection, it is often due to routine medical testing for high risk groups (bicuspid aortic valve, connective tissue disorder) or imaging of the chest for unrelated reasons. If a person does experience aortic dissection, the most common symptom is acute pain. For Stanford Type A dissection, this may feel like chest pain which may travel down the body as the dissection propagates distally along the aorta. Due to the location of the pain, these dissections may be misdiagnosed as heart attack (as with actor John Ritter).

1.4 ASSESSMENT OF DISSECTION RISK

The current clinical practice for assessing aortic dissection risk is the aortic diameter. Per longitudinal studies of large patient cohorts, the risk of dissection increases drastically with an aortic diameter in excess of 6.0 cm [25, 26]. The importance of diameter is explained by the simplistic law of Laplace ($\sigma = Pr/t$) where σ is the wall stress in the CIRC direction and P, r and t are the blood pressure, aortic radius, and aortic wall thickness, respectively. Assuming the blood pressure and wall thickness are constant, the stress (and thus the risk of dissection or rupture) on the aorta will increase proportionally with the diameter. Exacerbating this is hypertension. In the absence of an evidence-based mechanistic understanding of the tissue, aortic diameter is the best indicator of risk.

Current clinical practice is preventive surgical intervention if the aortic diameter exceeds 5.5 cm. This criterion was determined through large scale clinical studies relating the risk of surgery against dissection and rupture. A 11 year study at the Yale University School of Medicine showed significant increase in risk of complications for aortic diameters of 6.0 cm or larger in the ascending aorta and 7.0 cm in the descending aorta [21, 22]. The Yale study suggested a lower threshold of surgical intervention in patients with bicuspid aortic valve or Marfan syndrome. However, the literature has identified issues with this metric. Wide variability in quantification of aortic diameter has been shown due to development of improved imaging techniques since the threshold was determined. Exacerbating this issue, of those presenting with dissection, approximately 60% have an aortic diameter under the critical threshold of 5.5 cm [33, 34, 35]. For this reason, there has been a growing understanding that the aortic diameter is insufficient to determine risk of complications.

The above shows that the clinical practice of a 5.5 cm diameter criterion for elective aortic repair underestimates the potential for aortic dissection. However, despite the high mortality of acute aortic dissection[9, 10], a simple reduction in the threshold is not feasible. Doing so would significantly over treat patients, subjecting a sizeable number of low risk patients to surgery. In addition to the considerable cost of surgical repair, the procedure itself carries a risk of death or impairment. Mortality rate at 30 days is 3-4%[54, 55] and up to 35% at 5 years (vs. 11% for control patients)[56]. Further, a significant decrease in quality

of life has been seen in ascending thoracic aorta repair patients vs. non-repair controls[55]. To improve patient risk assessments, identifying at-risk patients without over treating, an evidence based metric is required.

Recent work has attempted to do so using patient specific aortic geometries to determine failure risk through computational simulations of both the aortic wall and fluid flow in the aorta. Pasta et al.[6, 1] reports the maximum principal stress in the ascending thoracic aorta. Raghavan and Vorp[57] as well as Nathan et al.[58] study the von Mises stress distribution on the ascending thoracic aorta, with Nathan noting that von Mises stress is increased in regions with changes in curvature. Speelman et al.[59] reports the maximum principal stress for abdominal aortic aneurysms while Polzer et al.[60] and Rissland et al.[61] reports von Mises stress. By reporting the maximum principal stress, (or the von Mises stress) these papers are implicitly assuming that the dissection process is controlled by Laplaces law (that is, the current aortic diameter criterion). However, we have shown that the current metric is a poor indicator of dissection risk. Volokh[62] constructs a strain-softening model for arterial failure. Modeling the aortic wall, Roccabianca et al.[63] suggest that localized disruption of the wall may lead to dissection. The role of root motion on the stress-state in the thoracic aorta was studied by Beller et al.[64]. Our group has suggested that the radial strength of the tissue may be an important consideration in the dissection process[65, 66]. Martin et al.[67, 68], Duprey et al.[69] and Tabelsi et al.[70] suggest strain based dissection risk metrics for the thoracic aorta. The blood pressure at which failure is expected to occur however is significantly above the physiological range. The literature above does not include tissue failure mechanisms such as the effect of the microstructure of the tissue. Further, they are hampered by a lack of verification against clinical data.

1.5 OBJECTIVE OF THIS THESIS

Based on the above sections, it is clear that there is a need for a more accurate evidence based risk assessment for aortic dissection. The current clinical practice, aortic diameter, is relatively simple but underestimates the risk for approximately half of dissection patients.

A simple solution, reduction in the threshold for surgical intervention, is infeasible due to the cost and risk of surgery. This would lead to significant overtreatment of patients with low to moderate risk of dissection. Prior work in the literature has shown a link between dissection and the biomechanical properties of the aortic wall[71, 58, 72, 73]. For this reason, biomechanically based criteria for aortic dissection risk have been proposed[67, 70, 69, 74]. However, the proposed metrics have not as of yet yielded a clinically viable indicator of dissection risk. Thus, there exists a clinical need for a biomechanically based criterion. Hampering this goal is an overall lack of predictive capability in terms of location of dissection.

From a mechanics point of view, the dissection event initiates from a pre-existing intimal tear and is governed by the in-plane stresses on the aortic wall, dissection can be predicted by a "factor of safety. Dissection will occur when the stress in the aortic wall exceeds the strength of the tissue. However, the construction of such a factor of safety is complicated by the stress-state in the aorta as well as the mechanical properties of aortic wall tissue. The blood pressure within the aorta causes a complex varying biaxial stress-state on the aortic wall due to the local wall shape. Further, tissue within the ascending thoracic aorta wall is highly anisotropic, with the strength in the circumferential direction approximately twice that in the longitudinal direction[75]. Spatially varying biaxial stress-state in conjunction with the anisotropic material properties makes such a simple factor of safety impossible. Additionally, dissection is multifactorial in nature and this the effect of multiple patient-specific clinical factors on the tissue biomechanics must be assessed. In-depth understanding of the tissue failure mechanisms leasing to dissection initiation in conjunction with relevant patient-specific clinical factors are required to construct a mechanics-based metric of dissection risk. The objective of this thesis therefore is to evaluate such a metric by considering the microstructural properties of the tissue, patient-specific aortic geometry, and patient-specific material properties of the aortic wall.

Due to the literature showing a link between the microstructural properties of the aorta and dissection risk, we believe that understanding of the tissue behavior requires a structural model of the aortic microstructure that is not possible with phenomenological models. Using this model will allow for physiologically relevant material parameters to be included. The

construction of the microscale model of the aortic tissue will provide an understanding of the failure mechanisms present in the tissue that is relevant for the loading experienced *in vivo*.

We will create models of patient-specific aortic geometries from CT imaging. Stress analysis on these geometries, in conjunction with the knowledge gained from the microscale simulations, will yield a dissection potential index (DPI) for the ascending thoracic aorta. This DPI provides an evidence-based metric for aortic dissection risk that, with further clinical study, could provide a more accurate identification of at-risk patients.

1.6 SPECIFIC AIMS

Towards the development of a dissection potential index, the work described in this thesis will be divided into three specific aims. We will construct a model of the ascending thoracic aortic media wall. This model will be used to determine how the failure response at the microscale affects tissue failure under physiologically relevant loading. Finally, patient-specific aortic geometry will be used to develop an improved aortic dissection potential index.

1.6.1 Specific Aim 1: Development of an ascending thoracic aortic wall media embedded-fiber finite element model

A structural embedded-fiber finite element method will be constructed to model the media of the ascending thoracic aorta (Chapter 2). This model will be assessed by comparison against experimentally gathered uniaxial stress-stretch data (Chapter 3). We postulate that the structural model developed will accurately capture the pre-failure response of aortic media tissue.

1.6.2 Specific Aim 2: Determine how the microscale failure response affects failure under physiologically relevant loading

Structural models include all salient components of a material. We hypothesize that our embedded-fiber finite element model predicts failure properties of the ascending thoracic aortic media from experimentally gathered uniaxial stress-stretch data (Chapter 4). Further, we hypothesize that such a model estimates the failure response under physiologically relevant loading (Chapter 5).

1.6.3 Specific Aim 3: Construction of a predictive dissection risk metric

The limiting stress of the aorta is governed by the longitudinal strength. Using experimentally-determined patient-specific material properties and geometry, we postulate that the physiologic strength from Specific Aim 2 will construct a predictive metric for assessing dissection risk (Chapter 6).

2.0 EMBEDDED FIBER FINITE ELEMENT MODEL

Computational modeling of tissue remains a challenging endeavor within the biomechanics community. Native cardiovascular tissues are heterogeneous, anisotropic, and highly non-linear. Further, the mechanical stress-state of the tissue *in vivo* is complex due to the loading and geometry. Most tissue exhibits a "J-shaped" curve when loaded in tension. A representative stress-stretch response for the aortic wall is shown in Figure 2.1. The response of cardiovascular soft tissue can be divided into three general regions. The first region, the "toe region", has relatively low stiffness with respect to the rest of the curve. Response of the tissue in this region is approximately linear. The response of this region is primarily governed by the elastin fibers in the tissue [76]. The other primary load-bearing constituent of tissue, collagen, does not contribute to the response in this region. The second region is a transition region between the approximately linear response in regions I and III. Non-linearity in this region is due to the gradual recruitment of collagen fibers. Collagen fibers, which have significant crimp in region I, have minimal bending stiffness. Gradual realignment and straightening of the collagen fibers in this region increases the tissue stiffness as more collagen fibers contribute to the stiffness of the tissue. In region III, the collagen fibers have straightened from the initially crimped shape seen in region I. The fibers will act to reorient with the loading direction. Due to the high stiffness of collagen vs. elastin fibers, $E = 1.2$ MPa for elastin [77, 78] versus $E = 54$ MPa for collagen [79], the stiffness in this region is significantly elevated over that of region I. This region is governed by the collagen fibers.

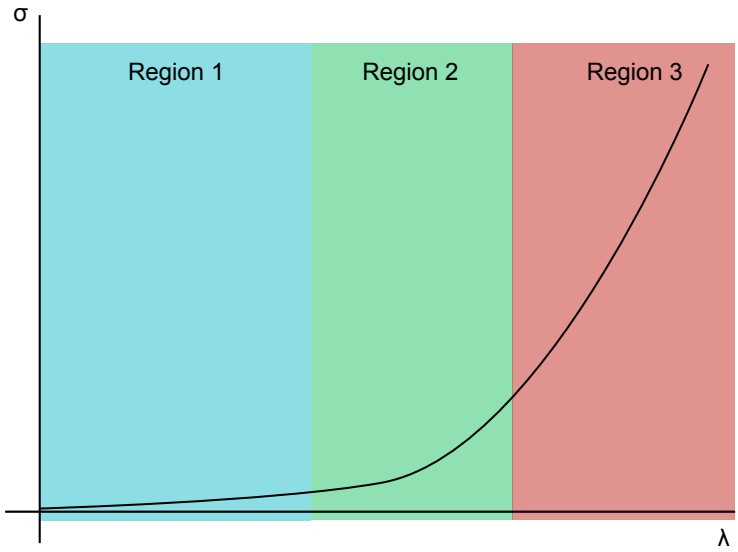

Figure 2.1: A representative stress-stretch response of soft tissue. The three regions are: elastin dominated, transition, collagen dominated. λ is the tissue stretch and σ the tissue stress.

2.1 MODELING OF VASCULAR SOFT TISSUE

Constitutive models for vascular soft tissue may be broadly classified in two groups: phenomenological and structural. Phenomenological models represent the tissue through a mathematical relationship whose parameters are not physically meaningful. While a wide variety of these materials are common within the literature, some well known models are the Fung and Moon-Rivlin models. A counterpoint to a phenomenological model is a structural model. These models attempt to improve the accuracy of the response by relating the material parameters to the physical aspects of the tissue. Complexity of these models varies, from the simple neoHookean material to distributed fiber models with multiple fiber families. Recent work has extended this idea further, explicitly modeling the fiber network.

2.1.1 Phenomenological models

At the inception of mechanical modeling of vascular tissue, the tissue was often modeled using a linear elastic material. When presenting the need for his newly developed phenomenological model, Fung states "[I]t is... perhaps important to point out that the usual practice of presenting a Young's modulus of elasticity for a blood vessel is meaningless." The solution to this issue was the development of phenomenological material models. As stated above, these types of material models are purely a mathematical fit to the data. That is, the material parameters do not have a physical meaning. This may simplify parameter estimation as no information beyond the experimental stress-strain curve is required. A notable model is the one introduced by Fung [80, 81]. Models based on this work are common in the literature [82, 83, 84, 85]. Although developed to model rubber elasticity [86, 87], the Mooney-Rivlin material model has also proven to be popular for vascular tissue [88, 89, 90]. Also of note is the isotropic abdominal aneurysm model developed by Raghavan and Vorp [57]. All of the above models represent continuum based hyperelastic materials.

2.1.2 Structural models

Based on the work of the phenomenological models above are structural models. As compared to the models above, these are constructed such that the parameters are based on physical aspects of the tissue. Detailed imaging of arterial tissue showed that there was a well defined structure. Wolinsky and Glagov [42] showed that the aortic media was divided into radially repeating structures defined by collagen and elastin networks. Imaging techniques such as X-ray diffraction [91], small angle light scattering (SALS) [92], and multiphoton microscopy [93] have shown that the structural proteins in the tissue have a defined orientation. From these data, new material models were constructed which explicitly included the collagen and/or elastin orientation in the continuum model for the tissue. Introduction of the actual fiber orientation in the model natively produces the typical anisotropy seen in vascular tissue. A common method [88, 94, 95, 96, 97, 49, 98] decomposes the strain energy function into isotropic and anisotropic portions with the anisotropic portion governed by an exponential fiber model. The fiber model is a function of $I_i = \mathbf{C} : \mathbf{A}_i$ where $\mathbf{C}$ is the right Cauchy-Green deformation tensor and $\mathbf{A}_i = \mathbf{a}_{0i} \otimes \mathbf{a}_{0i}$ with $\mathbf{a}_{0i}$ the direction of the i-th fiber family in the reference configuration. With this formulation, the continuum response of an arbitrary number of fiber families may be represented.

A further improvement over the above model represents the fiber network with an distribution of fiber orientations following a distribution [99, 100, 101, 102, 103]. Instead of modeling the response as a set of discrete families, these models allow for the experimentally observed distributions of fiber angle to be represented.

All the above models assume that the material is represented as a continuum. A recent development in the simulation of vascular soft tissue relaxes this constraint by modeling the fiber network explicitly. The non-fibrous matrix is represented as above (by decomposing the total strain energy function into isotropic and anisotropic portions), but each fiber in the fibrous network of the tissue is added to the simulation. The model developed by Barocas and collaborators [104, 105] uses a multiscale model with the fiber network at the microscale. We have proposed our own model to explicitly model the microstructure of aortic tissue [106]. Development of the model is detailed in the remainder of this chapter.

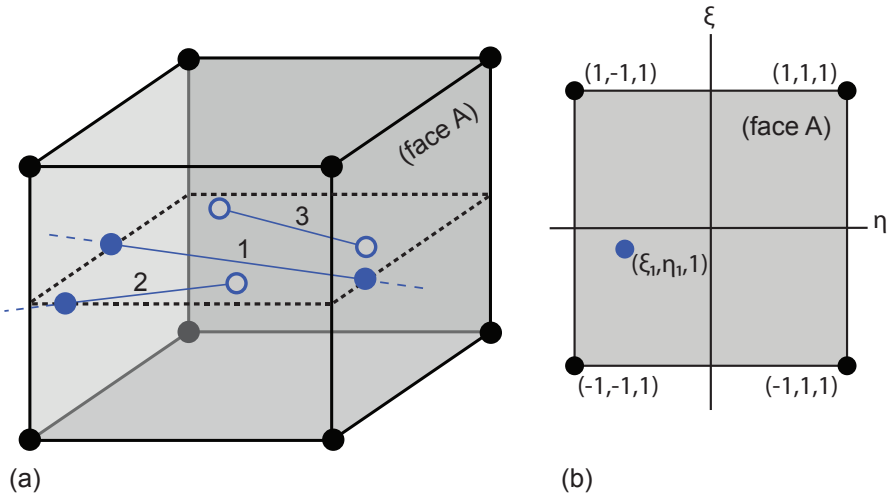

Figure 2.2: (a) Fibers embedded in a volumetric finite element. (b) Isoparametric coordinate of a point crossing the element face.

2.2 EMBEDDED-FIBER FINITE ELEMENT MODEL

To model the complex mechanical behavior seen with *in vitro* testing of soft tissue, we have developed an embedded-fiber finite element model. Consider a domain $\Omega \in \mathbb{R}^3$. Within the domain resides a fiber network f. A standard discretization of the domain yields a finite set of volumetric elements within which resides the embedded fiber network (Figure 2.2).

We propose a new finite element consisting of the typical 3D solid element (representing the non-fibrous matrix) and an arbitrary number of 1D bar elements describing the portion of the fiber network residing within the element. No constraint is placed on the number of fiber types within each element. Thus multiple fiber networks, or a network with distributions of fiber properties may be included without issue. To define the embedded-fiber finite elements, the fiber network must be apportioned amongst the volumetric elements. In general, a single fiber will not reside entirely within a single volumetric element. To determine the intersection point between the fiber segment and the volumetric element, a face-line intersection search algorithm was used (Algorithm 1). This algorithm, based on the algorithm given in [107],

assumes intersection of a infinite ray and a triangle. In the algorithm, $(a \cdot b)$ denotes the dot product of a and b. If hexahedral 3D elements are used, the each face is split into two triangles before the algorithm is called. The algorithm first defines the element face as an infinite plane and the fiber as an infinite ray. After determining if the ray intersects the plane, the barycentric coordinates of the intersection point are checked against the bounds of the line segment. If the intersection point is within the segment, barycentric coordinates of the intersection point are calculated on the triangle. As with the line segment, there is only intersection if the barycentric coordinates of the intersection point between the ray and the plane fall within the bounds of the face.

For non-trivial cases, determination of all intersection points in the domain is computationally expensive. To reduce the computational burden, an axis-aligned bounding box algorithm was used to pre-compute the potential intersections. Specifically, the volumetric elements in the domain were split into n regions based on the extents of the domain. A fiber was only checked for intersection within each region if the extents of the fiber intersected with that of the region.

Internally, all fibers are defined in terms of a volumetric element. The intersection points determined by Algorithm 1 provide the intersection on the volumetric element surface. There are three ways in which a fiber may intersect an element (Figure 2.2a). In case 1, the fiber passes entirely through the element. Two virtual nodes are defined on the volumetric element surface. For case 2, one end of the fiber is within the element while the other passes through a face of the element. The intersection point on the surface is determined in the same manner as case 1. In the third case, both endpoints of the fiber lie within the element. Degenerate cases, where a fiber lie on a volumetric element face, passes along an edge, or through an element node are captured and assumed by the code to follow one of the three cases above. Each fiber is thus decomposed into a series of fiber segments residing wholly within the volumetric element of the computational domain. Each fiber segment consists of two virtual nodes which lie either on the surface or interior of a volumetric element. These virtual nodes are defined in terms of the volumetric elements through barycentric coordinates (Figure 2.2b). In comparison to other methods, defining the fiber network in this manner does not impose any restriction on the volumetric element discretization. Consequently, arbitrarily

Algorithm 1 Intersection of a line and triangle (derived from [107])

Given line $l = (p_1, p_2)$ and triangle $t = (t_1, t_2, t_3)$

$u \leftarrow t_2 - t_1$, $v \leftarrow t_3 - t_1$, $n \leftarrow u \times v$ ▷ define plane and normal of t

$d \leftarrow p_2 - p_1$

$w \leftarrow p_1 - t_1$

if $|n \cdot d| < 0$ **then**

    No intersection

end if

$r \leftarrow -(n \cdot w)/(n \cdot d)$

if $r < 0$ or $r > 1$ **then**

    No intersection

end if

$I \leftarrow p_1 + rd$ ▷ intersection point on plane

$w \leftarrow I - t_1$

$D \leftarrow (u \cdot v) \times (u \cdot v) - (u \cdot u) \times (v \cdot v)$

$s \leftarrow ((u \cdot v) \times (w \cdot v) - (v \cdot v) \times (w \cdot u))/D$

if $s < 0$ or $s > 1$ **then**

    No intersection

end if

$t \leftarrow ((u \cdot v) \times (w \cdot u) - (u \cdot u) \times (w \cdot v))/D$

if $t < 0$ or $t > 1$ **then**

    No intersection

end if

Point I is the intersection point

dense fiber networks can be modeled with this method without refinement of the underlying volumetric finite element discretization.

2.3 FINITE ELEMENT FORMULATION

The fibers, represented by 1D rod elements, interact with the surrounding non-fibrous matrix, represented by the volumetric elements, through kinematically constrained virtual nodes situated within or on the faces of the 3D volumetric element. Isoparametric finite elements with nodal coordinates $\mathbf{X}^a$ and shape functions $\mathbf{N}_a$ were utilized to discretize the domain. The virtual nodes, to which the fiber segments are attached, were kinematically constrained to the 3D volumetric element. Isoparametric coordinates (ξ, η, ζ), (Figure 2.2b), for the virtual nodes were derived from their global position, $\mathbf{X}^*$, through the residual equation

$$\mathbf{R}(\xi,\eta,\zeta) := \mathbf{X}^* - \sum_a \mathbf{N}_a \mathbf{X}^a = \mathbf{0} \tag{2.1}$$

A Newton-Raphson iterative procedure was used to solve the above residual equation. These coordinates yield the location of the virtual nodes with respect to the volumetric element in which the fiber segment is embedded. Perfect bonding was assumed between the fiber segment and the volumetric element. Thus the isoparametric coordinates of the fiber segment endpoints and therefore the fiber itself remains fixed in relation to the volumetric element throughout the course of the simulation. As a consequence of the kinematic constraint on the fiber segment, the displacement of the two virtual nodes of the fiber segment, u_1^* and u_2^*, can be related to the nodal displacements of the solid element, $\tilde{\mathbf{u}}$ as

$$\{\mathbf{u}^*\} := \left\{ \begin{array}{c} u_1^* \\ u_2^* \end{array} \right\} = [\mathbf{P}\,(\xi,\eta,\zeta)]\,\{\tilde{\mathbf{u}}\} \tag{2.2}$$

where the projection tensor, $\mathbf{P}$ contains the nodal shape functions for the solid element evaluated at the location of the virtual nodes (ξ,η,ζ). For a 8-noded hexahedral element, the shape functions are given by

$$\begin{array}{llll} N_1 = & \frac{1}{8}(1-\xi)(1-\eta)(1-\zeta) & N_1 = & \frac{1}{8}(1+\xi)(1-\eta)(1-\zeta) \\ N_3 = & \frac{1}{8}(1+\xi)(1+\eta)(1-\zeta) & N_4 = & \frac{1}{8}(1-\xi)(1+\eta)(1-\zeta) \\ N_5 = & \frac{1}{8}(1-\xi)(1-\eta)(1+\zeta) & N_6 = & \frac{1}{8}(1+\xi)(1-\eta)(1+\zeta) \\ N_1 = & \frac{1}{8}(1+\xi)(1+\eta)(1+\zeta) & N_1 = & \frac{1}{8}(1-\xi)(1+\eta)(1+\zeta) \end{array} \tag{2.3}$$

An additive decomposition is used to split both the element stiffness matrix ($\mathbf{K}$) and load vector ($\mathbf{R}_{int}$) into bulk and fiber contributions as

$$\mathbf{R}_{int} = \mathbf{R}^b_{int} + \mathbf{R}^f_{int} \tag{2.4}$$

$$\mathbf{K} = \mathbf{K}^b + \mathbf{K}^f \tag{2.5}$$

with b and f denoting the bulk and fiber terms, respectively. The contributions of the bulk material are computed in the standard manner. To compute the fiber components, the axial displacement of each fiber segment u_f is computed from the displacement of the volumetric element (via Equation 2.2). The stretch of the fiber segment is then found by

$$\lambda_f = 1 + \frac{u_f}{l_0} \tag{2.6}$$

where l_0 is the initial length of the fiber segment.

Constitutive response of the fibers differs in the literature. Chapters 3 and 4 propose a linear fiber response (see Equation 3.5), but various other responses are used by other groups. See for example the exponential fiber models used in [108, 102]. With the fiber force, $f(\lambda)$, the virtual work done by the fiber is then

$$\delta W^f = f(\lambda)\delta u_f \tag{2.7}$$

The virtual work for the fiber segment may be rewritten using the shape function describing the displacement field for each fiber segment ($\mathbf{B}$) and equation 2.2.

$$\delta W^{fib} = f(\lambda)\left[\mathbf{B}\right]\left[\mathbf{P}\right]\left\{\delta\tilde{\mathbf{u}}\right\} = {}^i\mathbf{R}^f_{int}\left\{\delta\tilde{\mathbf{u}}\right\} \tag{2.8}$$

The variable $\mathbf{B}$ is given by

$$\mathbf{B} = \begin{bmatrix} \frac{\partial N_1}{\partial x} & 0 & 0 & \frac{\partial N_n}{\partial x} & 0 & 0 \\ 0 & \frac{\partial N_1}{\partial y} & 0 & 0 & \frac{\partial N_n}{\partial y} & 0 \\ 0 & 0 & \frac{\partial N_1}{\partial x} & 0 & 0 & \frac{\partial N_n}{\partial x} \end{bmatrix} \tag{2.9}$$

where $N_{1,\ldots,n}$ are the shape functions for the n nodes of the element.

In the virtual work equation, ${}^i\mathbf{R}^f_{int} = f(\lambda)\left[\mathbf{B}\right]\left[\mathbf{P}\right]$ stands for the internal load vector for the i-th fiber with respect to the solid element local coordinate system. The expression of

the stiffness matrix was obtained as a sum of the material and geometric tangent stiffness terms as

$$\mathbf{K}_{int}^{f} = \underbrace{[\mathbf{P}]^T [\mathbf{B}]^T k_f [\mathbf{B}] [\mathbf{P}]^T}_{\text{material}} + \underbrace{[\mathbf{P}]^T [\mathbf{D}]^T f [\mathbf{P}]}_{\text{geometric}} \tag{2.10}$$

where k_f is the stiffness of the fiber obtained as $k_f = \partial f / \partial u_f$ and $[\mathbf{D}] = \mathrm{d}[\mathbf{B}]/\mathrm{d}\{\tilde{\mathbf{u}}\}$. Finally, adding the contributions from n fibers within a volumetric element, the load and tangent stiffness contributed by the fiber segments are

$$\mathbf{R}_{int}^{f} = \sum_{i=1}^{p} {}^{i}\mathbf{R}_{int}^{f} \tag{2.11}$$

and

$$\mathbf{K}^{f} = \sum_{i=1}^{p} {}^{i}\mathbf{K}^{f} \tag{2.12}$$

2.4 EFFECT OF FIBER ARCHITECTURE ON THE MECHANICAL RESPONSE

We demonstrate the utility of the embedded-fiber finite element method developed in the previous section by studying its effect with various fiber network properties. The domain was taken as 250 μm $\times$ 250 μm with a thickness of 6.25 μm. The network properties varied with the test, but were based on a Voronoi tessellation of randomly placed points on a plane aligned with the two principal directions of the domain. Collagen fibers are commonly represented using an exponential stress-stretch response [88, 109, 105, 96, 102]. Thus, the following strain energy function was used to model the fibers,

$$\Psi = \begin{cases} 0 & \text{if } \lambda < 1 \\ \frac{k_1}{k_2} \left[\exp\left(k_2 (\lambda^2 - 1)^2 - 1 \right) \right] & \text{if } \lambda \geq 1 \end{cases} \tag{2.13}$$

where λ is the fiber stretch and k_1 and k_2 are material parameters. The response is assumed to be zero if $\lambda < 1$ as the fibers do not bear load in compression.

The non-fibrous matrix was modeled as an incompressible isotropic neoHookean material ($\Psi = \mu/2(I_1 - 3)$) with μ denoting the shear modulus of the material and I_1 the first invariant of the right Cauchy-Green deformation tensor.

The properties of the non-fibrous matrix were chosen to be significantly lower than the fibers. The fibers were assumed to bear load from the beginning of the simulation (that is the recruitment stretch was 1).

The domain was loaded uniaxially in via an applied displacement on one face. The opposing face was fixed against deformation and rollers were applied to the orthogonal faces. Convergence studies showed that a discretization of 10,800 8-noded hexahedral elements and a loading rate of 400 steps was sufficient for convergence. The stress-strain response of the simulated tissue in the loading direction was collected for each load step in the simulation. The applied stretch for the simulations was $\lambda = 1.4$.

Three sets of simulations were performed: variation of mean fiber angle, fiber angle dispersion, and fiber volume fraction. These parameters were chosen as they are the primary architectural parameters of the embedded-fiber finite element method developed above.

Unless otherwise specified the fiber networks were constructed with a volume fraction of 20%, standard deviation of fiber angles of 10°, and a mean fiber angle in the loading direction.

2.4.1 Effect of fiber network orientation

The first test run was a study of the effect of the fiber network to the loading direction. An aligned network with a small dispersion in fiber angle (a standard deviation of 10 degrees) was created. The size of the network was taken as 500 μm $\times$ 500 μm (sufficiently large so that it spanned the domain after rotation). The mean fiber direction was varied in 15 degree increments from 0 degrees (aligned with the loading direction) to 90 degrees (orthogonal to the loading direction). Under the uniaxial loading condition described above, the resultant stress seen in the stress-strain curve increased as the network was aligned to the loading direction (Figure 2.3).

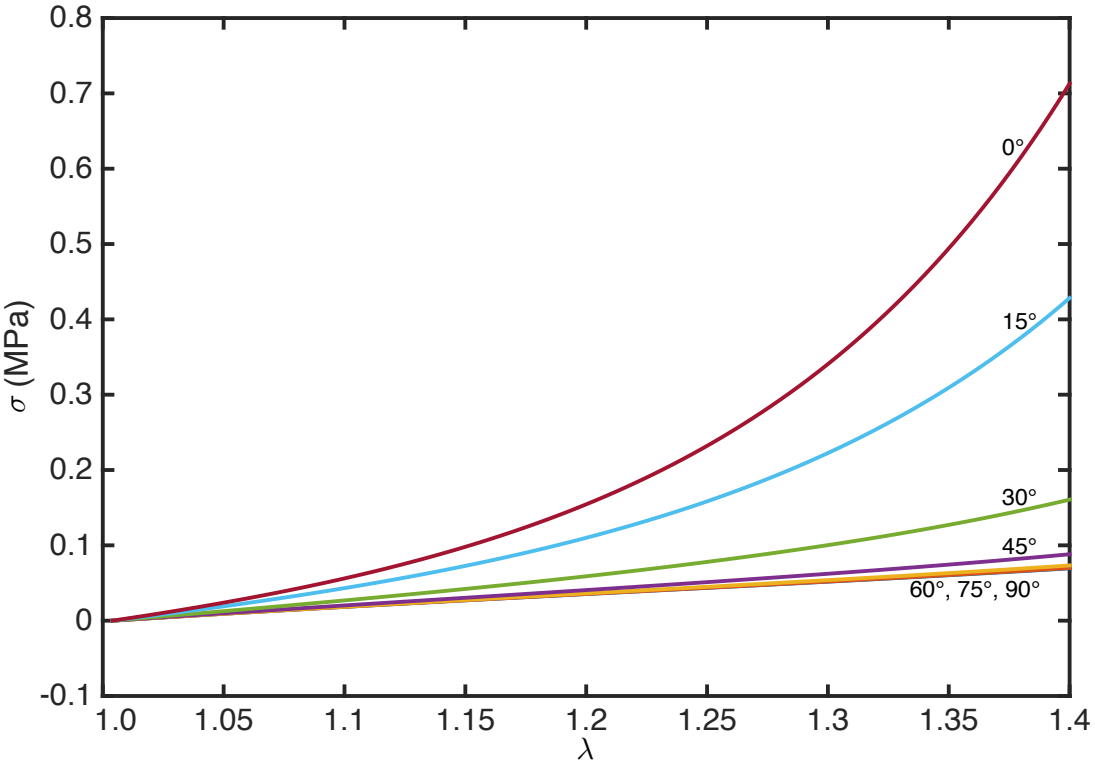

Figure 2.3: The mechanical response of fiber networks with a mean angle from 0 degrees (aligned with load) to 90 degrees (orthogonal to load)

With the network orthogonal to the loading direction, the response was approximately equal to that of the non-fibrous matrix. There was no appreciable stiffening in the response due to the fibers. Under moderate alignment with the loading direction (up to 45°), there was still little increase in the tissue stiffness. This is due to the fact that the fibers were unable to reorient to the loading direction under the loading provided.

2.4.2 Effect of fiber network alignment

As opposed to the previous section, the mean angle of the fiber network remained aligned with the loading direction over the course of these simulations. Instead, the alignment of the network (i.e. the spread in the distribution of the fiber angles) was modified. Four networks with the distribution of the fiber angles ranging from a standard deviation of 40° (highly isotropic) to 10° (highly aligned) in 10° increments. Ten degrees was chosen as the most aligned case (as opposed to fully aligned, SD=0 degrees) to correspond to the highly aligned cases seen experimentally for vascular wall tissue. To ensure a meaningful comparison between the cases, each network was created with a volume fraction of 20%. The stiffness of the tissue increased with the degree of alignment (Figure 2.4).

With an isotropic fiber network, the response at $\lambda = 1.4$ was approximately half that of the most aligned network. Interestingly, even the isotropic network was significantly stiffer than the orthogonal fiber case (see e.g. the 0 degree case in Figure 2.3).

2.4.3 Effect of volume fraction

The final test varied the volume fraction of the fiber network. The same mean fiber angle (0 degrees, aligned with the loading direction) and fiber angle alignment (a standard deviation of 10°) was used for the five networks tested. The volume fraction was increased in 5% increments from 0 to 20%. With a volume fraction of zero (i.e. no fibers), the material response was that of the non-fibrous matrix. The stiffness of the material increased with an increase in the volume fraction (Figure 2.5). The simulations showed an increase in stiffness linear with volume fraction. Of the three sets of simulations performed, the volume fraction was the only parameter with a linear relationship to the stress.

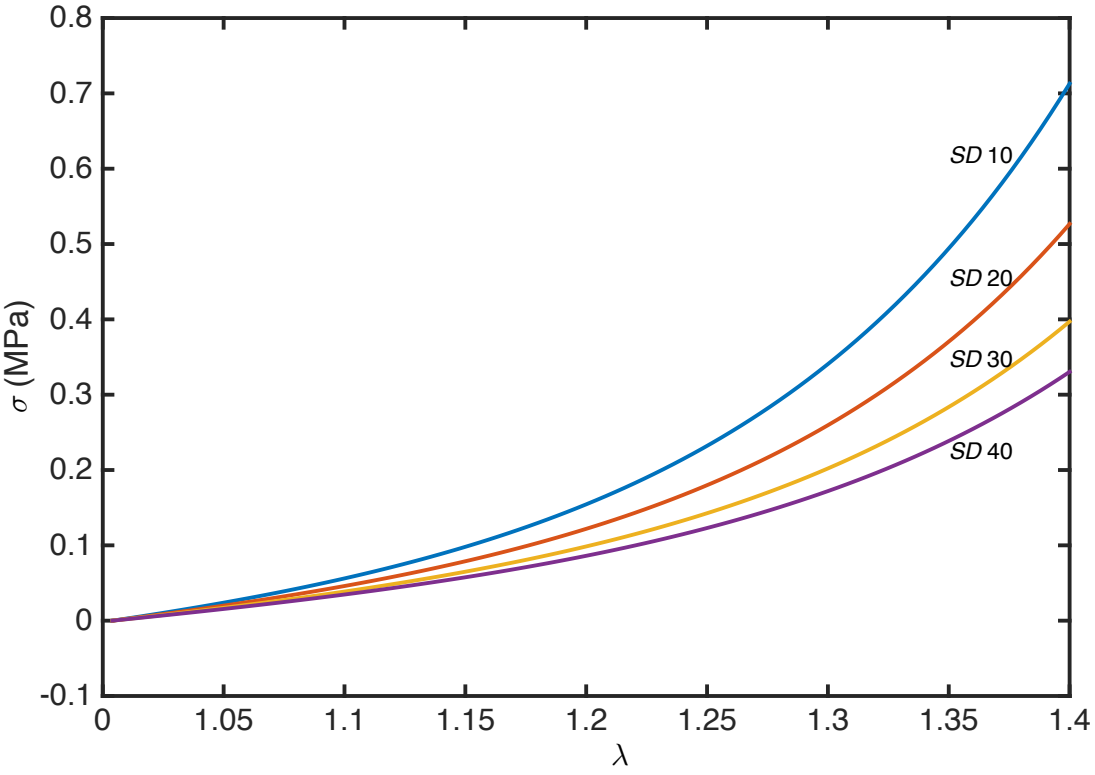

Figure 2.4: The mechanical response of fiber networks with varying degrees of fiber angle dispersion

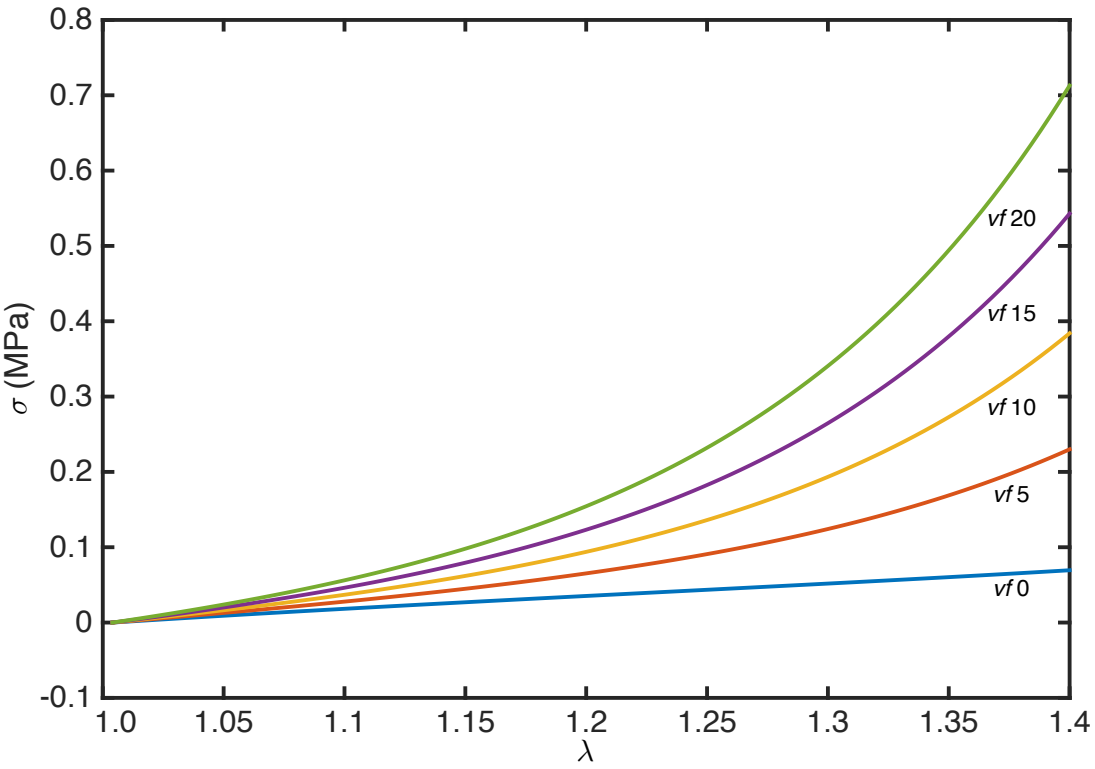

Figure 2.5: The mechanical response of fiber networks with volume fractions from 0 to 20%

2.5 CONCLUSIONS

This chapter has developed the embedded-fiber finite element method that will be used throughout the course of the rest of this work. Contrary to other methods in the literature, this method provides exceptional usability as discretization of the volumetric elements is independent of the fiber network architecture. For this reason, arbitrarily dense fiber networks may be simulated without excessive volumetric mesh density. Further, modification of the fiber network requires only regeneration of the fiber network, without any changes to the volumetric element mesh. Internal storage of the fibers is computationally efficient with the fibers split into segments which reside within the volumetric elements. One limitation of the method is the current assumption of affine deformation of the fibers with respect to the volumetric elements. While this appears to be an acceptable assumption [110, 111], implementation of non-affine behavior may be important for some tissues or loading scenarios (e.g. [108]). In general however, dense networks are assumed to follow a grossly affine behavior [112].

We have shown the utility of the method via a fiber network based upon the vascular wall. It was shown that the architectural features of the fiber network (the mean fiber direction, fiber dispersion, and fiber content) has significant impact on the mechanical response. Both direction and dispersion scaled nonlinearly whereas a strong linear relationship was seen between the volume fraction and material stiffness. These simulations explored the mechanical behavior of an approximate material. The next two chapters develops the method further, exploring the prefailure response (Chapter 3) and failure response (Chapter 4) of the aortic media. We will show that the method developed in this chapter is suitable for both fitting and predicting the mechanical response of aortic tissue.

While this chapter follows the majority of the literature by modeling the fibers using an exponential constitutive response, the subsequent chapters show that this is not a necessary requirement for matching the physically observed tissue response. Accurate fits were obtained using a linear fiber model with the inclusion of an initially zero stiffness region to capture the fiber recruitment stretch of the fiber (Equation 3.5). While the exponential model used in this chapter implicitly models the fiber recruitment stretch, the linear model

proposed in the referenced equation explicitly models this parameter. A similar model for the fiber was used by e.g. [113]. While not addressed in this work, formulation of the constitutive behavior in this manner would allow for study of the effect of gradual fiber recruitment due to a distribution of the recruitment stretch. Other researchers have suggested that such a mechanism is an important factor in the response of vascular tissue [114].

3.0 DEVELOPMENT OF A MICROSTRUCTURAL MODEL OF THE AORTIC MEDIA

3.1 INTRODUCTION

The work described in this chapter was previously published in [106].

Biomechanical response of the ascending thoracic aortic (ATA) wall tissue plays an important role in the pathophysiology of the thoracic aorta. The aorta is composed of three layers: the intima (yellow), media (red) and adventitia (orange) (Figure 3.1). This work focuses on the media as most aortic dissections travel through this layer. Primary load-bearing components of the ATA media are lamellar units (LU) consisting of elastic lamellae encompassing vascular smooth muscle cells (VSMC), interposed with collagen fiber network (Figure 3.1b). Incorporation of the above mentioned structural features of the lamellar units are thus essential in the study of biomechanical response of ATA wall tissue. A number of structurally motivated constitutive models for the arterial wall have recently appeared in the literature that augment the strain energy expression with additional terms incorporating experimentally observed collagen fiber tortuosity and orientation ([115, 116, 109, 117, 101, 118]). These constitutive models are a major improvement over purely phenomenological models, and are quite successful in fitting the overall stress-strain response of arterial wall tissue specimens. However, these models are not fully structural representations of the aortic wall. Thus they cannot examine, for example, the effect of physiological fiber network architecture and fiber-nonfibrous matrix interaction on the biomechanical state of the wall tissue. These lamellar scale details can give rise to locally heterogeneous stress distribution within the elastic lamellae and may influence structural and functional remodeling of the extra- cellular matrix by the VSMCs mediated by local mechanical stimuli.

Our goal in this study was to develop a finite element based modeling framework leading towards true structural representation of the ATA media lamellar unit. To achieve this goal, we developed a novel fiber reinforced finite element method capable of embedding 1D fibers of arbitrary orientation within 3D finite elements. Using this framework, we created a representation of the lamellar unit of the human aortic media that directly included structural features of the tissue. The developed model could recapitulate the uniaxial constitutive response of the media successfully. Additionally, our model revealed that stress state in the non-collagenous matrix is homogeneous at low stretch, but becomes highly heterogeneous at higher stretch levels after collagen fiber recruitment. Magnitude of non-collagenous matrix stress depends on the local architecture of the collagen network. Further, collagen fibers oriented themselves in the loading direction, and created distinct stress paths that were the primary load-bearing mechanism at high stretch.

3.2 METHODS

To simulate the biomechanical response of the aortic media, a representative volume element (RVE) of the lamellar unit (LU) was constructed (Figure 3.1c). In the figure, the green region represents the elastic lamella and the red region represents the interlamellar space. Location of the collagen fiber network is shown with the dashed line. Symmetry in the radial (RAD) direction was exploited such that only half of the LU was modeled. Thickness of the LU (and it's constituents) vary depending on location and depth within the aortic media. Therefore, the depth-wise thicknesses of the LU and the elastic lamellae were chosen as 1.5 μm for the elastic lamellae and 11 μm for the LU [44]. Based upon the multiphon microscopy (MPM) images on which the RVE is based, the dimensions of the RVE in the CIRC and LONG directions are 250 μm. The solid box in Figure 3.1 denotes the size of the RVE with respect to the entire LU. A network of 21,000 elastin fibers were embedded within the elastic lamella (Figure 3.1d). Elastin fibers were oriented randomly within the $250 \times 250 \times 1.5\ \mu m$ elastic lamella. The volume fraction of elastin in the elastic lamella was taken as 85% (10% of the total volume of the RVE). The orientation of the elastin fibers were based on our previously

published work [5] (normalized orientation index (NOI) 0.70). NOI is a measure of the degree of orientation of the fibers within a network defined as

$$NOI = \frac{90 - OI}{90} \times 100, \quad NOI \in [0, 100] \tag{3.1}$$

where OI is the area containing half of the total fiber angles [119]. An NOI of 0 denotes an isotropic network while 100 denotes a fully aligned network.

As the planar component of the collagen fibers is more significant than the out-of-plane components [120], the collagen network was constructed such that it lay entirely on the CIRC-LONG plane (Figure 3.1e). The network is embedded within the IL space and is situated directly below the elastic lamella. Due to the depth-wise variation in the collagen network properties, MPM imagery could not be used directly to construct the collagen network. Instead, averaged network parameters of MPM images taken at 10 μm increments through the media thickness were used [2, 5]. The fiber microstructure was computer generated using these values. Similar image-based computational representations of fiber networks have recently been utilized in the context of electrospun polymeric materials [110, 121] and tissue [122]. Orientation distribution (OD) for the collagen network from [5] and the fiber intersection density and areal density (AD) from [2] were as inputs for construction of the computational collagen network.

3.2.1 Construction of the elastin network

To construct the elastin network, a custom matlab script (Matlab 2014b, Mathworks, Natick, MA) was used. A 3D bounding box ($250 \times 250 \times 1.5\,\mu m$), representing the extents of the elastin network was described. For each fiber in the network, a random point p, uniformly distributed within the bounding box, was chosen as the seed point for the elastin fiber. A uniformly distributed fiber angle θ within the CIRC-LONG plane was chosen and a small random perturbation in the RAD direction applied. The infinite line at angle θ and passing through p was projected to the faces of the bounding box and the intersection point recorded. A line-plane intersection algorithm, based on [107] was used. The volume of the fiber was added to the total network fiber length and the elastin fiber volume fraction calculated. If the

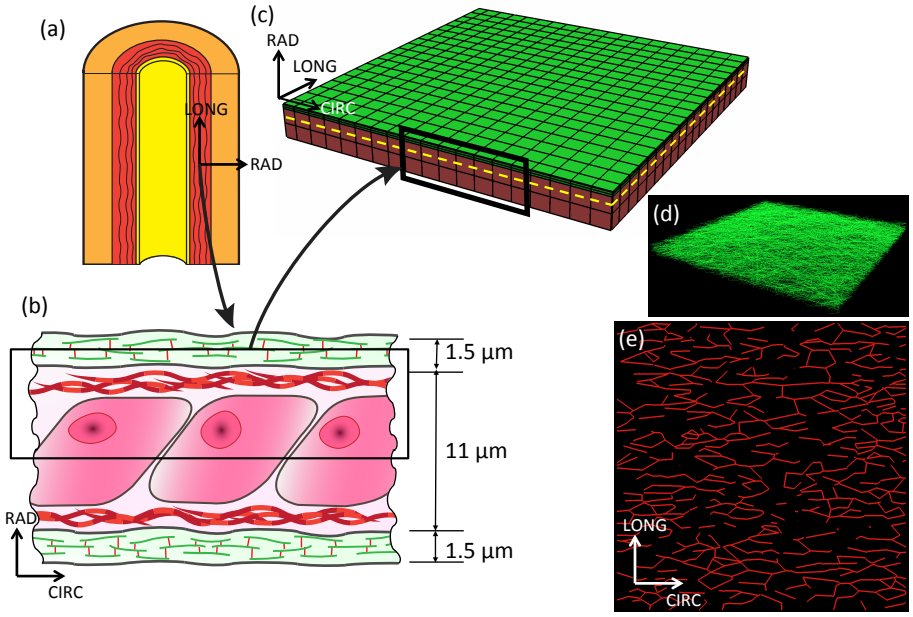

Figure 3.1: (a) The three layers of the aorta. (b) The media is composed of multiple lamellar units. (c) A RVE of the LU. (d) The elastin fiber network and (e) collagen fiber network.

volume fraction was less than the target volume fraction, then another fiber was added. This process was continued until the target volume fraction was reached. The process is described in Algorithm 2. In the algorithm, Intersection returns the intersection points between the line and the bounding box and CSA is the cross-sectional area of the fiber. vol_{BB} is the volume of the bounding box.

3.2.2 Construction of the collagen network

As with the elastin network generation, the collagen network was constructed using a custom matlab script. However, due to the planar nature of the collagen networks seen *in vivo*, the collagen network was created using a 2D algorithm. An isotropic voronoi tessellation was constructed using randomly selected points within a bounding box sufficiently large that modification of the network still ensured that it filled the domain. The initially isotropic voronoi tessellation was systematically modified to conform to the input network properties:

Algorithm 2 Elastin fiber network generation

Define Bounding Box $BB \in \mathbb{R}^3$

while $vf < vf_{elastin}$ **do**

Get random point $p \in BB$

Get random angle $\theta \in [0, 360]$

Define line l at θ through p

$[b1, b2] \leftarrow \text{Intersect}(l, BB)$

$len \leftarrow \text{norm}([b1, b2])$

$vol \leftarrow CSA \times len$

$vol_{tot} \leftarrow vol_{tot} + vol$

$vf \leftarrow vol_{tot}/vol_{BB}$

end while

OD, intersection density, fiber length, and AD. The process for the network generation is given in Figure 3.2.

As the voronoi tessellation was constructed with randomly placed seed points, the resulting network was isotropic. However, experimental MPM of the collagen networks show anisotropy. Thus, after tessellation of the randomly placed seed points, an affine transformation was applied to the network. Given a point $\mathbf{x} = \{x_1, x|2\}$, an affine transformation can be described by $\mathbf{x}' = \mathbf{A}\mathbf{x}$ where $\mathbf{x}'$ is the deformed point and $\mathbf{A}$ is a transformation matrix. This work imposes only scaling transformations on the network. The transformation matrix for that operation is

$$\mathbf{A} = \begin{bmatrix} w & 0 \\ 0 & h \end{bmatrix} \tag{3.2}$$

where w and h are the scaling factors in the CIRC and LONG directions, respectively.

A non-linear minimization algorithm (fmincon, Matlab 2014b) was used to minimize the distance between the experimentally gathered OD and the OD for the simulated network. The objective function of the minimization function was defined as $\min d_{l2}$ where d_{l2} was the Euclidean distance ($l2$ norm) between the experimental and simulation OD. The Euclidean

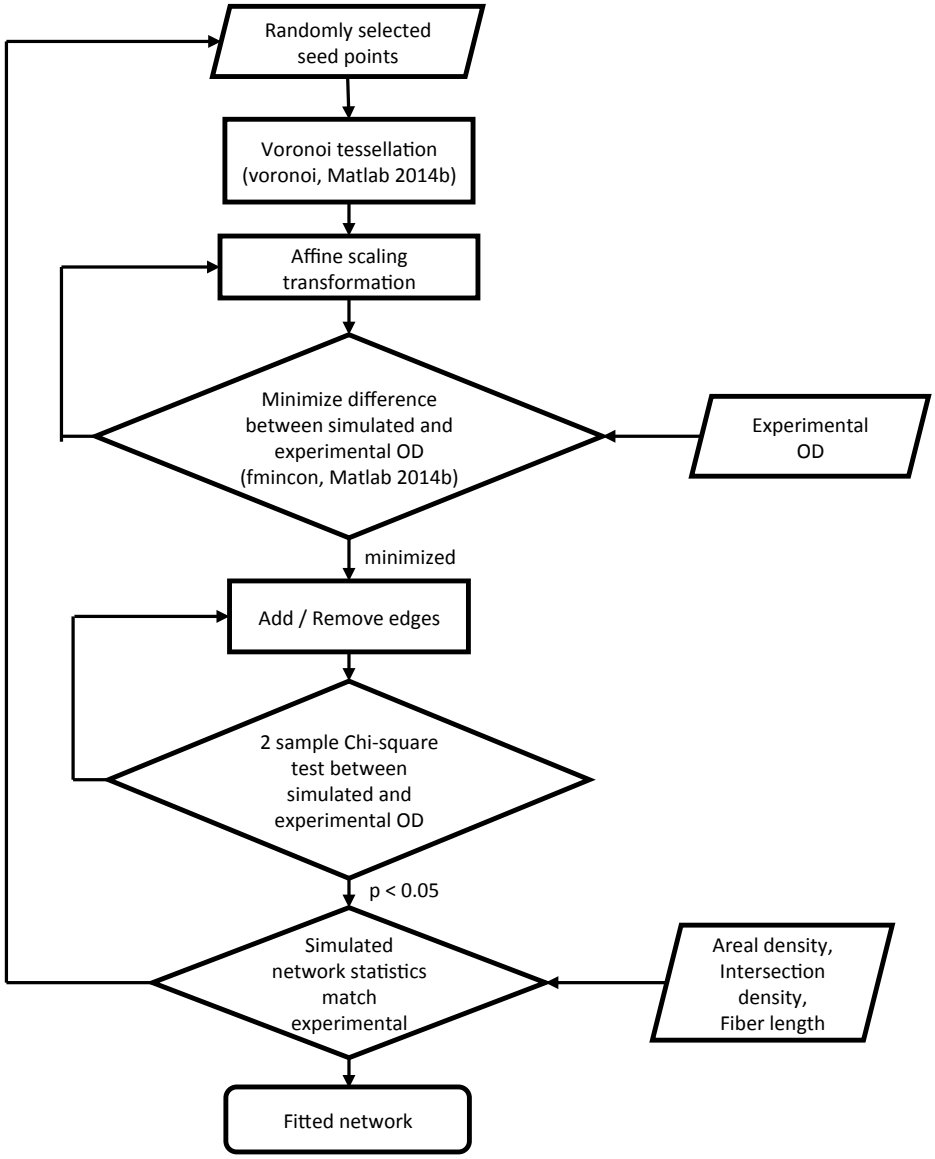

Figure 3.2: Collagen fiber network generation algorithm

distance is defined as

$$d_{l2} = \sqrt{\sum_{i=1}^{n} \left(OD_{exp}(i) - OD_{sim}(i)\right)^2} \tag{3.3}$$

with n denoting the number of angles in the OD and $OD_{exp}(i)$ and $OD_{sim}(i)$ the value of the orientation distribution for the i-th angle, respectively. Scaling parameters were restricted to positive values and the minimization was stopped when either the maximum number of iterations was reached or the tolerance was reached. To ensure a global minimum, the minimization was performed 25 times with randomly selected initial scaling factors.

Scaling alone may be insufficient to match the experimental orientation distribution depending on the microarchitecture. For this reason, after the minimization process, fibers were added and removed from the network to conform to the experimental OD. A two-sample Chi-squared test was used to determine the difference between the two network ODs. Additional fiber addition and removal steps were performed until the Chi-squared test showed equivalence in the ODs ($p \leq 0.05$). A representative experimental and simulated network OD is shown in Figure 3.3. The CIRC direction is at 0° and the LONG direction at ±90°. The final simulated network was checked against remainder of the experimentally gathered network parameters (fiber length, AD, and intersection density). A new network was created with a different set of seed points if the parameters from the simulated network were not equal to the experimentally gathered parameters (±1 standard deviation). The values of the experimentally gathered parameters as well as the parameters for the simulated network are shown in Table 3.1. With a areal density of 34%, the resulting volume fraction of collagen in the RVE was 16%. To determine the effect of the network architecture on the mechanical response of the tissue, five networks each of the aneurysmal TAV and BAV tissue were created. The mean and standard NOI from [5] were used to construct the ODs of the networks while the areal density, intersection density, and fiber length were kept constant at the value listed in Table 3.1.

3.2.3 Finite element simulation methodology

The RVE was discretized with custom-developed fiber-finite elements representing collagen or elastin fibers within 8-noded hexahedral elements (Figure 3.4a). The fibers, modeled as

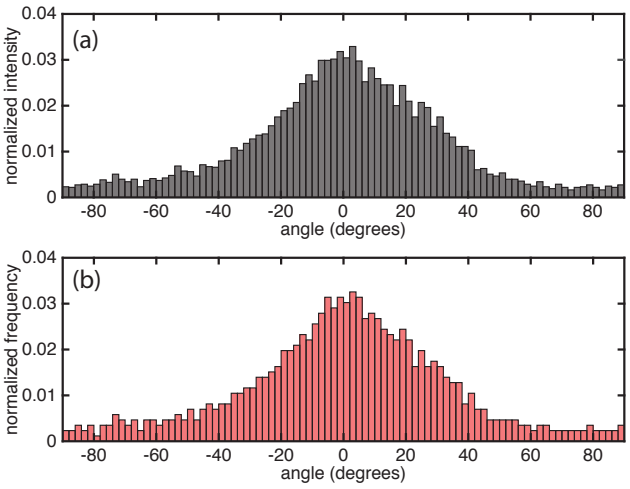

Figure 3.3: Orientation distribution for a representative collagen fiber network (reproduced from [5]) in the aortic media of an aneurysmal BAV patient (a) and that of a simulated computational network (b).

Table 3.1: Structural properties of the collagen network.

Parameter	Experimental value (from [2])	Simulated value	Notes
Areal density (AD)	27-32%	34%	Input to simulated network
Intersection density	0.005-0.01 μm^{-2}	0.009 μm^{-2}	Input to simulated network
Average fiber length	13-17 μm	9 μm	Derived from simulated network

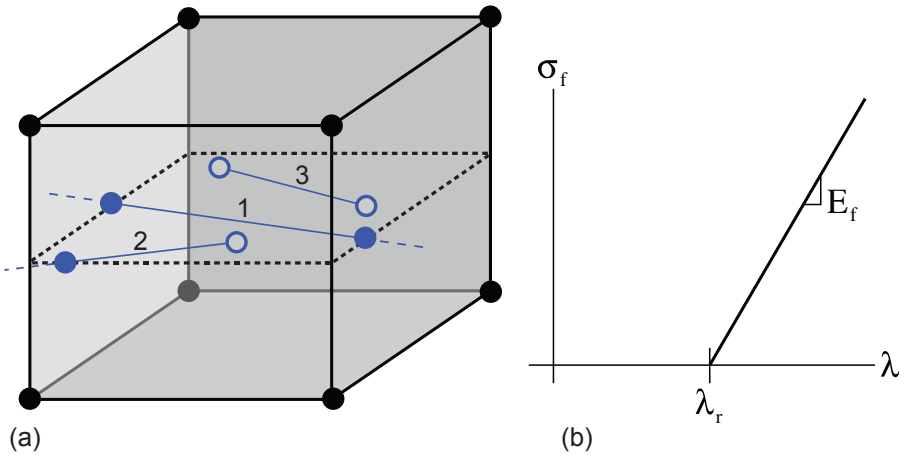

Figure 3.4: (a) Fibers embedded within a volumetric finite element. (b) The constitutive relationship for individual fibers.

2-noded bar elements, were kinematically constrained to the deformation of the surrounding volumetric elements via "virtual nodes" at the end of the fibers. Affine deformation between the fibers and underlying non-fibrous matrix was assumed. For this reason, isoparametric coordinates representing the virtual nodes of the fibers remained constant over the course of the simulation. Details of the finite element formulation are given in Appendix 2.

A stretch of $\lambda = 1.5$ was applied in the CIRC direction. To ensure a homogeneous stress-state in the absence of collagen fibers, rollers were applied to the LONG faces and on the symmetry plane. A custom nonlinear finite element program, developed in our lab and used to study biological tissues [66, 123] was used to simulate the RVE. Convergence studies suggested that a finite element mesh of 10,800 8-noded hexahedral elements was sufficient when the load was ramped linearly over 400 load steps. Stress contour in both the non-fibrous matrix and the fibers were plotted using Paraview 4.1.0 ([124]). The mean stress in the non-fibrous matrix were compared at different applied stretches using a paired t-test. Levene's test was used to compare variance of these groups (Matlab). A paired t-test was also used to compare the maximum non-fibrous matrix stresses in the BAV and TAV simulations.

3.2.4 Constitutive model and parameter estimation

The non-fibrous matrix was modeled using a 1-parameter neo-Hookean material ([49]) with the strain-energy functional

$$\Psi = \frac{\mu}{2}(I_1 - 3) \tag{3.4}$$

where μ is the shear modulus of the material and $I_1 = \text{tr}\mathbf{C}$ is the first invariant of the right Cauchy-Green deformation tensor ($\mathbf{C} = \mathbf{F}^T\mathbf{F}$). The deformation gradient, $\mathbf{F} = \text{d}\mathbf{x}/\text{d}\mathbf{X}$, is defined in terms of the nodal positions in the reference ($\mathbf{X}$) and deformed ($\mathbf{x}$) configurations. Full finite element implementation of this model is given in Appendix A.2.

The collagen and elastin fibers were assumed to be stress free in compression. In tension, the response was modeled as

$$\sigma = \begin{cases} 0 & \text{if } \lambda < \lambda_r \\ E_f(\lambda - \lambda_r) & \text{if } \lambda \geq \lambda_r \end{cases} \tag{3.5}$$

where λ is the fiber stretch, λ_r is the recruitment stretch, and E_f is the elastic modulus of the fiber (Figure 3.4). As the fibers were modeled as straight segments, the recruitment stretch was introduced to account for the tortuosity of the fiber. All collagen fibers were modeled with a diameter of 3 μm [2] while the elastin fiber diameter was taken as 0.1 μm [104].

As the shear modulus of elastin is reported in the literature as between 100 and 1000 kPa [125], E_f for the elastin fibers was taken as 3 MPa. The simulated constitutive response was regressed against previously reported experimental uniaxial tensile tests on aneurysmal BAV tissue [6] to fit the remaining material parameters: μ_M (shear modulus of the non-fibrous matrix), E_f, and λ_r (Table 3.2). The elastin fiber stiffness and recruitment stretch were taken to be constant for the fitting process. These fitted material parameters were used for all BAV and TAV simulations. Goodness of fit between the experimental and simulated stress-stretch response was determined using the coefficient of determination (r^2). For the simulations, $r^2 = 0.996$, Figure 3.5.

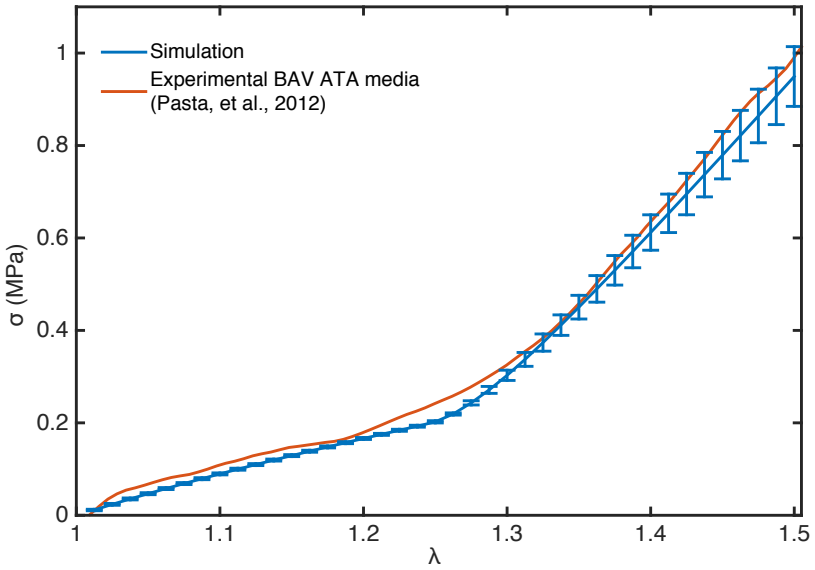

Figure 3.5: Stress-stretch relationship for simulation experimentally gathered uniaxial tensile testing of aneurysmal BAV tissue (from [6]) in the CIRC direction.

Table 3.2: Fitted material parameters for the fibers and non-fibrous matrix.

Role	Parameter	Fitted value	Reported value
Non-fibrous matrix	μ_M	170 kPa	-
Collagen fiber	E_f	80 MPa	54±25 MPa [79]
	λ_r	1.25	1.2-1.4 [118]
Elastin Fiber	E_f	3 MPa	$\mu = 3$ MPa [125]
	λ_r	1.0	-

3.3 RESULTS

3.3.1 Stress distribution in the interlamellar non-fibrous matrix

The CIRC component of the Cauchy stress in the IL region was plotted at different applied stretches in Figure 3.6. A $250 \times 250 \mu m$ planar section oriented with the CIRC-LONG plane and centered on the domain. The section is shown in the deformed configuration and is taken directly below the collagen fiber network. The upper panels show the response of a representative BAV simulation and the bottom panels the response of a representative TAV simulation. To show the effect of the collagen fiber network on the non-fibrous matrix stress, the collagen network has been superimposed in all panels. Under low loads ($\lambda = 1.1$ and $\lambda = 1.25$ in Figure 3.6), less than the recruitment stretch of the collagen fibers, the matrix stress is homogeneous. A change in this behavior is seen above these stretches. By $\lambda = 1.35$, the average matrix stress in the representative BAV simulation was 210 kPa with a maximum and minimum of 550 and -60 kPa, respectively. Notably, the peak stresses are seen in regions of localized disruption of the fiber network in the CIRC (loading) direction. This trend was enhanced at an applied stretch of $\lambda = 1.5$. To wit, the maximum matrix stress was 1.8 MPa and the minimum stress -0.42 MPa. Similar trends were seen with the aneurysmal TAV tissue (Figure 3.6 lower panels). However, the peak stresses in the TAV simulations were lower than those for the BAV simulations.

To further examine the evolution of the IL matrix stress under applied stretch, the CIRC component of the Cauchy stress was extracted at each gauss point within the IL under the four stretches shown in Figure 3.6. The normalized frequency of the stress was plotted (Figure 3.7). A positive correlation between mean IL non-fibrous matrix stress and applied stretch was seen ($p < 0.01$). Standard deviation in the CIRC stress was below 10 kPa until $\lambda = 1.25$ - the recruitment stretch of the collagen fibers. Standard deviations above this stretch were significantly higher. Coefficient of variance increased from 0.1 below λ_r to 1.25 at λ_r. Levene's test showed no difference in variance in stresses below $\lambda = 1.25$ ($p > 0.05$) but significant difference above $\lambda = 1.25$ ($p < 0.01$).

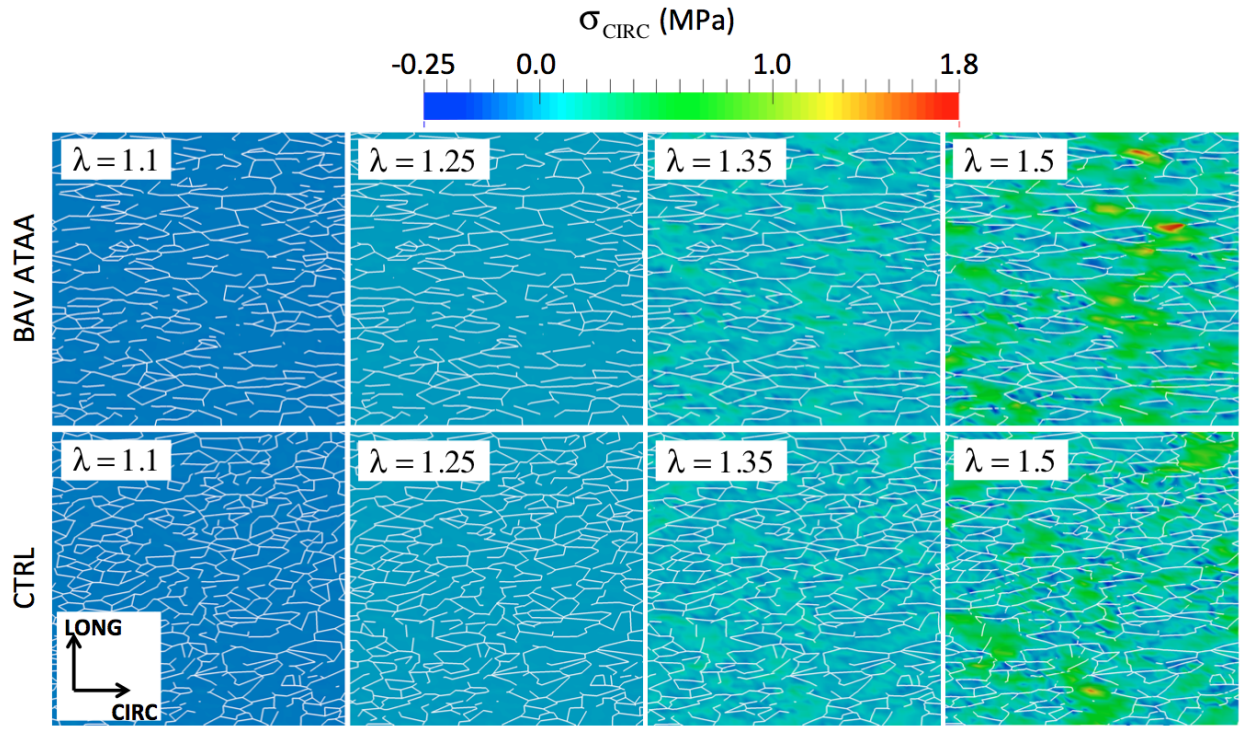

Figure 3.6: CIRC stress in the IL matrix for representative BAV (top) and TAV (bottom) simulations.

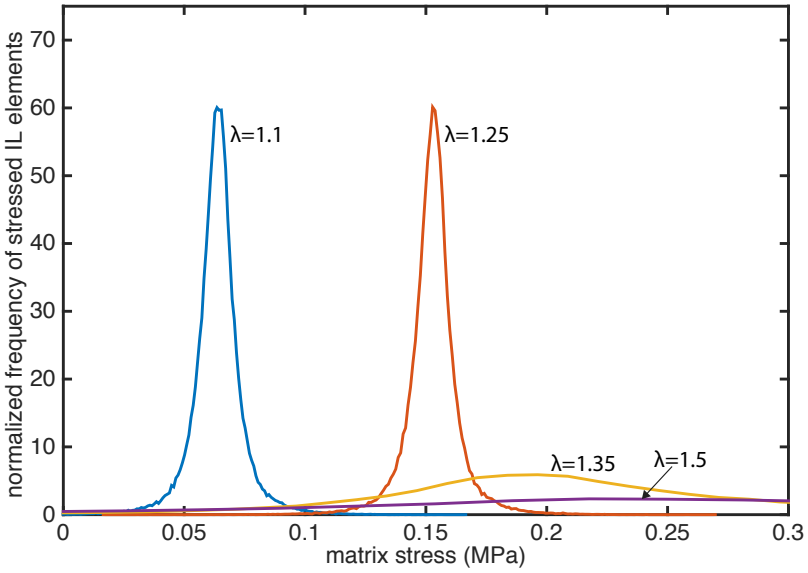

Figure 3.7: Heterogeneity of the CIRC stresses in the finite elements of the IL space increases with applied stretch.

In a similar manner, the mean and standard deviation of the von Mises stress in the matrix of the IL space was calculated at each load step for representative BAV (grey) and TAV (red) simulations (Figure 3.8). In the figure, the circles denote the average stress and the shaded region the standard deviation. Mean von Mises stress was approximately linear over the course of the simulation. Standard deviation of the stress however increased markedly after collagen fiber recruitment (at $\lambda = 1.25$). This increase in the standard deviation of the stress at higher applied stretches is due to the increasing heterogeneity in the stress state after the collagen fiber network begins to contribute to mechanical response of the tissue.

3.3.2 Fiber reorientation and recruitment with applied stretch

To examine the effect of the applied stretch on fiber recruitment and reorientation, the stress-state of each fiber was monitored at every increment of the applied stretch. The lengths of each fiber segment bearing load was added together and then divided by the total length of

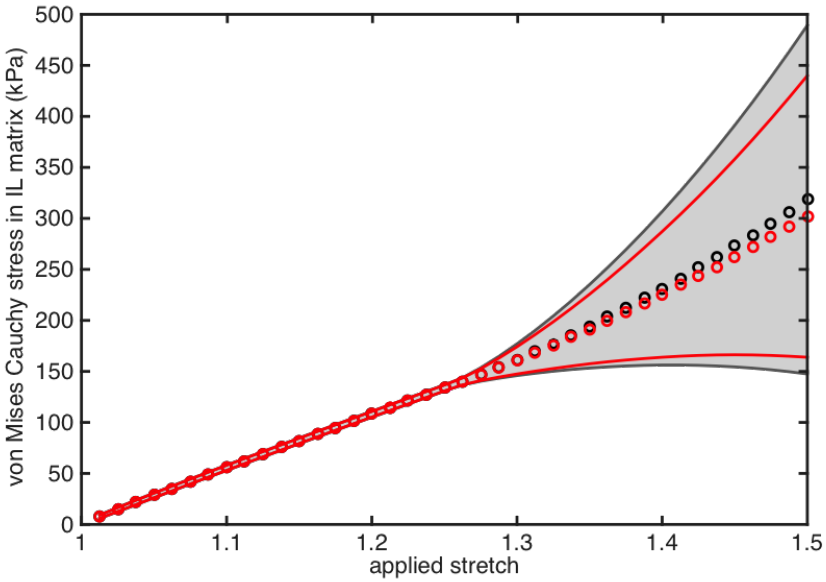

Figure 3.8: Evolution of IL stress (mean and standard deviation) for BAV (grey) and TAV (red) simulation.

the collagen fiber network to obtain the percentage of the collagen fiber network bearing load. Until the recruitment stretch of the collagen fibers ($\lambda_r = 1.25$), the collagen fiber network bore no load (Figure 3.9). At higher applied stretches, the percentage of the total network bearing load increases. The percentage saturates at approximately 90% of the total network. Thus, 10% of the fibers in the network do not bear load - even under high stretch. Collagen recruitment rate and saturation is not appreciably different for the other BAV simulations or for the TAV simulations.

The saturation of the percentage of the network bearing load suggests that not all collagen fibers in the network reorient with the loading direction. To study the reorientation of the network, the orientation of each collagen fiber segment was collected at five values of applied stretch: $\lambda = 1.0$, 1.1, 1.25, 1.35, and 1.5. At each stretch, the fiber orientations were gathered in 0.5° increments and fit to a normal distribution function. While most fibers in the network reoriented to the loading direction to an extent, the degree to which they reoriented depended on the initial fiber orientation as well as the magnitude of the applied stretch.

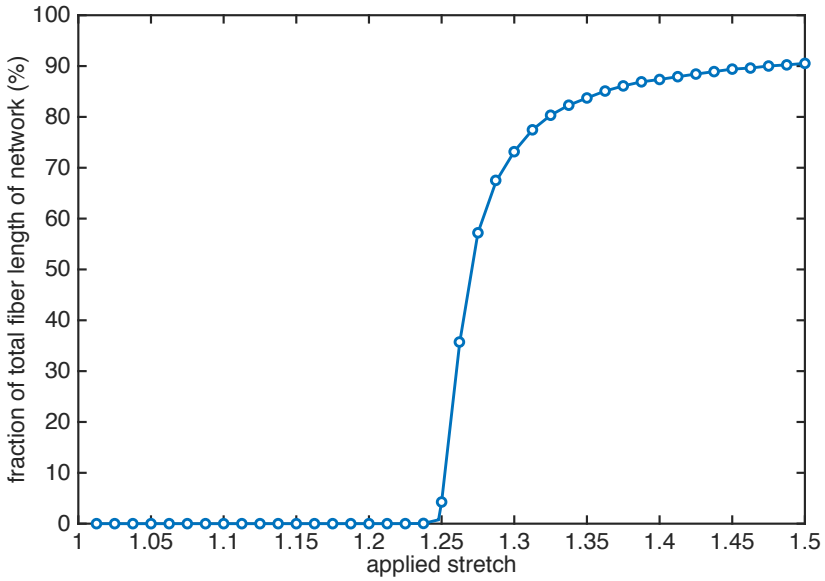

Figure 3.9: Percentage of the total collagen network bearing load with respect to applied stretch.

Inspection of the orientation distribution functions of the network at the five stretch levels, along with the actual network topology reveal that fiber reorientation began immediately at the onset of loading, even though the fibers were not bearing any load (Figure 3.10). The mean fiber orientation (CIRC) was maintained during applied stretch in the CIRC direction, and become more aligned with stretch as evidenced by the noted reduction in the standard deviation (Levene's test $p < 0.01$ for all combinations). NOI increased from 56% under no load to 62% at $\lambda = 1.5$. Change in the orientation of individual fiber segments depended on their orientation with respect to the loading direction. Of fibers with orientations between 30° and 60° from the CIRC direction, the mean change in angle was 9°. For fibers between 70° and 90° degrees however, the mean change in angle was 1°.

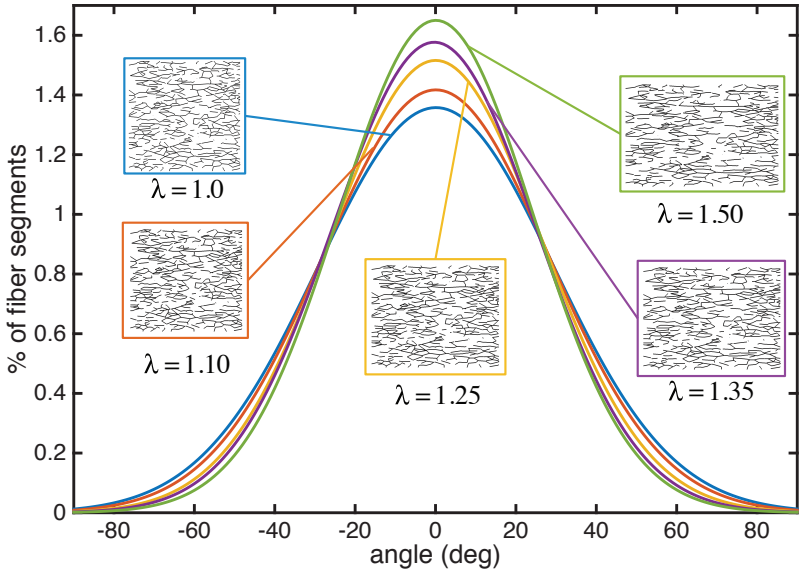

Figure 3.10: Fiber network OD at different applied stretches.

3.3.3 Stress in the fiber network

The model revealed a striking association between decreased fiber density and increased stress state within the non-fibrous matrix (Figure 3.11). The figure shows the stress in the fibers at different applied stretches. For comparison to the non-fibrous matrix, CIRC stress in the IL space matrix is shown in greyscale. A $250 \times 250\,\mu m$ planar section oriented with the CIRC-LONG plane is shown in the deformed configuration. Upper panels show the stresses for a representative BAV simulation and the bottom panels show the stresses fir a representative TAV simulation. At low stretches (up to λ_r), the fibers were unloaded. However, higher stretch levels ($\lambda = 1.35$ and 1.5 in the figure), the collagen fibers started to experience tensile stress. The magnitude of the fiber stress was heterogeneous. Segments aligned with the loading direction (CIRC) experienced the maximum stress while longitudinally oriented fibers remained unloaded. Further, some fibers followed continuous "stress paths" percolating between the loaded ends. [126] has demonstrated formation of such "stress paths" in the large strain response of biopolymer networks. They also suggested that reorientation of

these stress paths were a fundamental mechanism of stiffening in stretch-dominated regions. Additionally, we found that regions of fiber disruption in the loading direction (e.g. white arrows in Figure 3.11) was associated with focal regions of high stress in the non-fibrous matrix (lighter color in the IL matrix). At $\lambda = 1.5$, the stresses in the IL space were between 0.8 and 1.8 MPa. The collagen fiber stresses at the same stretch ranged from 8 to 10 MPa. These results suggest that there is a relationship between the local collagen fiber architecture and the non-fibrous matrix stress. To investigate this, the average matrix stress was plotted against the local fiber density at an applied stretch of $\lambda = 1.5$ for a representative BAV simulation (Figure 3.12. We considered all finite elements in the plane of the collagen fiber network. The "local fiber density" was calculated by dividing the total volume of collagen fiber in the finite element by the volume of the finite element itself. Stress at the gauss points of each element were averaged element-wise and plotted against the local fiber density. A negative correlation ($r = 0.65$, $p < 0.05$) was found between matrix stress and fiber density. For all simulations (BAV and TAV), a weak correlation was seen ($r = 0.2$, $p < 0.05$).

3.4 DISCUSSION

3.4.1 Structural model of the lamellar unit of aortic media recapitulates its constitutive behavior

Elastic lamellar units, the primary load-bearing structure of human ATA media, are arranged radially in a repetitive fashion in 4060 layers ([127]). Accordingly, we modeled a portion of the LU as the representative volume element of the aortic media (Figure 3.1). A representative collagen fiber network, constructed using empirically derived fiber network features from multi-photon microscopy, was directly incorporated in the RVE. Network features in addition to orientation distribution such as fiber intersection density, areal density, and average segment length can have a significant influence on network mechanics ([110, 112]). Our computational approach included all these network parameters, and also allowed for fiber-non-fibrous matrix interaction by the way of novel fiber-embedded finite element tech-

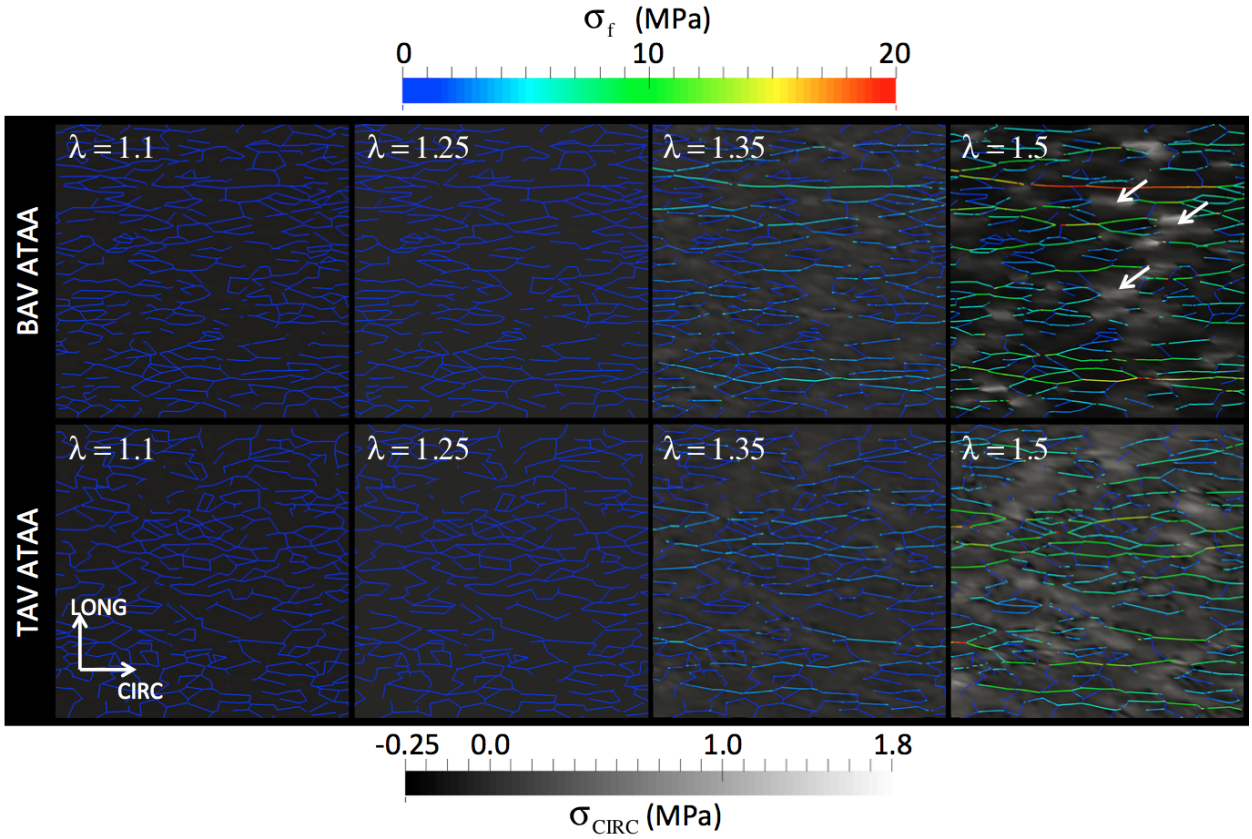

Figure 3.11: Fiber stress at different applied stretches.

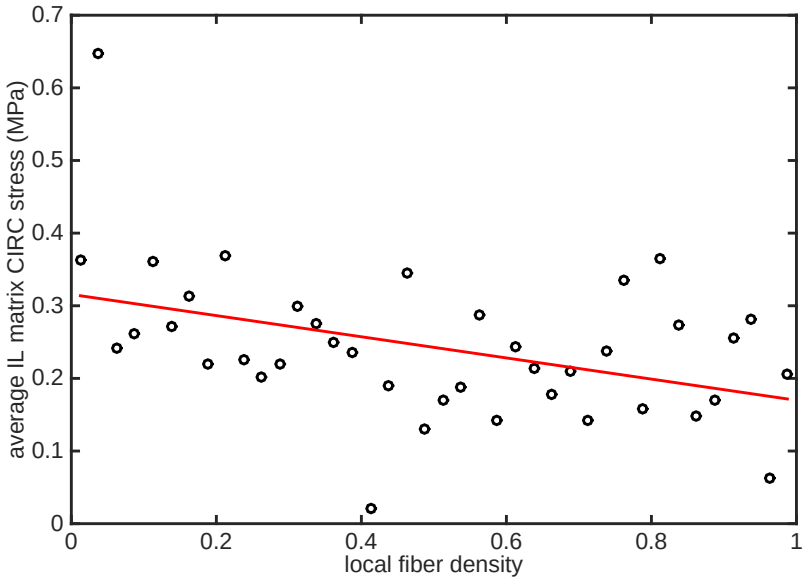

Figure 3.12: Average IL space stress vs. the local fiber density.

nique. The resulting model revealed heterogeneous non-fibrous matrix stress field in the human aortic media at higher applied stretch. Our approach is unique and in contrast with current structurally motivated models for the aortic wall, where an anisotropic and homogeneous media is assumed. Direct embedment of fibers within the non-fibrous matrix has been previously considered by [128, 129] in the general context of fiber reinforced soft tissue mechanics. However, in these works, the fibers were restricted to align with the edges of the finite elements making mesh generation a non-trivial task for large number of fibers. In contrast, our method incorporates multiple fibers in arbitrary orientation within a solid element thus rendering volumetric meshing a simple task. Our model correctly predicted the nearly linear elastin-dominated low stretch regimen as well as the linear collagen-dominated high stretch regimen. Gradual recruitment of collagen fibers, as predicted by our model, gave rise to nonlinearity of the response curve joining these linear portions (Figure 3.5).

3.4.2 Stress field in interlamellar matrix becomes heterogeneous after collagen fiber recruitment

We also show that the non-fibrous matrix stress became heterogeneous once collagen fibers started to transmit load, heterogeneities being markedly accentuated at higher stretch levels (Figure 3.6). Interestingly, the magnitude of stress heterogeneities differed between the simulated BAV and TAV ATA specimens. For example, at $\lambda = 1.4$, peak CIRC stress for BAV ATA specimens (660 KPa) was significantly different ($p = 0.047$) than that for TAV ATA (590 kPa) suggesting that difference in collagen microarchitecture between heart valve phenotypes may be an important factor influencing localized variations in the interlamellar stress field. The stress level in the collagen fibers also varied substantially, with fibers oriented in the loading direction carrying more stress (Figure 3.11). Fiber stress is concentrated on a small number of stress paths for the BAV ATA network while the stress is distributed among a majority of the aligned fibers in the TAV network. Additionally, fiber segments oriented within 70° of the loading direction continually reoriented thus altering the distribution of stress in the fiber network. Matrix stress heterogeneity is an outcome of local fiber network microarchitecture (e.g. density) as well as fiber-matrix interaction. Due to the assumption of perfect bonding between the fibers and the non-fibrous matrix, they deformed in an affine manner, a reasonable assumption for soft tissue mechanics ([130]). In presence of recruited fibers, matrix in the vicinity attempts to match fiber strain to maintain perfect bonding between them. Collagen fibers experience a higher stress and effectively shield the matrix because the collagen elastic modulus is at least an order of magnitude higher than the modulus for matrix ([125]). However, it can be noted from qualitative inspection of matrix stress heat maps overlayed with fiber network images that wherever the fibers are discontinuous in the loading (CIRC) direction, the intervening matrix stress is focally elevated in an attempt to match the stress state of the fibers in the vicinity (Figure 3.11). The correlation between decreased local fiber density and increased interlamellar matrix stress in the vicinity (Figure 3.12) raises the question of the potential for delamination in these regions. We noted that the stress heterogeneities manifested beyond the physiological range of wall stretch (approximately 1.2). Therefore, these findings might be more likely in

the setting of altered collagen microarchitecture in hypertensive patients. Locally elevated stress can adversely affect the biology of the aortic wall as VSMCs are mechanosensitive ([131]) and stress state can alter their phenotype ([132]). The impact of VSMC-matrix interactions on local stress will require further investigation. Taken together with recent work from our group and others ([133, 5, 75, 134]) these results indicate a role for collagen network microarchitecture architecture in aortic wall biomechanics.

3.4.3 Limitations of the current work

Our computational model for the human thoracic aortic media has some limitations. We assumed the interlamellar matrix to be homogeneous to act as a single material in our model. The multicomponent nature of the IL space along with contractile forces from the VSMCs can alter the stress state of aortic media. However, heterogeneities in the IL matrix material are expected to contribute to fluctuations in the stress field, and thus our basic conclusions will likely not change. Furthermore, we did not consider mechanical failure of any of the model components. Our model predicted markedly high stresses which could lead to failure of the fiber matrix and hence, alteration of stress distribution. Finally, we have considered only uniaxial stretching of the aortic media. It will be interesting to examine whether our model can capture constitutive responses under multiaxial loading, which is a topic of our future research.

3.5 CONCLUSIONS

We have presented a finite element structural model of the aortic media considering its lamellar architecture. An important aspect of our approach is the use of only experimentally-derived information as model parameters. The model correctly reproduced nonlinear mechanical response of the wall tissue and importantly, revealed a heterogeneity in the stress state of fibers and matrix throughout the entire stretching event. We found that fiber-matrix interaction, combined with local fiber microarchitecture, gave rise to heterogeneous stress

field within the aortic media after the fibers started taking load. Fluctuations in the interlamellar matrix stress continually increased with applied stretch, creating regions of higher stress that local VSMCs could experience.We expect that our computational approach will provide insight into the role of structural changes of the aortic wall and ensuing wall tissue biomechanical response on the pathophysiology of aortic disease, such as aneurysm and dissection, and contribute metrics from non-invasive clinical imaging data to help guide clinical decision-making and care of patients with aortic disease.

4.0 QUANTIFICATION OF TISSUE FAILURE AT THE MICROSCALE

4.1 INTRODUCTION

The data described in this chapter has been published in [135]. The chapter will describe an extension of the previous chapter adding failure of the collagen fibers under uniaxial loading.

Acute aortic dissection of the ascending thoracic aorta (ATA) is a major health concern with high mortality, particularly in the absence of surgical intervention. The dissection typically initiates from an intimal tear in the ATA wall and propagates transmurally before delaminating the media layers (Figure 4.1a). If left surgically untreated, the mortality rate is 1-1.4% per hour for the first 48 hours [9] which compounds to more than 60% by 2 weeks [10]. The primary strategy for prevention of acute aortic dissection (AoD) is emergent elective surgery for patients with a maximal orthogonal aortic diameter greater than 5.5 cm [136, 137]. However, 59% of the patients who experience acute dissection of ATA have an aortic diameter less than 5.5 cm [34]. Thus, there is an unmet clinical need for the formulation of evidence-based metrics for earlier and more accurate identification of patients at high risk of dissection. Failure mechanics of the vessel wall is expected to play a major role in the derivation of such metrics as dissection ultimately results from the lack of structural integrity of the wall.

Dissection propagation from an intimal tear (Figure 4.1a, middle) initiates an instantaneous sequence of biomechanical events leading to the separation of vessel wall layers (Figure 4.1a, bottom). The initiation event takes place when in-plane wall stress exceeds the in-plane wall strength creating a radially-oriented tear through the media. Vessel wall tissue derives its mechanical strength from the content and organization of the structural proteins, namely elastin and collagen, within the extracellular matrix (ECM) [138, 139, 140, 141, 49]. *In vitro*

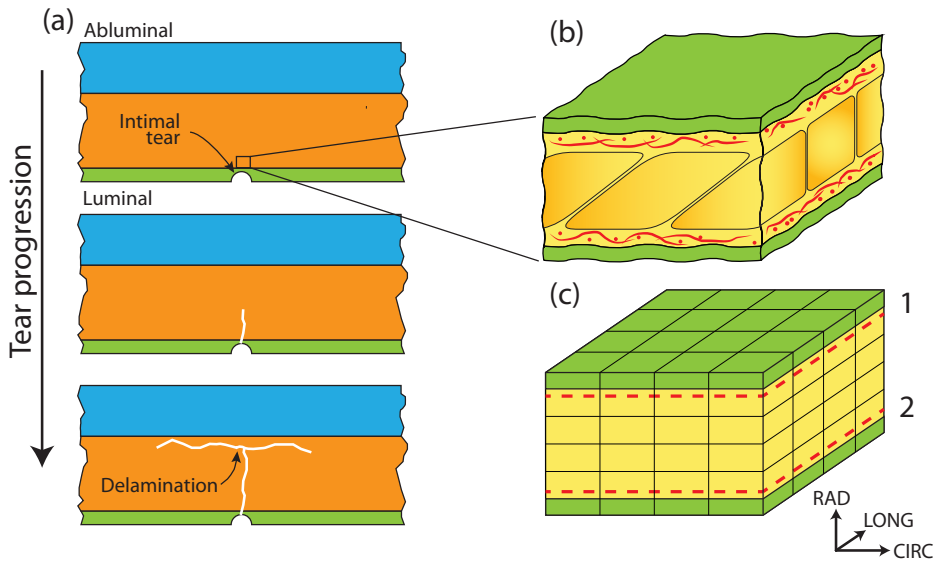

Figure 4.1: (a) Typical evolution of an aortic tear. (b) The lamellar unit of the aortic media. (c) A portion of the representative volume element of the lamellar unit.

experiments suggest that degradation of collagen fibers causes decreased tissue strength [141, 49]. Uniaxial strength in the circumferential (CIRC) direction of the aortic wall tissue was found to be significantly higher than in the longitudinal (LONG) direction [142, 75, 134]. These observations, along with the reports of anisotropic collagen fiber distribution in aortic medial ECM [1, 5], suggest that the tissue strength is influenced by collagen fiber organization. Damage-based structural models of the aortic tissue help to accrue mechanistic understanding of the tissue failure [115, 143, 144, 98, 62, 145]. Cohesive zone models where tissue is described as a continuum and potential failure planes were enriched with a failure law, address tear propagation in the aortic tissue [96, 66, 146]. Barocas and collaborators have developed multiscale models for porcine aortic tissue incorporating elastin and collagen fiber organization [104, 122]. These modeling efforts, in conjunction with the experimentally-derived data on tissue strength and microarchitecture, contribute to our current understanding of the structural basis of the vessel wall failure. Still, how collagen fiber architecture of the human ATA tissue in health and aneurysmal disease influences its failure properties is incompletely understood, and this could be critical is fully understanding AoD.

The goal of this study was to identify the structural features of the collagen fiber network that govern the strength of healthy and aneurysmal human ATA wall tissue. To accomplish this goal, we utilized a structural finite element model for the lamellar unit of the media of the human ATA wall, the layer in which the dissection primarily propagates. Organization of the collagen fibers in the ATA wall of non-aneurysmal and aneurysmal patients, previously obtained by multiphoton microscopy (MPM) image analysis [1], was explicitly incorporated into the model. We hypothesized that the tissue failure strength is governed by the orientation of the collagen fibers within the ECM. To test this, we simulated uniaxial tensile behavior of the ATA wall tissue in circumferential and longitudinal directions for three patient cohorts. The model parameters were calibrated by regressing model uniaxial pre-failure and failure response against the experimental response in the circumferential direction. The model, thus calibrated, could predict the tissue strength in the longitudinal direction with excellent accuracy ($p > 0.05$). This suggested that the essential tissue failure mechanisms were captured by our model. Quantification of the relationship between the tissue strength and microstructural features of the collagen network revealed the primary role of the collagen fiber orientation distribution.

4.2 METHODS

4.2.1 Human ATA tissue specimen preparation and uniaxial testing

Previously determined [75] uniaxial tensile strength of human ATA tissue were utilized in the present work. In brief, aneurysmal ATA wall tissue was previously collected during elective surgery for ascending aortic replacement or aortic valve replacement from patients with bicuspid ($n = 23$) or tricuspid aortic valve ($n = 13$) with Institutional Review Board (IRB) approval and informed patient consent. These two cohorts were designated as BAV and TAV, respectively. Control ATA tissues were also collected from heart transplant donors and recipients with tricuspid aortic valve and no aortopathy ($n = 7$), designated as CTRL, with approval from the Center for Organ Recovery and Education or IRB, and informed

patient consent. Multiple specimens were cut from the wall tissue of each patient in both CIRC and LONG directions, resulting in a total of 15 CIRC and 11 LONG specimens for the CTRL group, 28 CIRC and 31 LONG specimens for the TAV group, and 54 CIRC and 50 LONG specimens for the BAV group. These specimens were tested uniaxially in a displacement-controlled manner until failure. We reported details of sample preparation, uniaxial testing protocols, and strengths in our earlier publications [140, 75].

4.2.2 Structural model of aortic media

We created a solid model for the lamellar unit (LU) of the ATA media tissue and accounted for the organization of elastin and collagen fibers. Two elastic lamellae (EL), separated by an interlamellar (IL) space of 11 μm [45], were modeled as a 3D continuum of dimension $250\mu m \times 250\mu m$, see Figure 4.1b,c. The thickness of each lamella was taken to be 0.75 μm, half of its physiological dimension [44], as the lamellae are shared by adjacent LUs. The resulting volume fraction of the EL (vf_{elast}) was calculated as 0.12, and that for the IL space (vf_{il}) was 0.68. Collagen fiber networks were placed in the IL space adjacent to each elastic lamella. Individual collagen fibers of the network were modeled as one-dimensional rod elements of 3 μm diameter [2, 106]. We developed a custom Matlab (Matlab 2014b, Mathworks, Natick, MA) script to create planar networks of collagen fibers quantified by mean fiber direction (γ), orientation index (OI), and areal density (AD) obtained from multiphoton image analysis for each patient cohort and previously reported in [1, 5, 2] (Table 4.1). Pichamuthu, et al. [75] showed that there was no significant difference in the collagen content between the CTRL and aneurysmal populations. For this reason, the same value of AD of 0.48 [2] for all cohorts was used, resulting in a collagen volume fraction (vf_{col}) of 0.20. Fibers were added to the network until the target AD was reached with the angle of individual fibers normally distributed about γ using OI. After network creation, we verified normalcy of the fiber distribution using a Lilliefors test ($p \leq 0.05$). Similar fiber network generation algorithms have been presented by other researchers [104, 110, 119, 130]. The resulting fiber networks were symmetrically arranged with respect to the circumferential

direction of the vessel [147] with a mean fiber direction of $+\gamma$ for the network in layer 1 and $-\gamma$ for the other (Figure 4.2).

Table 4.1: Collagen network statistics from Pasta et al.[1] and Koch et al.[2].

Population	γ (degrees)	OI	AD
CTRL	± 11	0.67 ± 0.01	0.473
TAV	± 35	0.60 ± 0.01	0.488
BAV	± 30	0.63 ± 0.01	0.480

Elastic lamellae and interlamellar space were modeled with a 1-parameter isotropic incompressible neoHookean material model with a strain energy function $\Psi = 0.5\mu(I_1 - 3)$, with μ the shear modulus and $I_1 = \text{tr}\mathbf{C}$ the first invariant of the right Cauchy-Green deformation tensor. Full finite element implementation of this model is given in Appendix A.2. Based on our previous work [106] with the addition of fiber damage, the collagen fibers were modeled with the following stress-stretch relationship

$$\sigma = \begin{cases} 0 & \text{if } \lambda < \lambda_r \\ E_{col}\,(\lambda - \lambda_r)\,S & \text{if } \lambda > \lambda_r \end{cases} \tag{4.1}$$

with E_{col} representing the collagen fiber stiffness and the λ_r the recruitment stretch. λ is the current stretch of the fiber. To account for damage in the fiber, the parameter $S \in [0.1]$, an internal variable tracking the current fiber damage, was included. The damage parameter remained at its initial value $S = 1$ until the peak stretch of the fiber (λ_p) was reached. After that instant, S monotonically decayed between the fiber stretches of λ_p and λ_{max}, the failure stretch of the fiber. In the event of unloading, S for the fiber remained constant to allow for the fiber to follow the same unloading path upon subsequent loading of the fiber. At and beyond the failure stretch, the fiber was fully failed ($S = 0$) and the thus did not bear further load, even under potential unloading. Evolution of S is based on previously reported work by Maiti and Geubelle[148] and is given by

$$S = \min\left[S_{min}, \langle 1 - \frac{\lambda - \lambda_p}{\lambda_{max} - \lambda_p}\rangle\right] \tag{4.2}$$

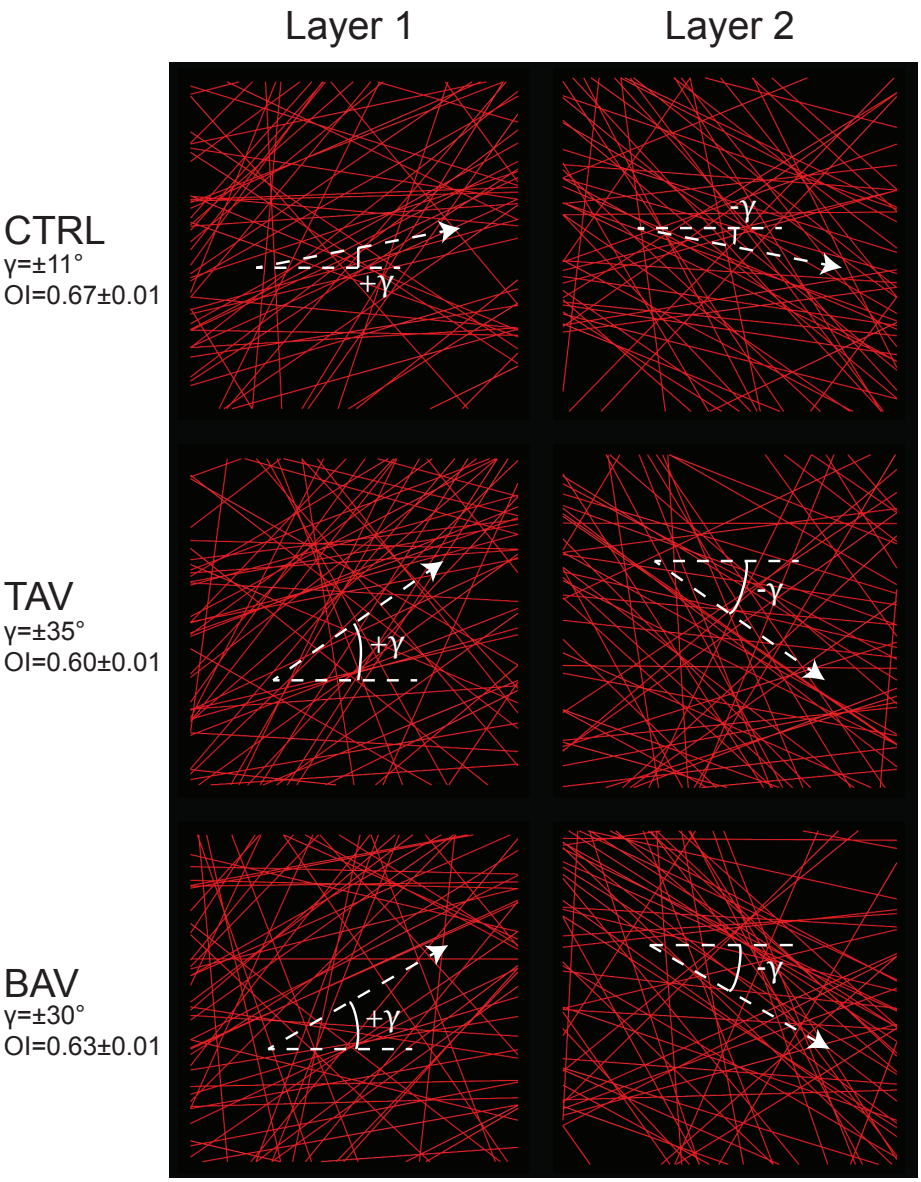

Figure 4.2: Collagen networks in layer 1 (left) and layer 2 (right) for CTRL, TAV, and BAV populations.

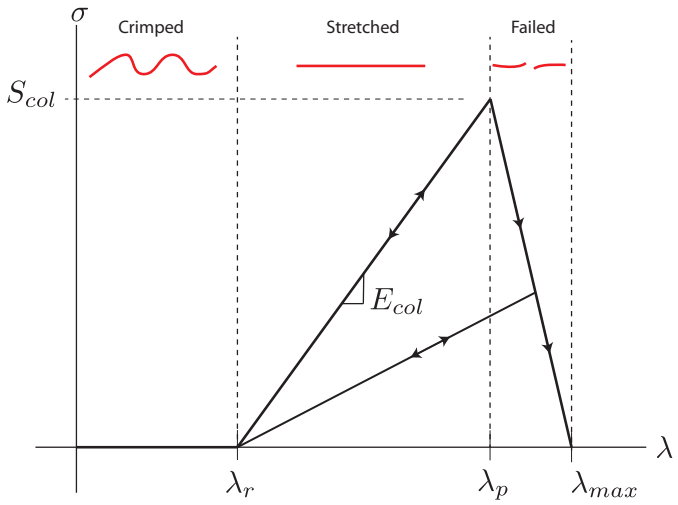

Figure 4.3: Constitutive relationship of an individual collagen fiber.

where $S_{min} \geq 0$ is the minimum value of S over the course of the simulation. The operator $\langle a \rangle$ is defined as

$$\langle a \rangle = \begin{cases} a & a > 0 \\ 0 & \text{otherwise} \end{cases} \tag{4.3}$$

4.2.3 Finite element simulation procedure and model parameter estimation

A custom embedded-fiber finite element model (detailed in Chapter 3, Appendix 2) was used to simulate uniaxial tensile tests on the computational domain. Tensile stretch was applied uniaxially over 1000 load steps in either the CIRC or LONG direction until the tissue stress reached the post-peak region. Faces orthogonal to the loading direction were placed on rollers. Reaction forces at all the nodes in the loaded face were recorded throughout the course of the simulation. These forces were post processed to compute overall tissue stress for the stress-stretch curve. To ensure convergence, simulations were run with different mesh densities until the change in peak stress was less than 5%. These studies showed that 15,000 8-noded hexahedral elements were sufficient for a converged result.

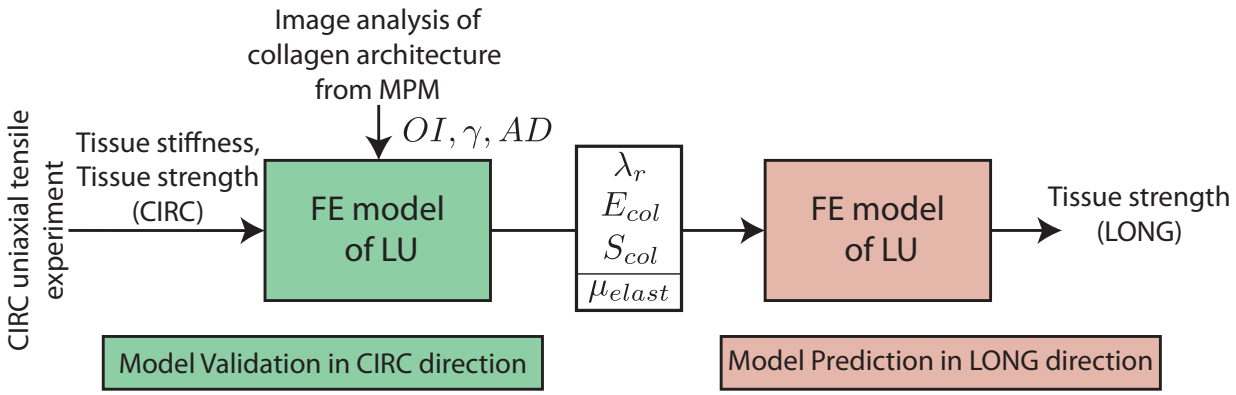

Figure 4.4: Process of CIRC response validation and LONG response prediction.

For all three patient cohorts, experimentally-measured uniaxial stress-stretch data in the CIRC direction provided model validation and parameter calibration, while those in the LONG direction were used to assess the accuracy of model prediction. Figure 4.4 schematically depicts the model validation and prediction procedure. For each patient, we averaged all experimental stress-stretch curves in the CIRC direction to yield the mean CIRC response. The computational domain was then uniaxially stretched in the CIRC direction and resulting stress-stretch curve was compared against the corresponding experimentally measured mean CIRC response for model validation. Four material parameters: shear modulus of elastic lamellae (μ_{elast}), as well as the elastic modulus (E_{col}), recruitment stretch (λ_r) and failure strength (S_{col}) of the collagen fibers, were calibrated. The IL space is primarily comprised of a mixture of elastin and collagen fibers, smooth muscle cells, and proteoglycans [43, 44], and thus is expected to be softer than the lamellae. Accordingly, we assumed IL space shear modulus to be 1/3rd of μ_{elast} for all simulations.

Material parameter calibration was performed for each patient by regressing the simulated stress-stretch curve against experimentally-measured mean CIRC response using the nonlinear least square fitting function lsqcurvefit in Matlab. As the initial low stiffness segment of the tissue stress-stretch response is governed by mechanical properties of elastin [76], the computational curve was fitted against the experimental data in this region to determine

μ_{elast}. The mean value of λ_r was determined from the location of inflection point in the experimental stress-stretch curve. Regression of the stiffer quasilinear region of the tissue stress-stretch response calibrated the collagen fiber elastic modulus E_{col}. Fitting the peak of the stress-stretch response determined the collagen fiber failure stress, S_{col}.

Population averages for each material parameter were computed after the patient-specific fitting was complete. Students t-test and Levenes test were used to determine statistical difference in the mean and variance, respectively, between the experimentally measured and computer simulated tissue failure stress and stretch. For both tests, $p < 0.05$ indicated a difference in means between the patient groups. Unless noted otherwise, reported values are given as (mean $\pm$ standard deviation).

With the completion of the model parameter calibration step, the domain was uniaxially stretched in the LONG direction using calibrated model parameters. Multiple simulations were run with different combinations of mean and $\pm$SD values of each model parameter. Comparison of the predicted LONG response and the experimental data were assessed using the same statistical tests as in CIRC calibration step.

4.3 RESULTS

Figure 4.5 presents the simulated and experimental CIRC stress-stretch responses (red and grey, respectively) for representative patients selected from each of the three populations. The coefficient of determination between average experimental and simulated stress stretch curves for the CTRL cohort was 0.99 ± 0.01, while those for the BAV and TAV cohorts were 0.98 ± 0.03 and 0.96 ± 0.03, respectively. Regressed model parameters for all the cohorts along with their experimentally measured values gathered from the literature are listed in Table 4.2. We found that all the regressed parameter values were in the vicinity of their experimentally measured magnitude.

Simulated uniaxial failure properties of the tissue, namely failure stress and failure stretch, in the CIRC direction are shown in Figure 4.6a and b, respectively. Corresponding experimentally measured values for these properties were also listed in these figures for the

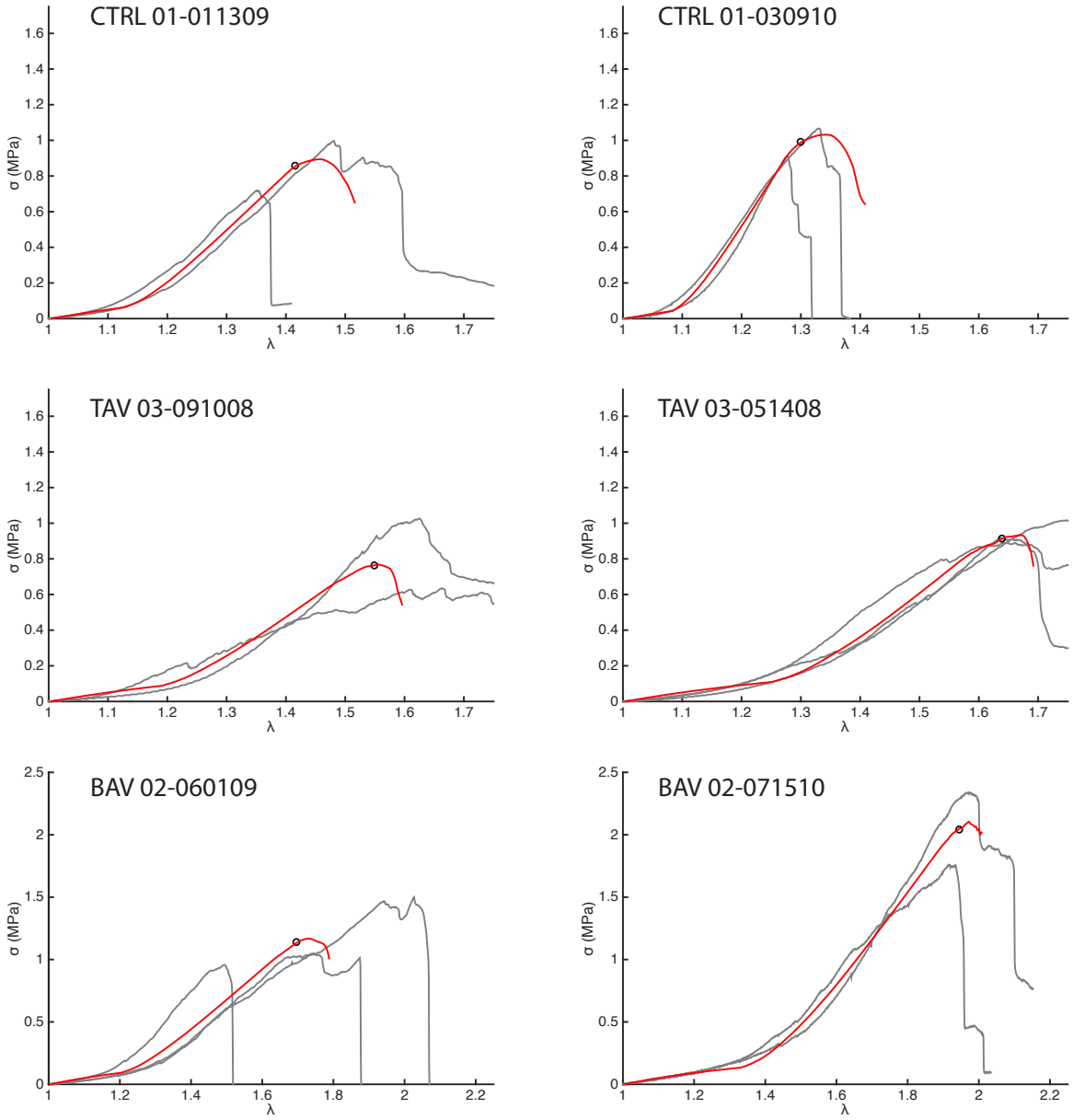

Figure 4.5: Representative CIRC fitting of computational RVE (red) to experimental data (grey).

Table 4.2: Fitted material parameters for CTRL, TAV, and BAV populations.

	Simulation Material Parameters			Literature
Population	CTRL	TAV	BAV	
μ_{elast} (kPa)	321 ± 102	349 ± 83	347 ± 68	100-1000 [125]
E_{col} (MPa)	23.1 ± 6.5	22.4 ± 10.7	19.8 ± 9.0	54 ± 25 [79]
S_{col} (MPa)	8.17 ± 2.19	6.95 ± 4.32	12.89 ± 7.02	8.5 ± 2.6 [79]
λ_r	1.19 ± 0.07	1.24 ± 0.13	1.30 ± 0.10	1.2-1.4 [118]

comparison purpose. Mean failure stress and failure stretch for the simulation derived and experimentally measured failure properties of the tissue in the CIRC direction was equivalent for all populations ($p > 0.05$). In addition, there was no difference in the variance of the failure stress and stretch data in the CIRC direction (Levenes test $p > 0.05$).

The model tissue was next stretched uniaxially in the LONG direction. The model parameters were fixed at their CIRC regressed magnitudes, as listed in Table 4.2. Simulation predicted tissue failure stress and stretch values in the LONG direction, along with their experimentally measured values, are shown in Figure 4.7a and b, respectively. Mean failure stress and stretch between the simulation predicted and experimentally measured data in the LONG direction were similar ($p > 0.05$) in all three cohorts. Moreover, Levenes test showed no significant difference between the variances of the experimentally measured and simulation predicted data. These statistical outcomes indicate accurate tissue failure prediction capability of our aortic media model.

The simulated evolution of maximum principal stress for CIRC stretching of the CTRL and TAV tissues shown in Figure 4.8 reveals the stress in the CIRC-LONG plane with proximity to the collagen network layer. An applied stretch of 1.1 resulted in unloaded collagen fibers and uniform stress in the non-collagenous matrix (Figure 4.8a). At an applied stretch of 1.3, the collagen fibers oriented within $\pm 30^{\circ}$ of the CIRC direction were recruited

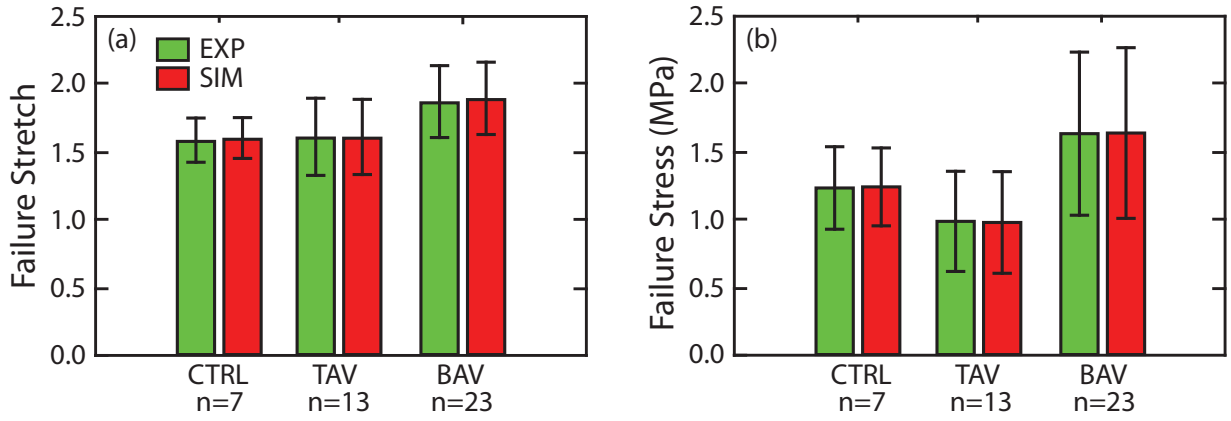

Figure 4.6: Failure stretch (a) and stress (b) in the CIRC direction (mean and standard deviation).

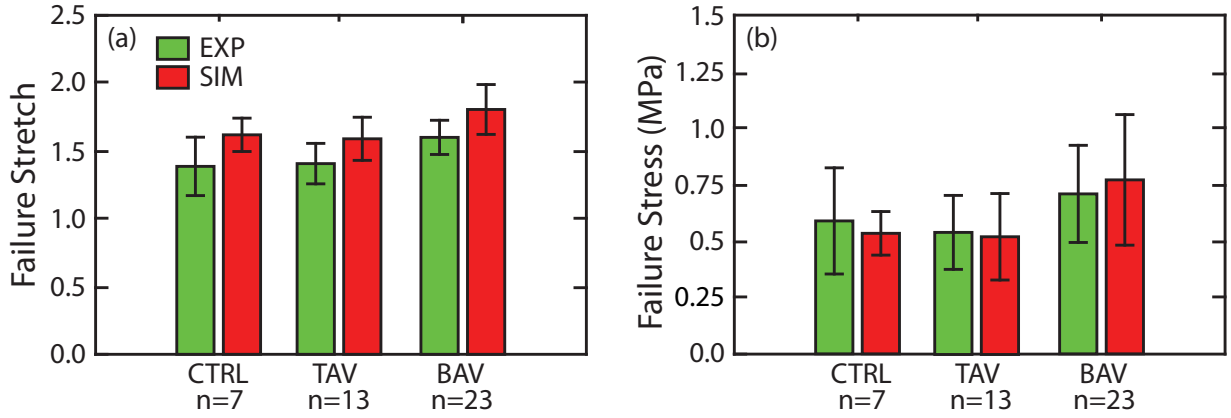

Figure 4.7: Failure stretch (a) and stress (b) in the LONG direction (mean and standard deviation).

and started bearing load while fibers not oriented with the CIRC direction remained unloaded (Figure 4.8b). Consequently, the stress transfer from the fibers to the surrounding matrix was not found to be uniform resulting in heterogeneous stress state in the matrix. At an elevated stretch of 1.45, collagen fibers in the loading direction began to fail. The matrix stress in the regions of collagen fiber failure was concomitantly elevated with respect to the rest of the domain, suggesting simultaneous colocalized failure of the non-collagenous matrix.

We observed similar evolution of the stress distribution when the tissue models were stretched in the LONG direction (Figure 9). Under low loading (below the recruitment stretch of the collagen fibers), the matrix stress was homogeneous with unloaded collagen fibers (Figure 4.9a). Heterogeneity in the matrix stresses was observed with collagen fibers recruitment and load bearing (Figure 4.9b). Marked increases in matrix stresses were noted in localized regions of the domain with fiber failures at elevated stretch (Figure 4.9c)., The number of highly stressed fibers in the LONG direction was reduced when compared with CIRC loading case, due to the correspondingly lower number of fibers oriented. Consequently, fewer individual fiber failure events occurred in the LONG direction compared to the CIRC direction. Qualitatively similar evolution of stress in the pre-failure and failure regime was observed for BAV tissues.

4.4 DISCUSSION

The evolution of AoD takes place in two primary stages: dissection initiation from an intimal tear, and mural propagation through aortic media leading to separation of media layers. A number of prior studies have focused on the mechanics of wall delamination due to dissection propagation [66, 72]. Pal et al. found that the delamination strength of both healthy and diseased ATA wall tissue was related to the radially running fibers in the media [66]. The mechanism of dissection formation from glycosaminoglycans within the aortic media has recently been reported [149, 63]. These reports have contributed to our understanding of dissection propagation mechanisms within the media. Another major area of concern is the mechanics of dissection initiation from an intimal tear, which is governed by the in-

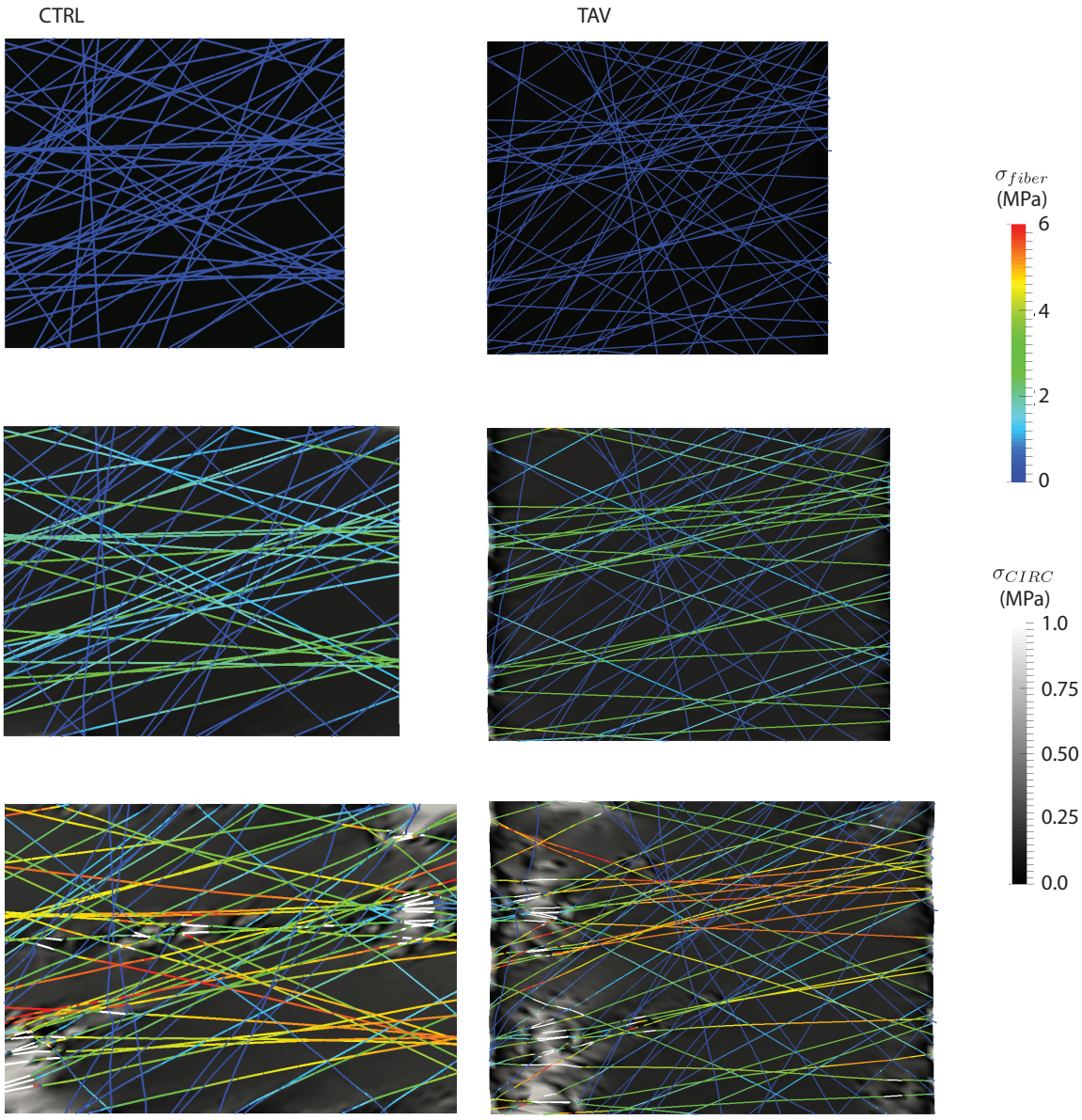

Figure 4.8: Fiber and matrix stress for representative CTRL and TAV patients under CIRC loading at $\lambda = 1.1$, 1.3, and 1.45.

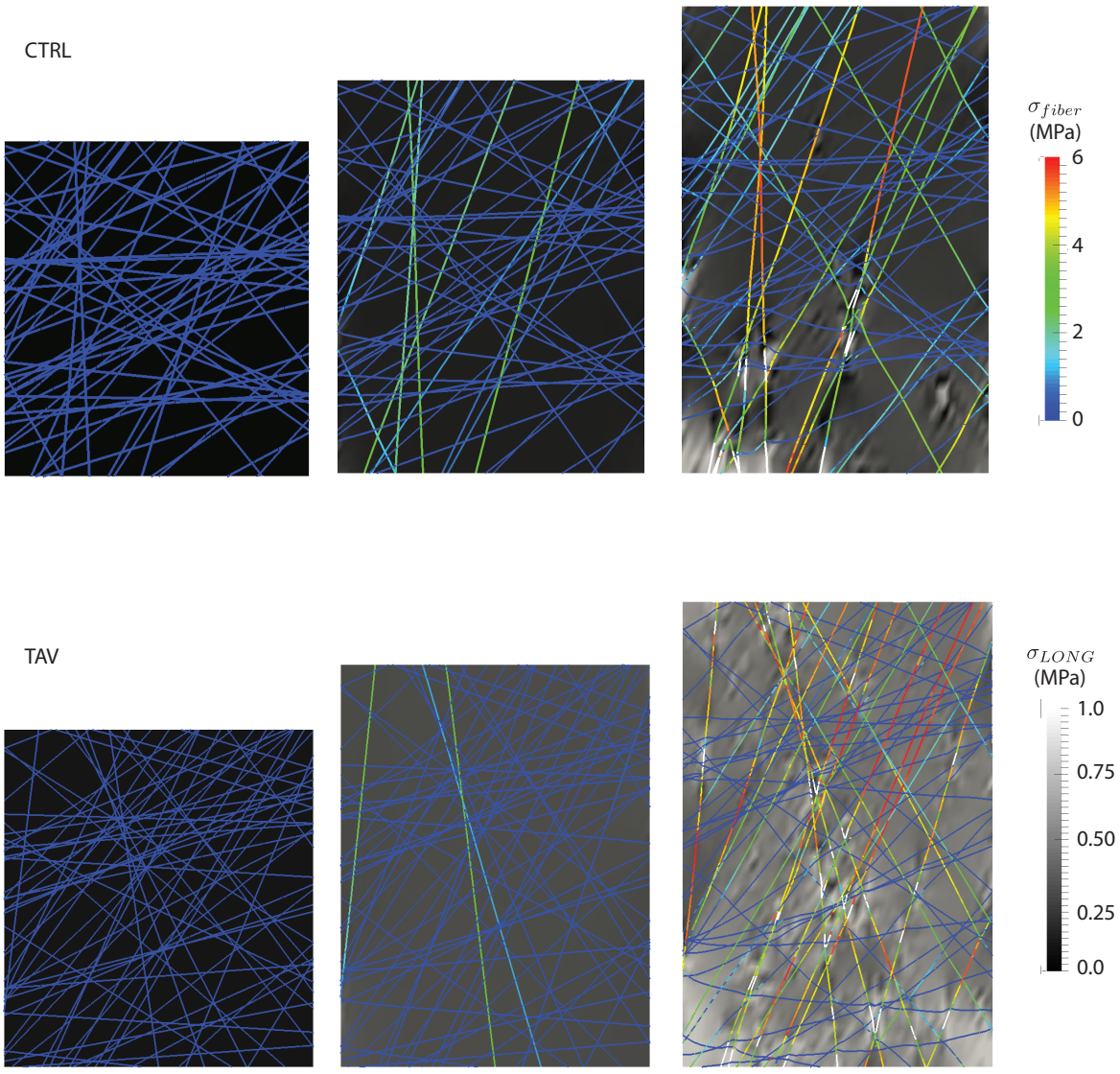

Figure 4.9: Fiber and matrix stress for representative CTRL and TAV patients under CIRC loading at $\lambda = 1.1$, 1.3, and 1.5.

plane failure mechanics of the ATA wall. Increased wall stress in the ascending thoracic aorta was suggested as a possible mechanism for the propagation of dissection from intimal tears in the ATA wall [150, 151]. Formation of aneurysm [151], aortic root motion and hypertension [64, 152] was postulated as possible causes for the increase in the wall stress. However, how the tissue structure of the healthy and diseased ATA wall is related to the tissue strength is not known yet. Our goal in this work was to identify the microstructural mechanisms leading to ATA tissue failure under in-plane loading conditions, and quantify their contributions towards in-plane tissue strength.

We obtained MPM imaging-derived population-specific collagen fiber orientation and areal density data from our prior work [5, 2], and incorporated them into our model through a novel fiber-reinforced finite element technique [106]. Fiber stress in excess of fiber strength, defined as the maximum stress a fiber can bear without failure, was considered as the fiber failure criterion. All the free parameters of the model, listed in Table 4.2, were calibrated for each patient cohort by regressing the simulated CIRC stress-stretch curves against experimentally measured CIRC response. As these parameters are intrinsic mechanical properties of the tissue constituents, they were assumed not to vary with the loading direction. Next we stretched the finite element model longitudinally with free parameters fixed at magnitudes derived from CIRC simulations; see the schematics in Figure 4.4. Simulation-predicted LONG failure properties of the tissue exhibited a striking fit with the experimentally measured LONG failure properties for all patient cohorts (Figure 4.7). As the only failure mechanism considered in our model was the failure of individual collagen fibers, our results suggest that the tissue failure properties are governed by the failure of collagen fibers; which in turn depends on the mechanical properties of individual fibers and their orientation within the vessel wall. However, Table 4.2 shows that regressed mechanical properties of the collagen fibers were similar among patient cohorts ($p > 0.05$) (fiber strength for BAV cohort was higher than for other cohorts, although we did not find a statistically significant difference). In addition, the collagen content for all the cohorts was kept constant, in accordance with [75]. Thus, our simulation results suggest that the difference in tissue strength among cohorts are likely due, at least in part, to their distinct collagen fiber architectures. Recent experiments of *ex vivo* degradation of the aortic tissue collagen revealed that the

wall strength correlated with collagen content [141, 49]. Deleterious effect of aging on the tensile strength of the aneurysmal sinus tissue was demonstrated by Iliopoulos et al. [153]. Pichamuthu et al.[75] demonstrated that both the CIRC and LONG tensile strengths were higher in ATA aneurysms from aneurysmal patients with BAV when compared with patients with TAV. Phillippi et al. [5] reported distinct collagen fiber microstructure in the aortic media matrix for aneurysmal BAV and TAV tissue. Taken together, these studies support finding of prior work (Refs [142] and [1]) by demonstrating how collagen fiber organization directly influences tissue strength in human aorta. In this report, we demonstrated that distinct arrangement of collagen fibers within the ATA media matrix of healthy and diseased tissues can explain the difference in the strength of these tissues.

We enumerated the evolution of stress in the collagen fibers and non-collagenous matrix during uniaxial stretching for CTRL and TAV tissues, as shown in Figures 4.8 and 4.9. Stress evolution in BAV tissues, not shown here, also follows a similar pattern. We found that the imposed load was born by the non-collagenous matrix at low stretch levels until the collagen fibers were recruited, resulting in the initial low stiffness region of the stress-stretch curve for the tissue. Once recruited, the collagen fibers provided the additional load bearing mechanism for the tissue, resulting in a dramatic increase of the tissue stiffness. However, only a fraction of available collagen fibers carried the load imposed on the tissue segment, resulting in distinct stress paths within the tissue along the loading direction [106]. Magnitude of fiber stress was dependent on the fiber orientation with fibers aligned with the loading direction experiencing higher stress levels. Fibers that were almost orthogonal to the loading direction did not participate in the load-bearing mechanism. Percentage of load-bearing fibers for all patient cohorts at the instant of tissue failure for both CIRC and LONG loading directions are listed in Table 4.3. As the mean orientation of collagen fibers were at an acute angle to the CIRC direction for all populations (Table 4.1), more fibers participated in the CIRC load-bearing mechanism than when the tissue was loaded in the LONG direction. With further increase in the applied stretch, highly stressed collagen fibers failed in a localized manner resulting in a drastic reduction of the tissue stress. Non-collagenous matrix stress at the locations of fiber failure exhibited sharp peaks in excess of 3 MPa for all cohorts, far greater than the ultimate stress of 1.38 ± 0.08 MPa for elastin [78].

This localized rise in the matrix stress was a result of the stress transfer from the broken fibers to the proximal non-collagenous matrix due to fiber-matrix interaction. Although matrix failure was not explicitly modeled in our work, these high focal stresses in the matrix are likely to cause matrix failure collocalized with the fiber failure, and lead to eventual tissue failure. Barocas and collaborators have recently studied the failure of porcine aortic tissue using a multiscale modeling technique [104, 122]. They subjected the tissue model to various loading conditions in addition to the uniaxial cases, and also identified that collagen fiber failure was the predominant mechanism for tissue failure for all the loading scenarios they considered.

Table 4.3: Percentages of load bearing fibers in the network at the onset of failure under CIRC and LONG loading for CTRL, TAV, and BAV tissue. A wide range of sample-to-sample variation for LONG cases could be found for all patient cohorts. This variation was due to substantial reorientation of the fibers in the LONG direction during loading.

Population	Max % of load bearing fibers	
	CIRC	LONG
CTRL	90 ± 2	33 ± 21
TAV	82 ± 6	30 ± 20
BAV	87 ± 2	30 ± 19

Our computational results suggested that the primary load bearing mechanisms at the point of tissue failure are the loaded collagen fibers and non-collagenous matrix components. For a first order quantification of the relationship between these mechanisms and tissue strength, we approximated the tissue as a linear elastic composite material, and estimated the tissue strength S_{tissue} using the rule of mixture [154]

$$S_{tissue} = vf_{col} N_f S_{col} + vf_{elast} E_{elast} (\lambda_{fail} - 1) + vf_{il} E_{il} (\lambda_{fail} - 1) \tag{4.4}$$

In this expression, N_f stands for the percentage of fibers bearing load at the instant of failure, vf_{elast} and vf_{il} stand for volume fraction of elastic lamellae and IL space, respectively,

while their elastic moduli are represented by E_{elast} and E_{il}. λ_{fail} denotes the failure stretch of the tissue. We calculated CIRC tissue strength for all the patients in all three cohorts using this expression and performed a correlation analysis against the experimentally measured tissue strength. Specifically, we assessed Pearson correlation (r), Spearmans rank correlation (ρ), and the slope of the regression line (k). We found a very strong correlation between the estimated and corresponding measured strength for CTRL ($r = 0.98$, $\rho = 0.96$, $k = 0.89$) and TAV ($r = 0.86$, $\rho = 0.88$, $k = 0.90$) tissues, while the strength of correlation for BAV cohort was moderately strong ($r = 0.73$, $\rho = 0.71$, $k = 0.75$), see Figure 4.10a-c. The experimental stress-stretch curves for BAV tissues exhibited a wider scatter in the failure stress and stretch, which is the likely cause for weaker correlation. Figure 4.10d plots the same result in the bar chart form, while Figure 4.10e presents the comparison between experimental measurements and analytical estimates of the tissue LONG strength. Again, an excellent agreement between them for all the cohorts can be observed. Taken together, these results suggest that a simple linear rule of mixture based expression can predict the tissue strength reasonably well. All the parameters of the expression are experimentally measurable, except the fraction of the loaded fibers, N_f. We anticipate that there is a correlation between fiber orientation distribution and N_f, which will be the topic of a later report.

We have shown that our computational model is able to accurately recapitulate the tissue uniaxial failure response in two orthogonal directions (LONG and CIRC). Our model shows a pronounced strength anisotropy in the tissue in these directions. While this fact has been observed experimentally (e.g. [75, 66]), the structural model developed in this study provides compelling evidence that organization of the collagen fiber network is a contributing factor in the strength anisotropy. As all the anisotropy in our model is provided by the collagen fiber orientation, the model should also be capable of predicting the tissue failure properties under biaxial loading conditions. Notably, prediction of failure over the entire biaxial loading space allows for creation of a population-relevant failure envelope for the tissue that, in conjunction with patient specific aorta models, could be lead to a metric to evaluate individual dissection risk.

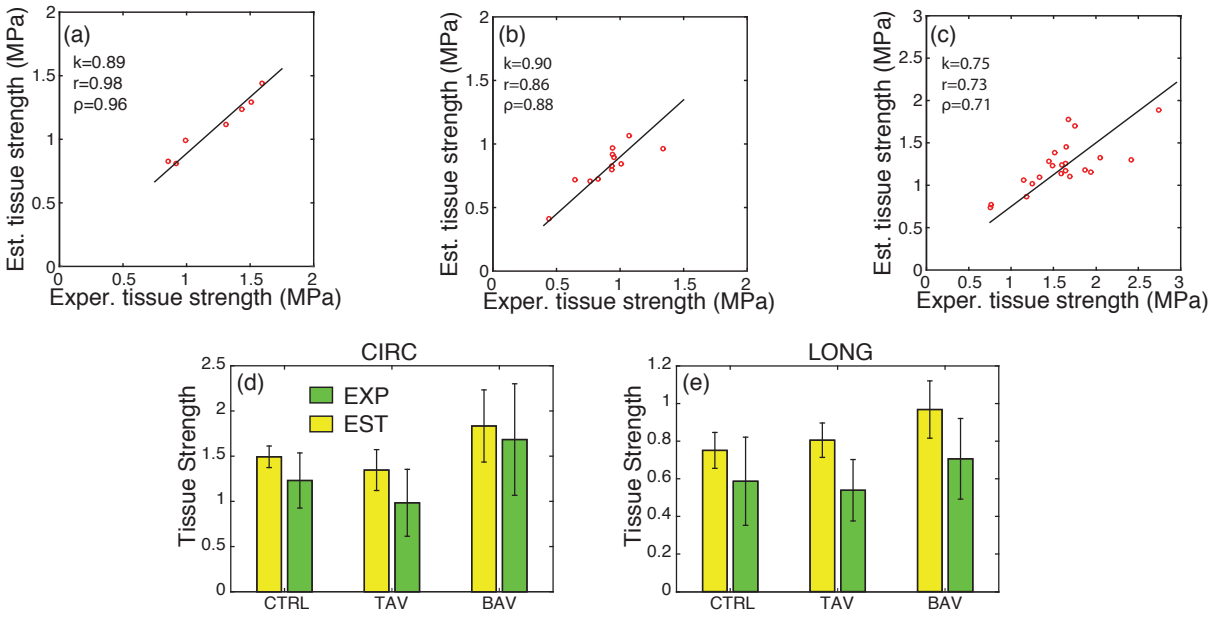

Figure 4.10: Comparison of the experimental tissue strength and analytically estimated tissue strength (Equation 2) for the (a) CTRL, (b) TAV, and (c) BAV populations under CIRC loading. k denotes the slope of a regression line through the origin and r and represent the Pearson correlation and Spearmans rank correlation, respectively. (d) Experimental (yellow) and estimated (blue) tissue strengths in the CIRC direction. (e) Experimental (yellow) and estimated (blue) tissue strengths in the LONG direction. For all cohorts in both the directions, no statistical difference was found between experimental and corresponding analytically estimated tissue strength.

The computational model described in this work has some limitations. We have assumed that the fiber diameter is consistent for the three populations studied. This was based on the published work from our group with aneurysmal tissue (e.g. [2]). The effect of including a distribution of fiber diameters or local variations in fiber diameters within the network or a population-specific fiber diameter could be evaluated in a future study. Further, we have neglected active contraction of the IL due to cell activity. We feel this is a valid assumption as the experimental data used to fit the simulations do not have any active response, but this may change the behavior *in vivo*. Finally, we modeled only the aortic media, while the experimental stress-stretch data were gathered from the specimens of the entire vessel wall. However, Iliopoulos et al. [153] showed that majority of the uniaxial specimens of the ATA wall ruptured from within the media layer. Thus, the failure properties of the entire wall tissue are likely to be limited by the media failure, justifying our choice of the modeling region.

5.0 AORTIC TISSUE STRENGTH UNDER BIAXIAL LOADING

5.1 INTRODUCTION

The previous chapters, Chapters 3 and 4, have developed an RVE of the aortic media which includes microstructural structures of the tissue. Under uniaxial loading, it was shown that the pre-failure and failure properties of the tissue could be accurately captured. However, to accurately assess the risk of aortic dissection, we must have an understanding of the *in vivo* stress state in the aortic wall. Previous work has shown that the stress-state in the aorta is biaxial (e.g. [64, 155]). Thus the failure properties of the tissue *in vivo* may not correspond to those gathered in the previous chapters. What the failure properties of the tissue are between the extremes of uniaxial circumferential (CIRC) and uniaxial longitudinal (LONG) loading are not known. To fill this gap, we have conducted a series of computational experiments simulating the tissue response under the stress ratios expected to be seen *in vivo*.

Experimentally measured uniaxial strength in both circumferential and longitudinal directions have demonstrated highly anisotropic failure behavior of the aortic tissue[75]. Inflation tests, which subject the specimen to equibiaxial loading condition, have revealed that the aortic wall tissue primarily fails in a transverse manner[156]. Mohan and Melvin found physiologic tissue strength of human ascending thoracic aortic tissue under this loading condition to be close to its longitudinal strength[157]. Duprey et al. recently reported physiologic strength of 0.8 MPa under equibiaxial conditions, while the circumferential strength was 1.3 MPa, and longitudinal strength was 0.7 MPa[69]. Both of these works showed that the magnitude of aortic tissue physiologic strength for equibiaxial loading is greater than its uniaxial longitudinal strength, but less than the uniaxial strength in circumferential direction. These studies have contributed to our current understanding of the vessel wall failure

mechanisms. However, although the physiological stress state of the ascending thoracic aortic wall is biaxial in nature, the longitudinal stress component is generally not equal to the circumferential stress.

In this work, we present a computational model of the aortic media capable of estimating physiologic strength of the tissue under biaxial loading conditions. The model was informed by multiphoton image analysis-derived collagen fiber orientation data. As all the model parameters are intrinsic structural properties of the tissue, they were expected to be direction independent. To verify this assertion, model predictions were validated against uniaxial tissue strength for healthy as well as aneurysmal tissues for both circumferential and longitudinal directions. Extensive biaxial simulations were performed on the validated model to determine physiologic tissue strength for a feasible range of the ratio between circumferential and longitudinal loading.

5.2 METHODS

5.2.1 Representative volume element of the aortic media

As with the previous work (Chapters 3, 4), a representative volume element (RVE) is constructed to model the aortic tissue. Specifically, the model represents the medial layer of the aortic wall as that is believed to be the primary region of interest in aortic dissection. Briefly, the RVE is composed of three layers, two elastic lamellae surrounding an interlamellar space. Within the interlamellar space and adjacent to the lamaellae are two discrete collagen fiber networks. Due to the experimentally reported structure of the aortic media, see e.g. Clark and Glagov [158] or O'Connell et al. [44], the media consists of a repeated structure of elastic lamellae separated by an interlamellar space. The elastic lamellae are planar and oriented normal to the radial direction of the aorta. The computational RVE was based upon experimental data gathered by our group and others. For symmetry reasons, the elastic lamellae were taken as 0.75 μm thick, half their physiologic thickness. Total thickness of the RVE was taken as 12.5 μm, with the remainder of the RVE thickness representing the

interlamellar space. Planar collagen networks, adjacent to the lamellae, were composed of discrete collagen fibers (3 μm in diameter) modeled as bar elements. Previously determined network parameters: mean fiber direction (γ), orientation index (OI), and areal density (AD) were used as inputs to a custom Matlab network creation algorithm. The values of these parameters are listed in Table 4.1. Mean fiber direction was taken as $+\gamma$ for one of the two networks in the RVE and $-\gamma$ for the other. Orientation index ($OI \in [0.5, 1.0]$) denotes the degree of alignment of the network, with 0.5 an isotropic network and 1.0 a fully aligned network. The index is calculated by

$$OI = \frac{1}{n}\sum_{i=1}^{n}\cos^2\theta_i \tag{5.1}$$

where n is the number of fibers and θ_i is the angle between fiber i and the mean fiber direction of the network[1]. To construct the networks, fibers were added to the network at a random orientation governed by the OI until the required areal density was reached. At the end of the network creation process, the normalcy of the network was checked using a Lilliefors test ($p \leq 0.05$ denoting a normal distribution). Non-normal distributions resulted in recreation of the network.

To include the effect of the OI distribution, five networks were constructed for each of the cohorts with OI determined by the mean and standard deviation presented in Table 4.1. For this work, two population cohorts were considered: a tricuspid aortic valve non-aneurysmal cohort (control) and tricuspid aortic valve aneurysmal cohort (aneurysmal).

5.2.2 Material model

As with the previous chapter, the RVE is modeled with two constitutive models. The non-collagenous materials (i.e. the lamellae and the interlamellar space) were modeled with an isotropic incompressible neoHookean material represented by the following strain energy function

$$\Psi = \frac{1}{2}\mu(I_1 - 3) \tag{5.2}$$

with $I_1 = \mathrm{tr}\mathbf{C}$ the first invariant of the right Cauchy-Green deformation tensor and μ the shear modulus of the material. The collagen fibers were modeled as discrete 1D rod elements

(see Chapter 2). The fibers were considered as an initially zero stiffness material until the recruitment stretch was reached (representing the initial crimp of the fiber). After that stretch was reached, the stress increased linearly until the fiber strength was reached after which the fiber stress decreased to zero. Specifically this was represented by the following relationship

$$\sigma = \begin{cases} 0 & \text{if } \lambda < \lambda_r \\ E_{col}\,(\lambda - \lambda_r)\,S & \text{if } \lambda > \lambda_r \end{cases} \tag{5.3}$$

with E_{col} representing the collagen fiber stiffness and the λ_r the recruitment stretch. λ is the current stretch of the fiber. To account for damage in the fiber, the parameter $S \in [0.1]$, an internal variable tracking the current fiber damage, was included. The damage parameter remained at its initial value $S = 1$ until the peak stretch of the fiber (λ_p) was reached. After that instant, S monotonically decayed between the fiber stretches of λ_p and λ_{max}, the failure stretch of the fiber. In the event of unloading, S for the fiber remained constant to allow for the fiber to follow the same unloading path upon subsequent loading of the fiber. At and beyond the failure stretch, the fiber was fully failed ($S = 0$) and the thus did not bear further load, even under potential unloading. Evolution of S is based on previously reported work by Maiti and Geubelle[148] and is given by

$$S = \min\left[S_{min}, \langle 1 - \frac{\lambda - \lambda_p}{\lambda_{max} - \lambda_p}\rangle\right] \tag{5.4}$$

where $S_{min} \geq 0$ is the minimum value of S over the course of the simulation. The operator $\langle a \rangle$ is defined as

$$\langle a \rangle = \begin{cases} a & a > 0 \\ 0 & \text{otherwise} \end{cases} \tag{5.5}$$

Failure in the RVE consists only of failure in the collagen fibers. Non-collagenous matrix components remain undamaged over the course of the simulations.

5.2.3 Finite element method

Finite element simulations were performed using a custom non-linear embedded-fiber finite element method [106] in which the collagen fibers are explicitly modeled within the simulation via their endpoints written in terms of the local volumetric element coordinate system (see

Chapter 2 for more details). To simulate the biaxial loading condition on the tissue, the positive CIRC and LONG faces were subjected to an allowed traction incremented by 4kPa per load step, at which rate convergence was seen. The RAD face and the negative CIRC and LONG faces were placed on rollers. Per convergence studies the final RVE consisted of 15,000 8-noded hexahedral elements.

To assess the failure of the tissue under biaxial loading, each RVE was loaded with a number of biaxiality ratios, defined as the ratio of applied LONG to CIRC stress $B = \sigma_{LONG}/\sigma_{CIRC}$, spanning the range of feasible combinations. Biaxial ratios were simulated by adjusting the applied tractions in the CIRC and LONG directions. A maximum applied traction of 2.0 MPa was chosen to ensure failure before the end of simulation (based on experimentally gathered uniaxial strength[75]). The ratios were then simulated by varying the maximum applied reactions in the two principal direction between 0 and 2.0 MPa (Figure 5.1). Tissue failure was defined as the point at which the peak reaction force was reached in either the CIRC or LONG direction. The peak stress does not necessarily correspond to the maximum of the CIRC and LONG stresses, but is the first of those stresses to reach a peak. The first direction to reach a peak stress depends upon the biaxiality ratio, material parameters, and the collagen fiber network. This peak stress was recorded as the physiologic stress under that ratio. At the point of peak stress, the current stress in the other direction was also collected.

A range of potential biaxiality ratios were simulated for each patient population. *In vivo*, the ratio is not expected to exceed 1.0 as the stress in the longitudinal direction is typically less than the stress in the circumferential direction. This follows the computational simulations performed in the next chapter (Chapter 6). However, to account for potential atypical aneurysmal geometries, the biaxiality ratio was varied between 0.0 and 2.0. For each population, 100 simulations were performed with the network chosen at random from the five statistically similar networks created. The biaxiality ratio was also chosen at random within the range specified for each simulation. To elucidate the effect biaxiality ratio on tear direction, an additional set of simulations were performed at $B = \infty$ (uniaxial LONG loading).

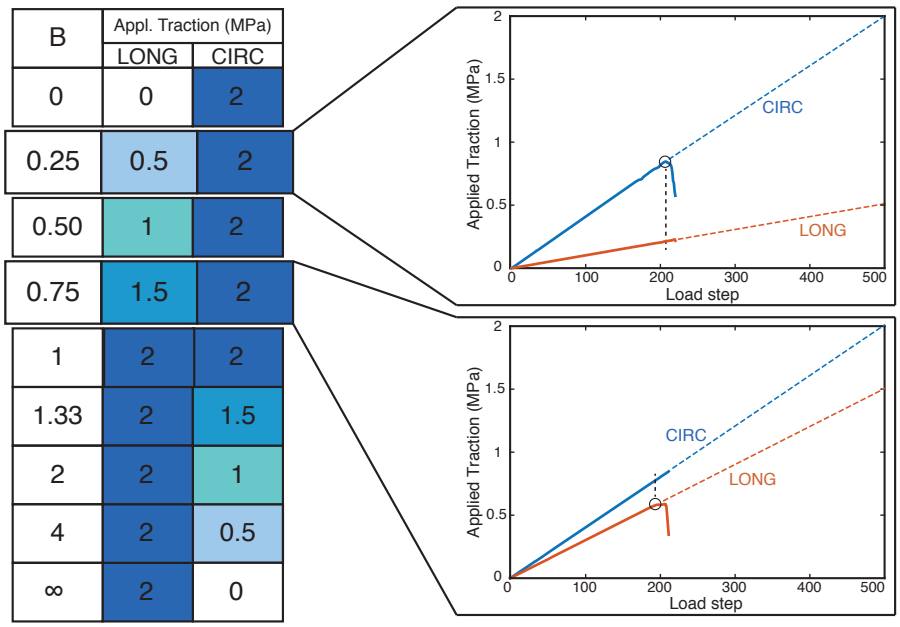

Figure 5.1: Representative biaxial loading ratios (left) and resulting reaction vs. load step (right). Solid lines show the reaction traction while the dashed lines show the projected response if no fiber failure was included. Tissue strength is the traction at which a drop in traction is observed (hollow circle). The strength may be the minimum of the CIRC and LONG tractions depending on the biaxiality ratio and model.

5.2.4 Estimation of model material parameters

The material parameters used for this study were the same as those fitted in the previous chapter. They are listed in Table 4.2. Briefly, the material parameters were determined by individually fitting to patient-specific uniaxial stress-stretch data in the circumferential direction. The average fitted parameters were validated against cohort averaged uniaxial stress-stretch data in the longitudinal direction. No significant difference between the uniaxial experimental data and the simulations in either the CIRC or LONG directions with the control or aneurysmal cohorts.

5.2.5 Statistical testing

All reported values, unless otherwise noted, are given as mean±std. To determine the effect of the CIRC and LONG strengths under different biaxiality ratios on the physiologic strength of the tissue, a backwards stepwise regression (Matlab 2017a, Mathworks, Natick, MA) was used. Variables (CIRC and LONG strengths)were removed from the model if the associated p-value was greater than 0.10.

To determine the transition biaxiality ratio between the high strength and low strength regions of the response, a nonlinear least-square fitting algorithm in Matlab was used. The objective function was defined as the Heaviside function

$$H(x) = \begin{cases} 0 & \text{when } x < a \\ 0.5 & \text{when } x = a \\ 1 & \text{when } x > a \end{cases} \tag{5.6}$$

where a is the transition point from CIRC to LONG failure. All simulations with LONG failure were denoted by 0 and CIRC failure as 1 when conducting the fit. Similar methods for determining the transition point in a dataset have been reported in the literature[159, 160].

5.3 RESULTS

5.3.1 Physiologic tissue strength under biaxial loading

The statistically similar RVEs of the aortic media tissue were subjected to a biaxial loading state using biaxiality ratios between 0 and ∞, with a ratio of 0 corresponding to uniaxial circumferential loading and ∞ to uniaxial longitudinal loading. For each simulation, the physiologic strength (that is the limiting strength of the tissue) as well as the direction of failure (the direction in which the peak stress was reached first) was recorded. The tissue strength in the CIRC and LONG directions are shown in Table 5.1. The physiologic strength is reported for all cases in which the failure was controlled by either the CIRC or LONG direction. The same data is represented graphically in Figure 5.2. We separate the physiologic strength in the simulations for each cohort into two groups each. There was a distinct difference in physiologic strength based on the direction of failure. Those biaxiality ratios that failed in the CIRC direction (below B_{trans} in the figure) had physiologic strengths which were similar to the experimentally gathered CIRC strength while the physiologic strengths with biaxiality ratios above B_{trans} were similar to the experimentally gathered LONG strengths. There were no significant differences between the experimental CIRC strength and the physiologic strength for $B < B_{trans}$ for either the control of aneurysmal cohorts. Nor were there no significant difference between the experimental LONG strength and the physiologic strength for $B > B_{trans}$ for either the control of aneurysmal cohorts. There was a significant difference between the physiologic strengths above and below the transition point.

A plot of the physiologic strength with respect to the biaxiality ratio (Figure 5.3) shows the sharp change in strength at the transition point B_{trans}. The material parameters for the simulations were taken from the LHS design. A transition point was found at $B_{trans} = 0.68$ for control and $B_{trans} = 0.69$ for aneurysmal tissue. This corresponds to failure in the CIRC (for $B < B_{trans}$) and LONG (for $B > B_{trans}$) direction as defined by the first direction to see a drop in the reaction traction. There was a small increase in the physiologic strength from uniaxial CIRC load-state (at $B = 0$) until the transition ratio for both cohorts. There was

Table 5.1: Physiologic tissue strength for CIRC and LONG dominated failure compared with experimental uniaxial CIRC and LONG strengths as reported in Pichamuthu et al.[75]. There is no significant difference between the simulated physiologic and uniaxial strengths ($p < 0.05$ for all cases)

Cohort	S_{CIRC} (MPa)		S_{LONG} (MPa)	
	Simulation	Experiment	Simulation	Experiment
Control	1.12 ± 0.05	1.24 ± 0.29	0.50 ± 0.04	0.59 ± 0.23
Aneurysmal	1.03 ± 0.03	0.97 ± 0.38	0.54 ± 0.14	0.54 ± 0.16

not significant change in physiologic strength above B_{trans} for either cohort. The strength as measured by uniaxial tensile experiments is shown for comparison.

5.3.2 Failure pattern of fibers under biaxial loading

The failure pattern in the collagen fiber network differs significantly depending on the biaxiality ratio. For aneurysmal tissue, a ratio below $B_{trans} = 0.69$ will result in failure predominantly in the CIRC direction (Figure 5.4). A ratio greater than this however shifts the predominant failure direction to the LONG direction. There is a significant degree of scatter at the transition point, with small difference in biaxiality ratio yielding large difference in strength depending on the RVE. With a biaxiality ratio of 0.25, 98% of the failed fibers were within 30 degrees of the CIRC direction. However under equibiaxial loading ($B = 1.0$), 75% of the failed fibers were within 30 degrees of the LONG direction. Between a ratio of $B = 0.50$ and $B = 0.75$, there was a transition region. 90% of the failed fibers were within 30 degrees of the CIRC direction at $B = 0.50$ dropping to only 65% within 30 degrees of the CIRC direction at $B = 0.75$. Under the highest ratio described in the figure, $B = 1.0$, less than 1% of the failed fibers were within 30 degrees of the CIRC direction. These results are not limited to aneurysmal tissue, similar trends were observed in control tissue (Figure 5.5)

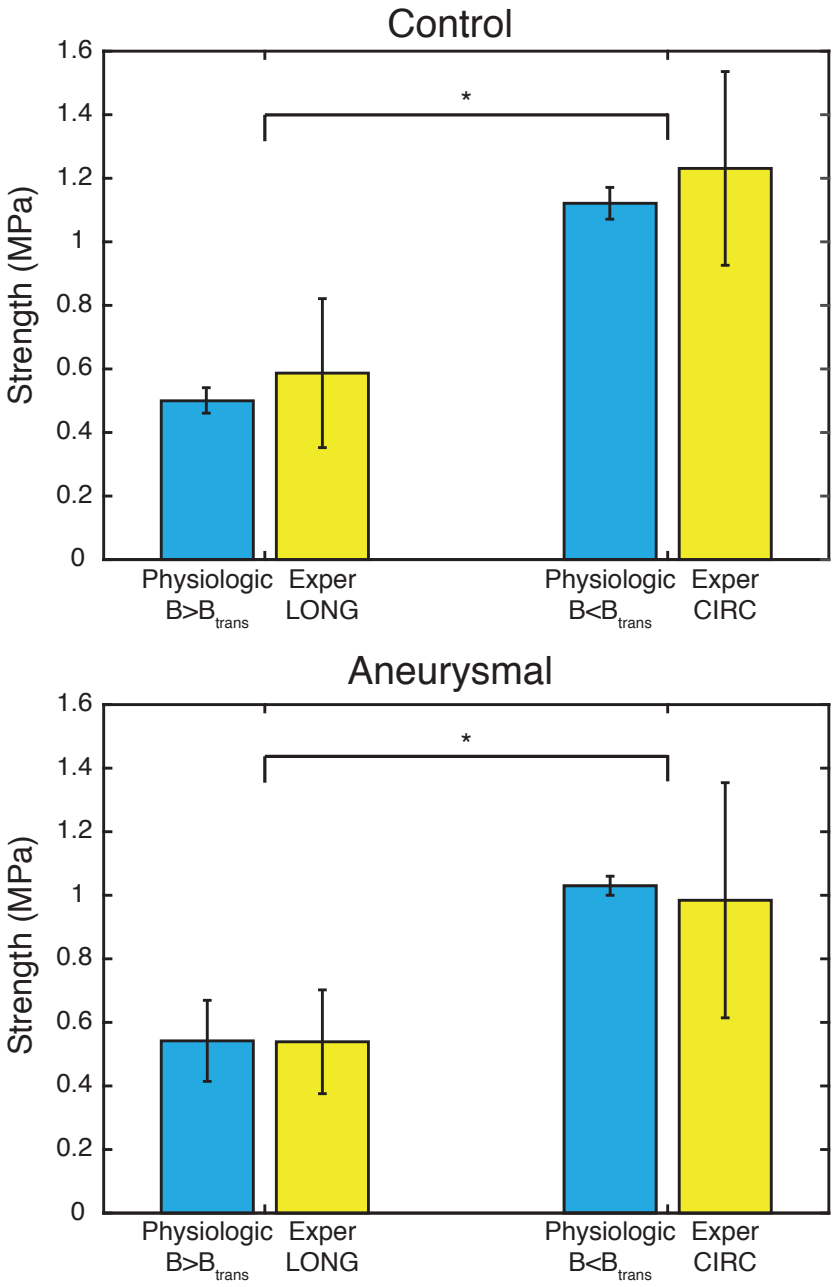

Figure 5.2: Physiologic strength and experimentally gathered uniaxial strength for aneurysmal and control tissue. There is no significant difference between the physiologic strength below the transition point and the experimental CIRC strength in either group ($p > 0.05$, t-test) nor a difference between the physiologic strength above the transition point and the experimental LONG strength. There is a significant difference between the physiologic strength above and below the transition point ($p < 0.005$, t-test). $*$ Denotes statistical significance.

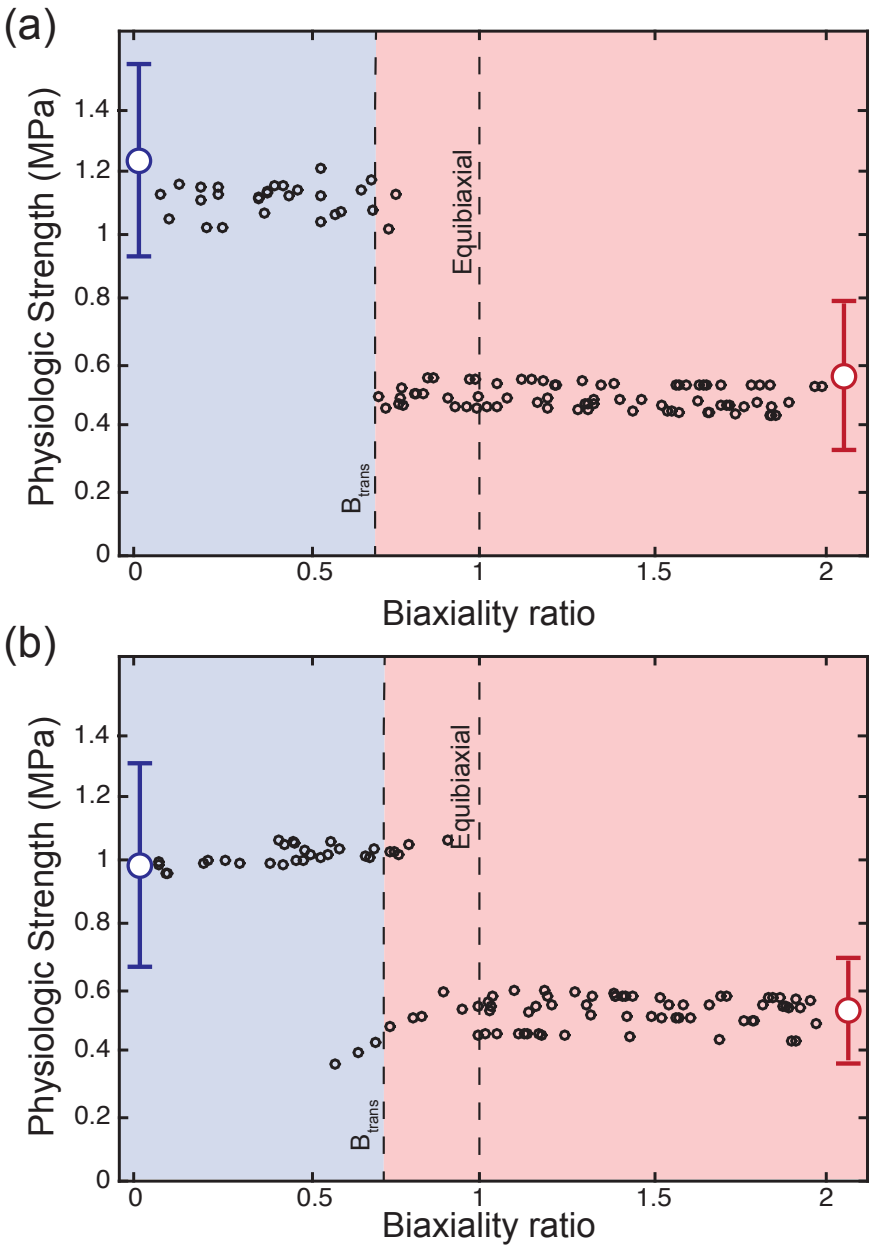

Figure 5.3: Physiologic strength with respect to the applied biaxiality ratio B for the control (a) and aneurysmal (b) cohorts. There is a sharp transition in physiologic strength at the transition point (B_{trans}). The biaxiality ratio for an equibiaxial load as well as the transition ratio are shown with dashed lines. Uniaxial experimental strengths are shown with large circles. The red is the uniaxial LONG strength and the blue the uniaxial CIRC strength.

with fiber failure with low biaxiality ratios primarily in the CIRC direction but transitioning to LONG oriented failure under high biaxiality ratios.

To further quantify the transition from CIRC to LONG oriented failure, the tear direction was computed for the biaxiality ratios defined in Figure 5.1. For each simulation, the tear direction was found by computing the average direction orthogonal to all failed fibers at the time of peak reaction traction (Figure 5.6). Fiber failure in the CIRC direction (at 0 degrees) corresponds to a tear aligned with the LONG direction (90 degrees). Under the extreme biaxiality ratios, there was low variability in the tear direction, with low B resulting in tears oriented in the LONG direction and high B resulting in CIRC oriented tears. As suggested in Figures 5.4 and 5.5, moderate B resulted in a tear direction between those extremes. Further, in the transition region, there was significantly higher variability in the tear direction, with a ratio of 0.75 having a standard deviation of approximately 20 degrees for both the control and aneurysmal tissues.

5.4 DISCUSSION

Better understanding of the failure process is crucial in understanding the aortic dissection process. To date, the majority of the published literature reports failure properties under only uniaxial loading. The stress-state *in vivo* however is multiaxial, potentially limiting the utility of these data. Development of more advanced dissection risk assessments are hampered by the lack of experimental data under physiologically relevant loading. Some exceptions are the work of Mohan and Melvin[157] and Duprey et al.[69]. These groups load thoracic aorta tissue under an equibiaxial loading condition. To our knowledge however, there are no published data exploring the failure properties of the thoracic aorta under other biaxial loading states.

Figure 5.2 shows that the RVE constructed in this chapter is able to accurately capture the response of the tissue for both the control and aneurysmal cohorts when compared to experimental uniaxial test data. As mentioned in the previous chapters, the model is able to match the data with a small number of material parameters, collagen network areal density,

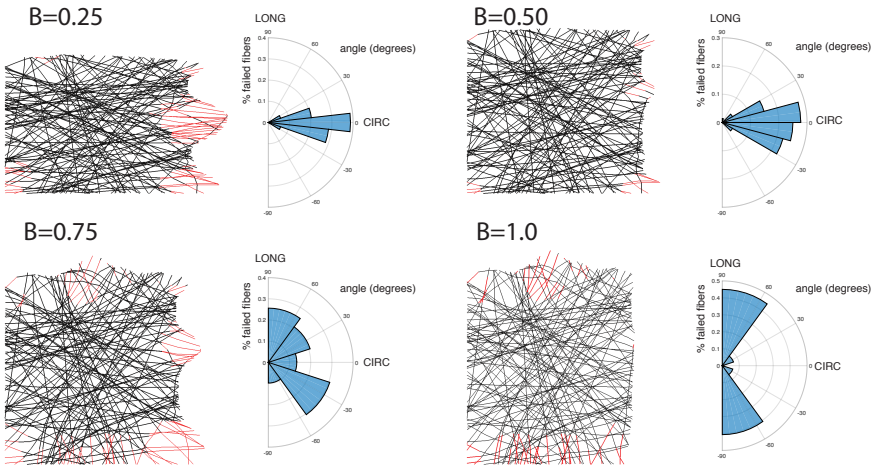

Figure 5.4: Failure pattern in aneurysmal tissue under various biaxiality loading ratios. Ratios below 0.69 (top row) show failure predominantly in the circumferentially aligned fibers. Above this ratio however, there are a significant number of longitudinally aligned fiber failures (bottom row). The polar plots show the percentage of failed fibers plotted against the fiber angle at the time that the failure pattern was visualized. Zero degrees corresponds to the CIRC direction and 90 degrees to the LONG direction. As shown by the polar plots, the direction of failure shifts from the CIRC direction to the LONG direction with a ratio above 0.69.

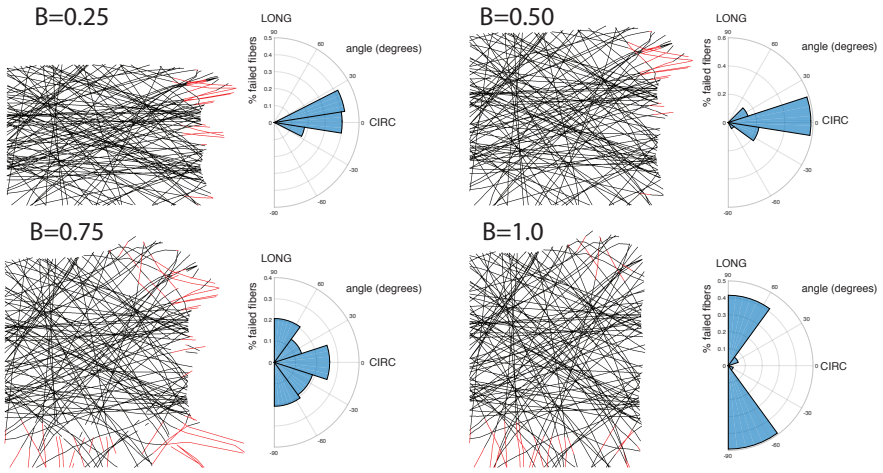

Figure 5.5: Failure pattern in control tissue under various biaxiality loading ratios. Ratios below 0.68 (top row) show failure predominantly in the circumferentially aligned fibers. Above this ratio however, there are a significant number of longitudinally aligned fiber failures (bottom row). The polar plots show the percentage of failed fibers plotted against the fiber angle at the time that the failure pattern was visualized. Zero degrees corresponds to the CIRC direction and 90 degrees to the LONG direction. As shown by the polar plots, the direction of failure shifts from the CIRC direction to the LONG direction with a ratio above 0.68.

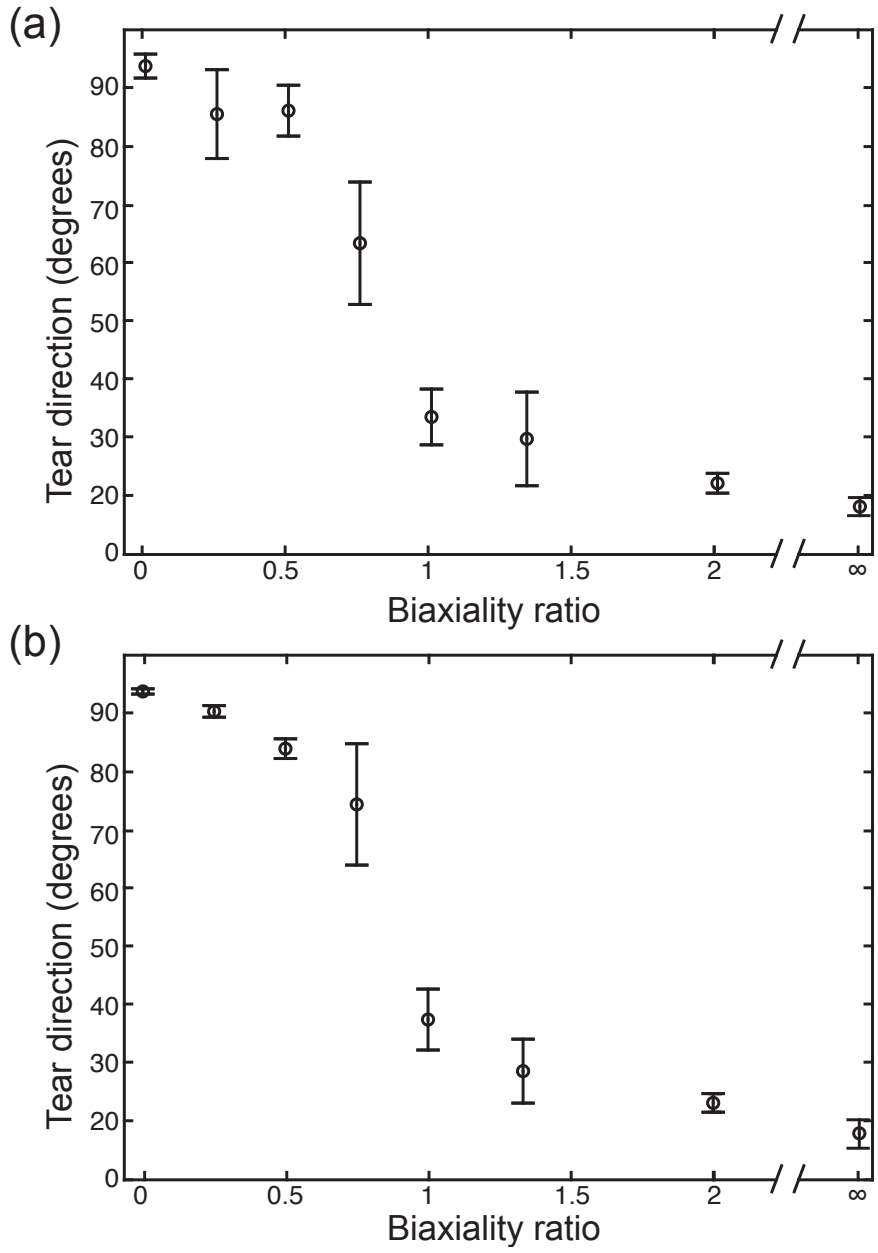

Figure 5.6: Mean tear direction with respect to biaxiality ratio for control (a) and aneurysmal (b) tissue. 0 degrees denotes the CIRC direction and 90 degrees the LONG direction.

orientation index, and mean fiber direction as well as the elastin shear modulus, and collagen stiffness, collagen strength, and collagen recruitment stretch. All of the network parameters can be gathered from microscopy imaging of the tissue (areal density, orientation index, and mean fiber direction) while the fitted parameters fell within reported values from the literature. As with the literature (e.g. Pichamuthu et al.[75]), we saw a significant difference between the strength when the RVE was loaded in the CIRC versus the LONG direction. Further, we found that the transition between the high strength CIRC dominated failure and low strength LONG dominated failure occurred sharply (Figure 5.3). There was a noticeable difference in the transition point for the cohorts, with the control tissues transitioning at a biaxiality ratio of 0.68 versus 0.69 for the aneurysmal tissues. The dashed line in the figure denoting the equibiaxial stress-state suggests that failure under that loading condition is likely to be controlled by the LONG strength of the tissue. The available experimental data[157, 69] show a similar result with the strength under that loading condition similar to the LONG strength. Further, the experimental equibiaxial loading testing showed a tear direction in the transverse direction. This tear direction matches with what was seen with our experiments (Figure 5.6). Based on the fit to the uniaxial experimental strength and the qualitatively similar response to equibiaxial loading, this suggests that our model is able to accurately capture the tissue response under the gamut of potential *in vivo* loading scenarios.

Figure 5.6 shows that both control and aneurysmal tissue is susceptible to transverse tears under high biaxiality ratios. This failure occurs at approximately the LONG strength of the tissue. This may be applicable to dissection in the aorta as the biaxiality ratio will increase in more aneurysmal aortas. The aorta may be considered, at a basic level, as a thin walled pressure vessel. By doing so, we can use theoretical solutions for the stresses in these geometries. Laplaces law states that the hoop stress (e.g. the stress in the CIRC direction) is

$$\sigma_{CIRC} = \frac{Pr}{t} \tag{5.7}$$

with P, r, and t the applied pressure, vessel radius, and wall thickness, respectively. In the LONG direction, the stress becomes

$$\sigma_{CIRC} = \frac{Pr}{2t} \tag{5.8}$$

half the stress in the CIRC direction. These values of course assume that the vessel is a perfect cylinder. Change in the geometry will affect these values. Indeed, the stress in both directions will be $\sigma = Pr/t$ for a sphere (that is, the stresses will be the same when there is no difference in local curvature). Due to the anisotropic nature of aortic tissue, this suggests that regions on the aortic wall with a high biaxiality ratio may be more prone to dissection. For vessels, burst tests have observed dissection in the transverse direction[156], with our data suggesting that this trend will be more pronounced as the vessel becomes increasingly aneurysmal. The factors controlling dissection are thus likely to be not only the tissue strength, but also the shape of the aorta. Further, the limiting strength is likely to be the LONG strength. We have shown (Chapter 4) that elastin properties have a significant impact on strength in the LONG direction which suggests that elastin fragmentation may also be a critical factor in dissection risk. Elastin fragmentation is observed with ageing[161] and aneurysm[5] and may play a significant biomechanical role in aortic dissection.

This study has two main limitations. As with our previous studies, Chapters 3 and 4, we have considered only the aortic media. While the aortic wall is composed on three layers, dissection occurs within the media[153] thus suggesting that the wall failure is likely limited by failure within this layer justifying our choice. Secondly, while failure properties of the aorta are readily available under uniaxial loading, there are few papers in the literature discussing strength under biaxial loading. With the exception of the equibiaxial experiments noted above, there are no data on biaxial failure properties. As such, validation of our model under other loading conditions is limited. However, we feel that the agreement with the uniaxial and equibiaxial data that is available suggest that the model is valid for the biaxial loading conditions seen *in vivo*.

5.5 CONCLUSIONS

This Chapter has developed a thoracic aorta RVE that can accurately capture experimental stress-stretch data. Using this model, we have predicted the physiologic strength of both control and aneurysmal tissues under a wide variety of loading conditions expected to be

seen *in vivo*. We have shown a sharp transition from CIRC dominated to LONG dominated failure which suggests that the local biaxiality ratio must be considered in the prediction of aortic dissection. Due to the relatively low strength in the LONG direction, strength in an aorta is likely limited by that strength. This is predicted to be exacerbated by aneurysmal aortas as the percentage of the aorta with biaxiality ratios above the threshold will increase.

6.0 DEVELOPMENT OF A METRIC FOR AORTIC DISSECTION RISK

6.1 INTRODUCTION

The previous chapters have developed a microscale model of the aortic wall tissue. To construct a more accurate metric for use in predicting the risk of aortic dissection however, the entire aorta, both at the microscale and at the whole organ level must be considered. Specifically, we propose a stress-based dissection potential index to evaluate the risk of dissection. The proposal of mechanistically based metrics for assessing risk is not new, both Martin et al[67] and Duprey et al.[69] for example has suggested stretch-based criteria for prediction of ascending thoracic aorta dissection. However, these stretch-based metrics may be insufficient as aortic geometry and *in vivo* stress-state were not considered in their construction. The use of the *in vivo* stresses state to assess risk is not uncommon in the literature, significant work has been done to predict rupture potential for Abdominal Aortic Aneurysms (AAA), see e.g. [162, 163].

Hampering the development of a stress-based dissection risk metric for the ascending thoracic aorta is the scarcity of knowledge on physiologic failure properties of the aortic tissue. While the failure properties of thoracic aortic tissue under uniaxial loading have been reported in the literature, [153, 75, 133, 142], relatively little attention has been paid to the biaxial failure properties of the tissue. Exceptions are the equibiaxial experiments by Mohan and Melvin[157] and Duprey et al.[69]. However, no data, to our knowledge, exists on the failure response of aortic tissue under other multiaxial loading conditions.

We note that although the dissection process is a multifactorial problem, the dissection event itself due to mechanical effects. Failure mechanics states that the tissue will fail when the local stress in the body exceeds the local strength. Determining this state is complicated

in the aorta due to (as stated above) the relatively small amount of data on the multiaxial failure properties of aortic tissue. However, the results from Chapter 5 suggest that there is a clear differentiation between circumferentially (CIRC) dominated and longitudinally (LONG) dominated failure modes. By considering the *in vivo* stress-state in the aorta in terms of the CIRC and LONG coordinate system we can predict the physiologic failure response of the aorta at all points in the aorta. Further, failure mechanics suggests that LONG dominated dissection is the limiting value in aortic tissue due to the relatively low LONG strength vs. CIRC strength. We propose a dissection potential index based on the LONG stress and strength of the tissue and compare it against clinically observed failure location. This criterion may be the basis of a future non-invasive metric for identification of patients at high risk of type A aortic dissection.

The work in this chapter is possible due to the effort provided by Leonid Emerel. He was instrumental in identification of the patients in the control and dissection cohorts as well as help with statistical testing of the data.

6.2 METHODS

6.2.1 Patient selection

All patients undergoing type A aortic dissection (TAAD) repair by Dr. Gleason between 2007 and 2016 were retroactively identified. IRB approval and patient consent was obtained for all patients. Of the total number of patients presenting with acute TAAD (n=351), a cohort was selected for those with available computed tomography angiography (CTA) at time of dissection and at least 1 CTA pre-dissection (n=15). Patients experiencing TAAD within one year of a surgical procedure requiring manipulation of the ascending aorta (including coronary bypass grafting with proximal aortic anastomosis, aortic valve replacement, or placement of a ventricular assist device) were excluded from the study (n=11). Subsequent data analysis excluded TAAD patients with retrograde propagation after thoracic aortic endovascular stenting bringing the final cohort to (n=7) patients. A control cohort (n=7)

Table 6.1: Patient statistics for the control and dissection cohorts. (p-values calculated with Mann-Whitney U test, ns denotes no significant difference)

	TAAD (n=7)	Control (n=7)	p-value
Age (years)	62.25 ± 3.46	62.5 ± 3.15	ns
Gender (% males)	77	77	ns
Height (cm)	175.73 ± 2.98	171.25 ± 3.15	ns
Weight (kg)	88.61 ± 6.78	88.78 ± 8.75	ns
BMI (kg/m^2)	28.69 ± 2.10	30.07 ± 2.53	ns
Max orthogonal diameter (mm)	47.78 ± 2.75	31.50 ± 1.56	$p < 0.01$
Systolic blood pressure (mmHg)	129 ± 7	127 ± 7	ns
Diastolic blood pressure (mmHg)	73 ± 5	73 ± 4	ns

was selected from the patient bank with tricuspid aortic valve (TAV), no connective disorder, and no prior history of cardiac surgery. The control cohort was age, body mass index (BMI), and blood pressure matched to the dissected cohort. Statistics of the patients (mean±std) are given in Table 6.1.

6.2.2 Model creation

Contrast CTA image data were collected from patients during the normal course of clinical observation. Before scanning, 150 mL of standard nonionic contrast were administered at 4 mL/s. CTA images were obtained during a single sustained breath held by the patient to reduce artifacts from respiratory-induced motion. Individual images were generated at 2-3 mm slice spacing along the thoracic aorta. The CTA data were imported into Mimics (Materialize, Leuven, Belgium) and a surface reconstruction extending from the sino-tubular junction and extending 10-15 cm distal to the aortic arch extracted. The surface point cloud was imported into Geomagic (3D Systems, Rock Hill, SC) for cleanup and surface construction.

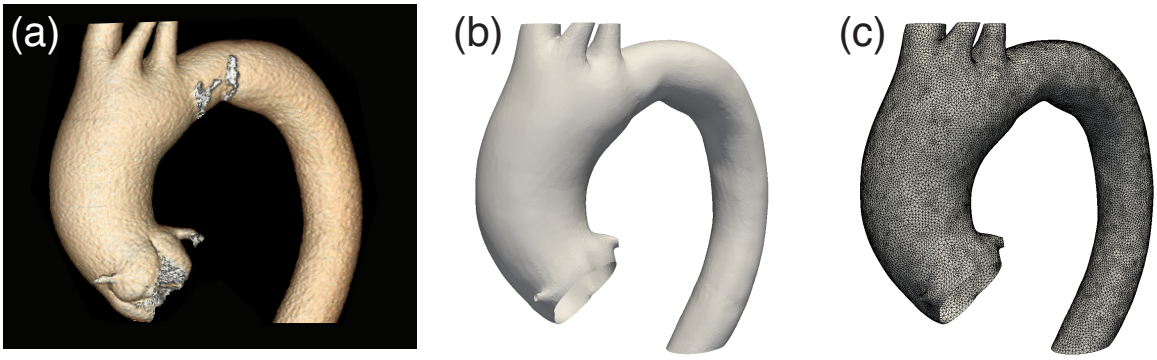

Figure 6.1: To create the aortic models, CTA scans (a) were reconstructed and smoothed (b). The smoothed model was then discretized with triangular elements (c).

The final finite element discretization was performed in Trelis (csimsoft, American Fork, UT). Meshes consisted of 30,000-50,000 3-noded triangular elements oriented in 3D space. All models were fixed against deformation at model boundaries and an internal pressure of 200 mmHg was applied to the domain. The process is described in Figure 6.1.

6.2.3 Finite element analysis

The finite element simulations were performed using a custom nonlinear dynamic membrane program. The dynamic time-stepping algorithm is provided in [164] while the membrane formulation is based upon that given in Taylor et al.[165]. The domains were pressurized at a minimum of 0.01 mmHg/step. Convergence was ensured by decreasing the loading rate if the change in maximum stress exceeded 5% under a 2x increase in load steps.

The material model for the aortas was a 2-parameter hyperelastic incompressible isotropic model developed by Raghavan and Vorp[57] for abdominal aortic aneurysm tissue. The strain energy function for the material is given by

$$\Psi = \alpha(I_1 - 3) + \beta(I_1 - 3)^2 \tag{6.1}$$

Table 6.2: Average Ragahavan-Vorp material model parameters for the aorta simulations

Cohort	α (kPa)	β (kPa)
Control	0.74 ± 0.5	34.0 ± 1.5
Dissected	49.3 ± 13.3	72.7 ± 19.7

where $I_1 = \text{tr}\mathbf{C}$ is the first invariant of the right Cauchy-Green deformation tensor and α and β are material parameters. Material parameters were determined by using patient-specific aortic strains determined from two-dimensional transthoracic echocardiography taken pre-dissection. A parasternal long axis window was used to record the aortic diameter at diastole and systole. Diameters were collected 3 cm above the aortic valve with the diameter at diastole (AoD) obtained at the peak of the R wave in a simultaneously recorded electrocardiogram and the diameter at systole (AoS) obtained at the initiation of the T wave. Multiple measures were taken over the course of the electrocardiogram and the mean values calculated. The aortic strain over the cardiac cycle ($\varepsilon = (AoS - AoD)/AoD$) was then found for each patient. To determine the patient-specific aortic stiffness, the models were simulated to the diastolic blood pressure. Mean diameters were found at three locations on the aortic wall at systolic and diastolic blood pressure and the aortic strain between those pressures recorded. The material properties were iterated until the difference between the clinically recorded and simulated strains over the aortic cycle was less than 5%. Mean fitted values of the material parameters for the control and dissected cohorts are given in Table 6.2. Model visualization was performed with Paraview (Kitware Inc, Clifton Park, NY). To determine statistical difference between groups, a two-sample t-test was used (Matlab).

6.2.4 Construction of a dissection potential index

Based on our previous work with biaxial loading of a computational model of the ascending thoracic aortic media tissue (Chapter 5), the longitudinal direction was identified as the

likely limiting factor in aortic dissection. We propose a simple safety factor based dissection potential index (DPI)

$$DPI = \frac{\sigma_{LONG}}{S_{LONG}} \tag{6.2}$$

where the index is defined in terms of the tissue stress (σ_{LONG}) and strength (S_{LONG}) in the longitudinal direction. The DPI is in the range $DPI \in [0, 1]$ with an index greater than 1, that is if the stress exceeds the strength, denoting aortic dissection (tissue failure). From this equation, a higher DPI suggests a higher potential for dissection. Values for the stress will be provided by the stress analysis of the aorta while the strength is estimated in a patient-specific manner based on uniaxial stress-stretch experiments in either the CIRC or LONG directions (segregated by the transition biaxiality ratio determined in Chapter 5). As noted in that chapter, the biaxial strength can be determined by the uniaxial strength as well as the ratio of the biaxial stresses. The process for construction of the DPI is shown in Figure 6.2.

6.2.5 Validation of DPI against clinically observed dissection locations

Perioperative scans of the dissected patients were used to determine initiation sites of the dissection. To visualize these locations, a senior board-certified aortic surgeon with extensive experience in evaluation of imaging to diagnose dissection (Dr. Gleason) selected the dissection location on patient-specific 3D surface models of the aortas. The surgeon was blinded to the computational stress analyses prior to location identification.

After the dissection locations were identified, the results were superimposed on the stress contours to compare overlap between regions of high stress.

6.3 RESULTS

6.3.1 Stress and DPI in the aorta

The simulations show CIRC stress concentrations on the lesser curvature of the aortas for both the control and dissected cohorts. Similarly, both cohorts show LONG stress concen-

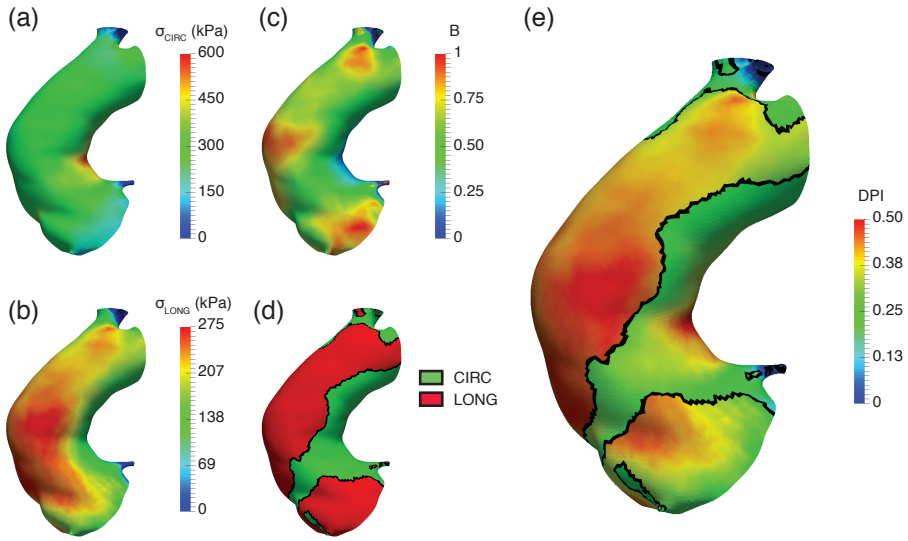

Figure 6.2: Construction of the DPI. The CIRC (a) and LONG (b) stress contours were used to calculate the stress biaxiality ratio $B = \sigma_{LONG}/\sigma_{CIRC}$ (c). A transition B of 0.59 and 0.69 was used for the control and dissection cohorts, respectively. Below the transition ratio, the aorta wall is controlled by CIRC stress, and above it is controlled by LONG stress (d). The DPI for the aorta segregated by B.

trations on the greater curvature of the aorta. All of the dissected cohort have a stress concentration near the sino-tubular junction with a subset (2 of 7) having elevated LONG stress along the length of the ascending thoracic aorta on the greater curvature. There is elevated DPI on the greater curvature of the aorta for the dissection set (Figure 6.3).

6.3.2 Dissection potential index increases in dissected cohort

With respect to the control cohort, there is significantly elevated LONG stress in the ascending thoracic aorta of dissected cohort (Figure 6.4, $p < 0.001$). Further, there was a significant difference between the stress in the CIRC and LONG directions for both the control and dissection cohorts ($p < 0.001$). There was so significant difference between the CIRC stress in the control and dissection cohorts ($p = 0.2$).

DPI is significantly higher in the dissected cohort than in the control cohort (Figure 6.5, $p = 0.03$, t-test). DPI for the control and dissected cohorts were 0.32 ± 0.07 and 0.49 ± 0.04, respectively. The figure shows the peak DPI in the ascending portion of the thoracic aorta in both cohorts, with the DPI for the dissected taken from the last CTA geometry pre-dissection.

Representative plots of DPI are shown in Figure 6.6. The DPI for the dissected cohort is elevated in the LONG controlled regions of the aortic wall while the DPI is similar about the entire circumference of the aorta in the control cohort. For all aortas shown in the figure, the CIRC strength controlled region contains the lesser curvature of the aorta while the LONG strength controlled region contains the greater curvature of the aorta.

6.3.3 Dissection potential index increases over time

All patients in the dissected cohort included at least one pre-dissection scan. Plotting the DPI with respect to the time from the scan to the dissection event (Figure 6.7) shows that there was a noticeable increase in the dissection potential index over time. For all patients shown in the figure, there is an increase in the DPI from the first scan to the time of dissection.

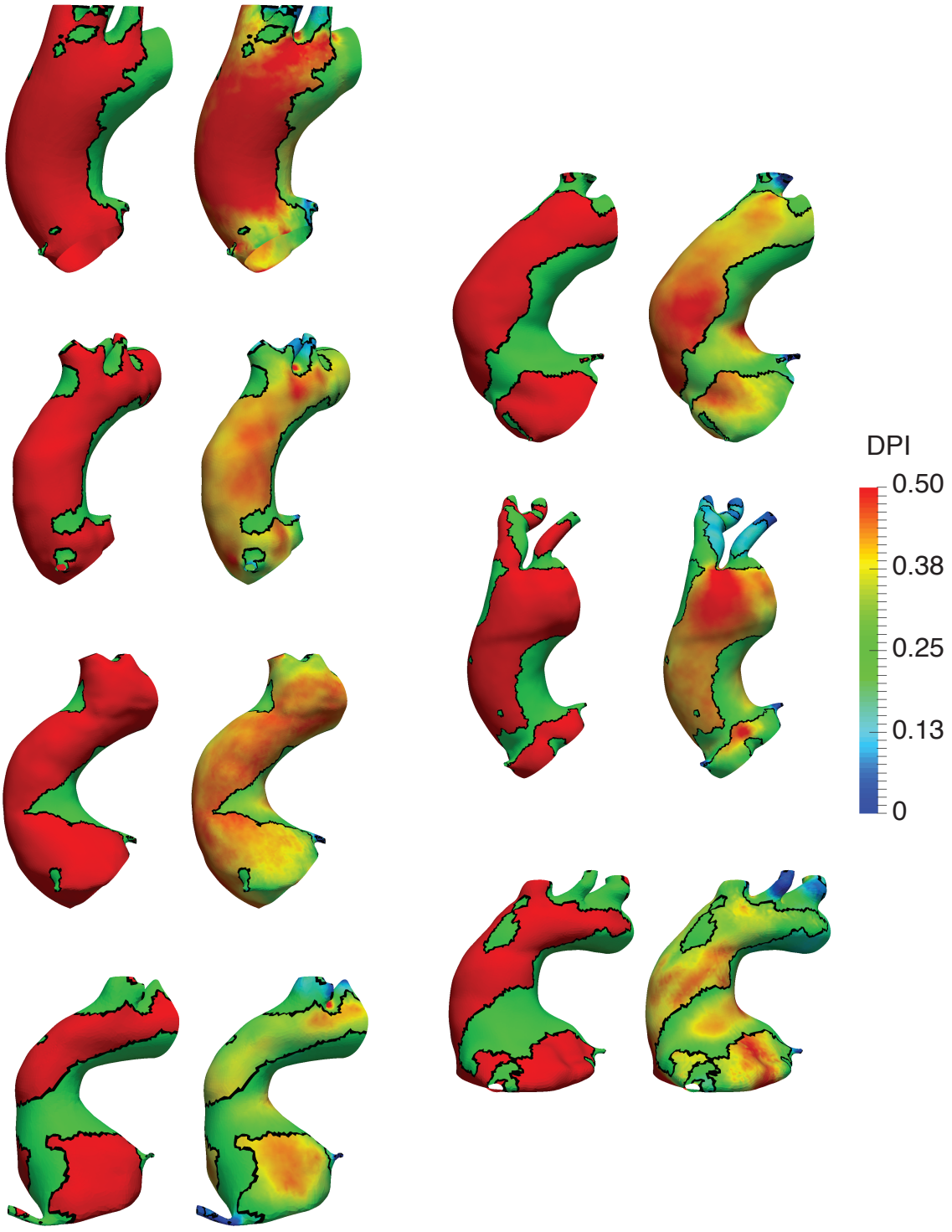

Figure 6.3: DPI in the dissection cohort. The descending thoracic aorta has been suppressed for clarity. The solid red region denotes LONG controlled dissection and the solid green region CIRC controlled dissection.

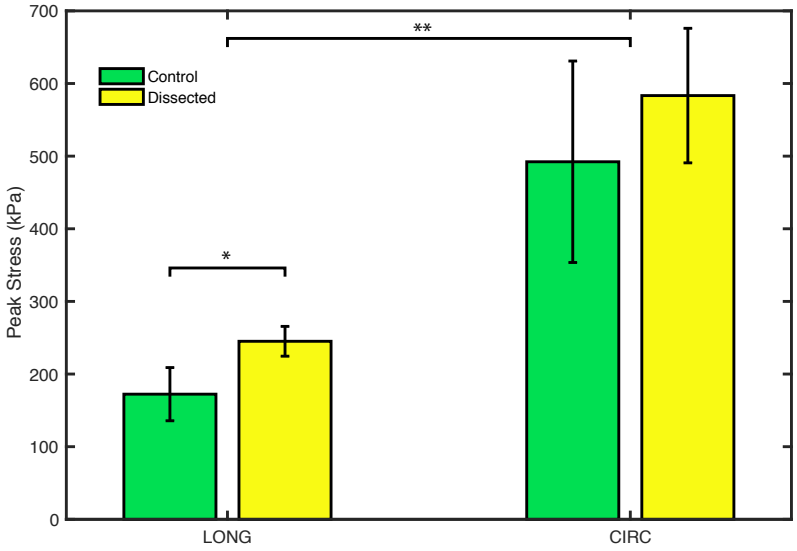

Figure 6.4: Peak stress in the control and dissection cohorts. $*$ denotes a significant difference between LONG stress between the control and dissection cohorts. $**$ denotes significant difference between the peak CIRC and LONG stresses for both the control and dissection cohorts.

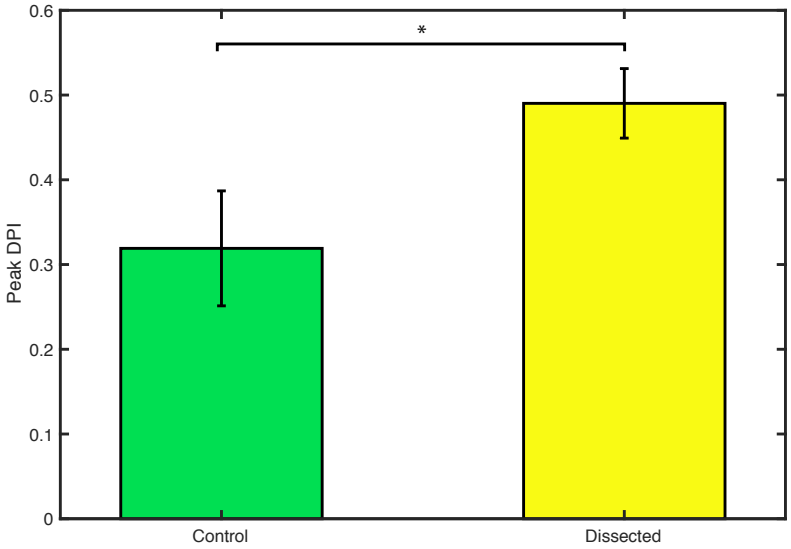

Figure 6.5: DPI for the control and dissection cohorts. $*$ denotes a significant difference between the DPI for the control and dissection cohorts.

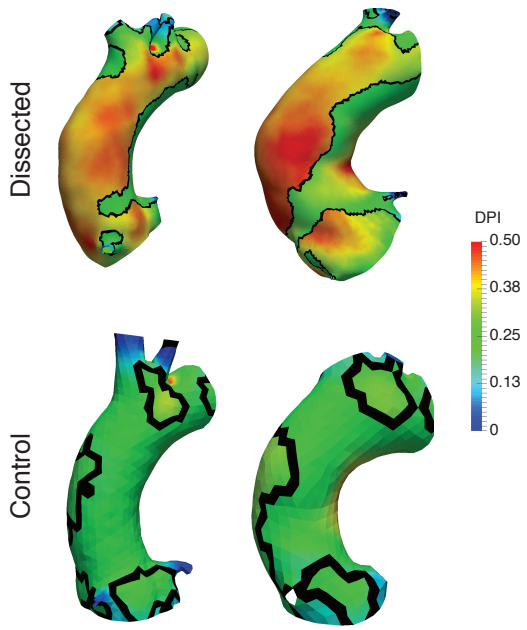

Figure 6.6: Representative DPI in control and dissection cohorts

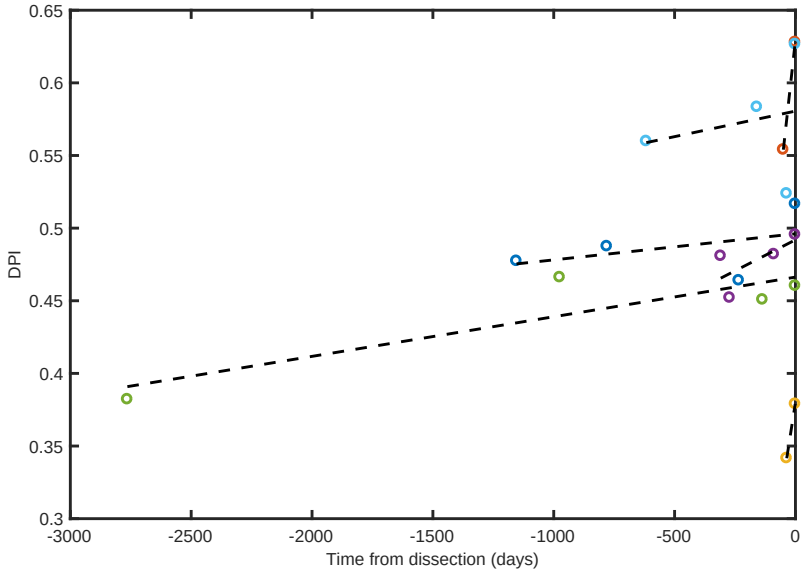

Figure 6.7: Increase in DPI over time for patients in the dissected cohort

6.3.4 Increase of DPI with aortic diameter

Figure 6.8 shows the DPI plotted against the maximum orthogonal diameter of the aorta for both cohorts. There is a strong correlation between the diameter and DPI for the control patients, with an increase in diameter leading to an increase in the DPI. There is low correlation between the diameter and DPI in the dissection cohort. An increase in the diameter causes low increase in the DPI.

6.3.5 Validation of the dissection potential index

To validate our choice of dissection potential index, that the dissection event is limited by the longitudinal stress and strength, we compared the clinically observed dissection location against the LONG and CIRC stress contours. Figure 6.9 shows the dissected aortas and the associated circumferential stress contours. The grey region is the clinically observed dissection initiation site. As noted in Section 6.3.1, the circumferential stress is elevated on the lesser curvature of the aorta. The dissection location of the aorta however was situated

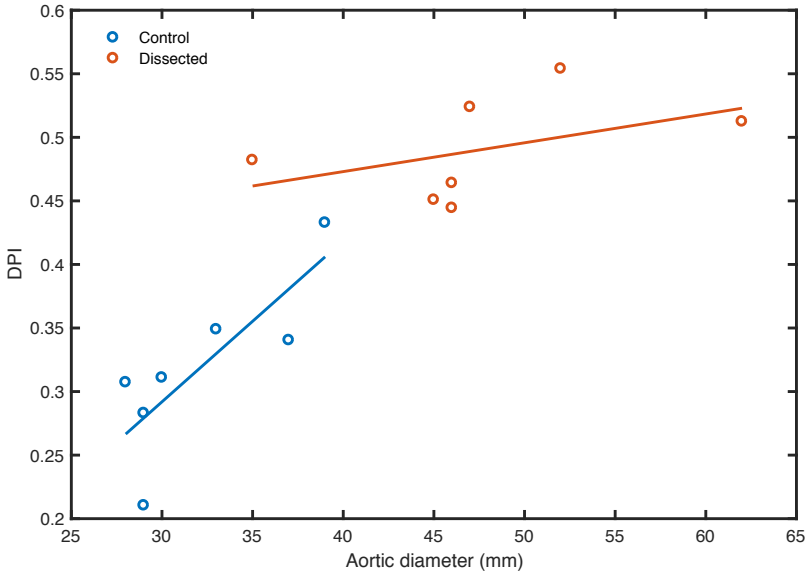

Figure 6.8: Evolution of DPI with diameter for control and dissection cohorts

on the greater curvature of the aorta. Figure 6.10 shows that the longitudinal stress is a better predictor of the dissection location. The dissection location is situated in a region of elevated longitudinal stress.

6.4 DISCUSSION

As stated in the literature, the selection of a 5.5 cm diameter criterion for elective surgery prior to aortic dissection is controversial due to the high number of patients experiencing dissection below the threshold[33]. Computational study of type A aortic dissection is hampered by the difficultly of obtaining pre-dissection aortic imaging. By usage of a dissection cohort with pre-dissection CTA imaging available, we were able to explore the changes to aortas known to have dissected over a period of time before the dissection event. Further, perioperative scans of the aorta were able to identify dissection locations on a aortic geometry amenable to finite element simulation. Further, the chosen cohorts show the effect of the

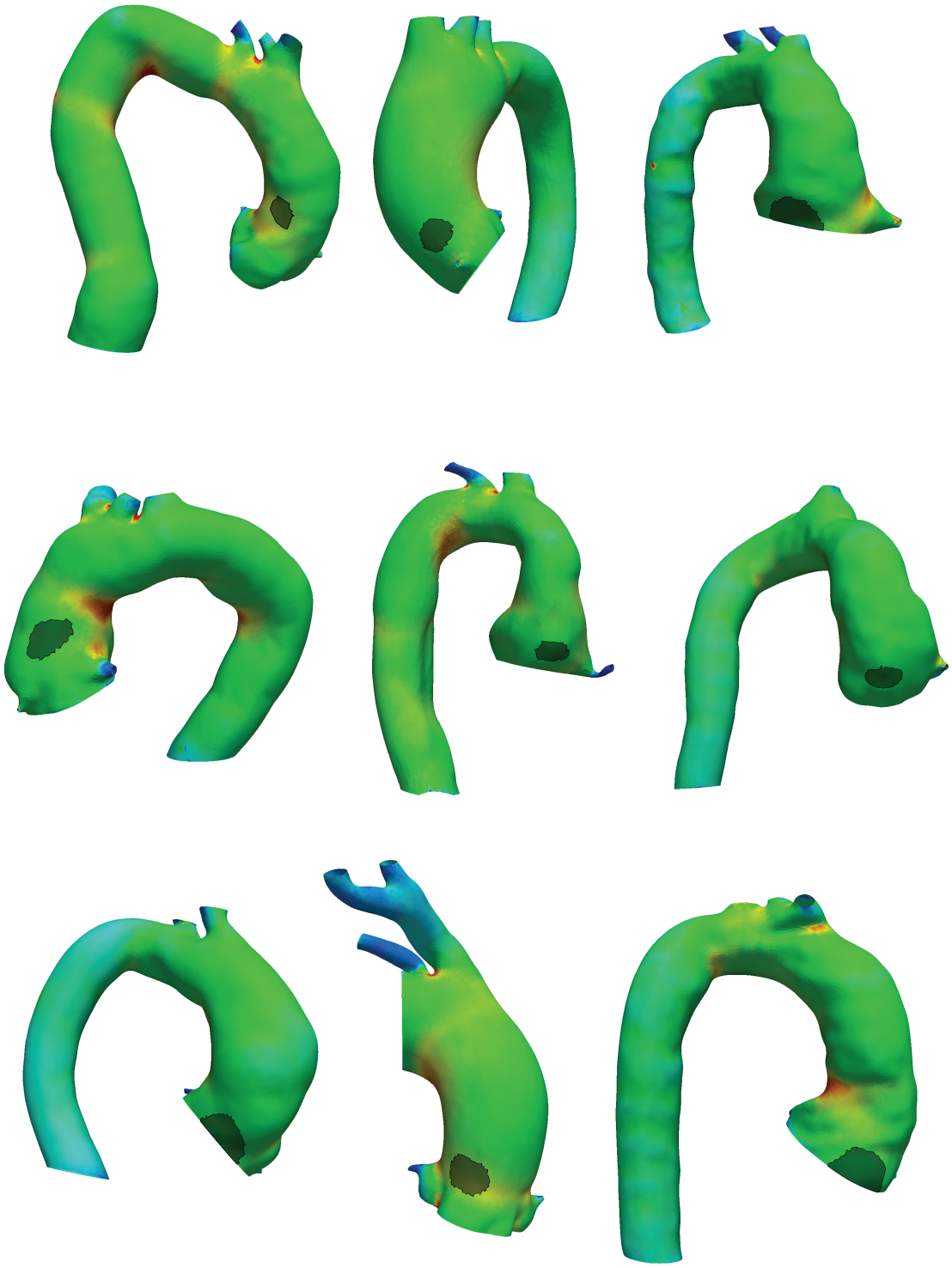

Figure 6.9: σ_{CIRC} contours on the dissected aortas. The grey region denotes the location of the dissection initiation.

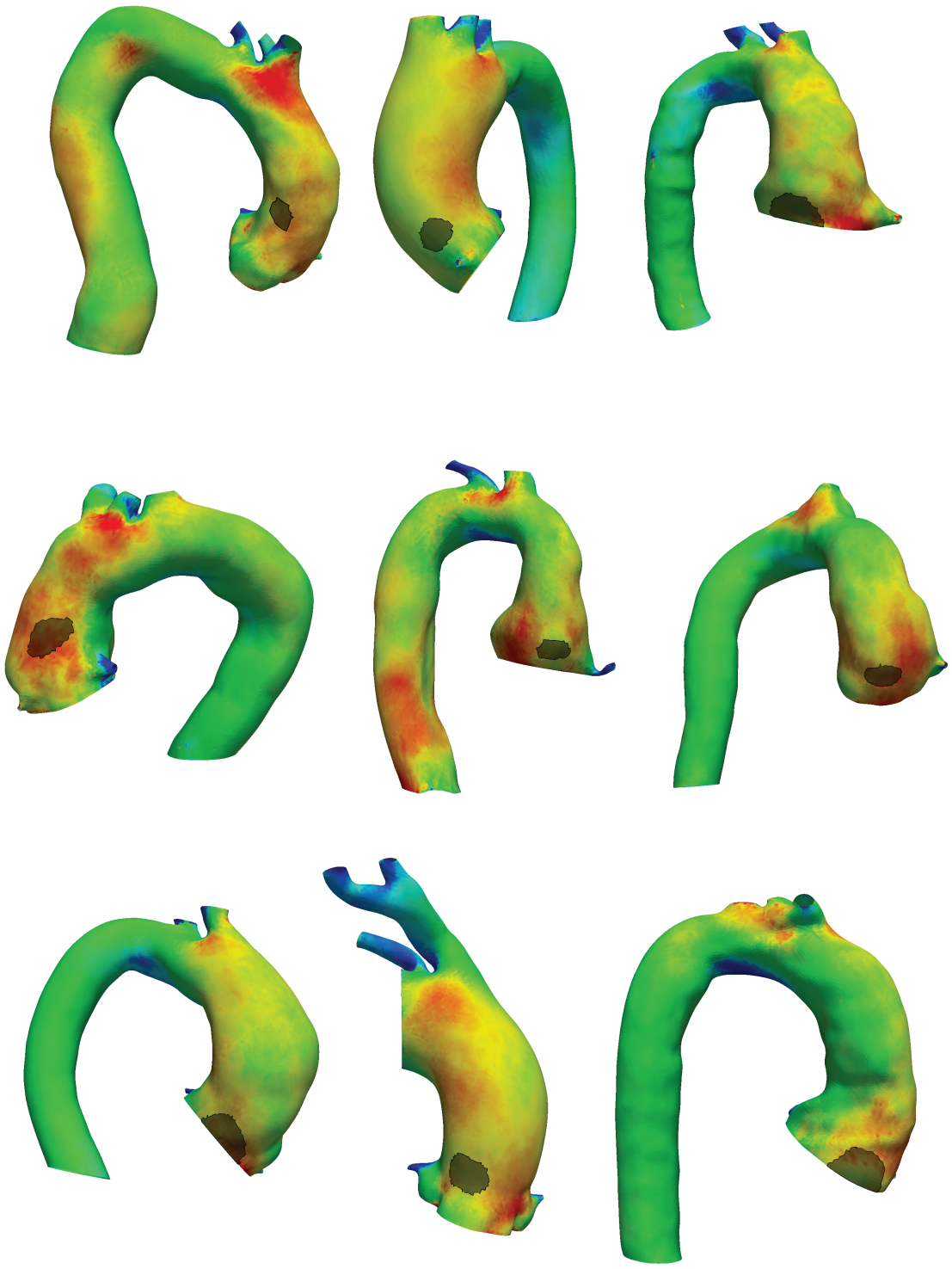

Figure 6.10: σ_{LONG} contours on the dissected aortas. The grey region denotes the location of the dissection initiation.

5.5 cm diameter criterion. The aorta diameter for patients in the dissected set were <5.5 cm, the current criterion for surgical intervention.

The DPI calculated for all patients (both in the dissected and control cohorts) was markedly less than the dissection value of 1.0. One interpretation of these results would be that there is thus no potential for dissection. However, as with safety factors used in other engineering disciplines, no margin of safety is not recommended. For this metric in particular, there are significant sources of error inherent in the calculation. Some of these include visualization errors, sudden spikes in blood pressure (caused by e.g. heavy exercise), and a non-invasive estimate of tissue strength. However, even with these caveats, there was a significant increase in the DPI in the dissected cohort. Further, we noted an increase in the index over time. Of note is that while DPI increased over time, the maximum orthogonal diameter as measured clinically did not which provides further evidence that the current aortic diameter criterion is not sufficient for patients at risk of aortic dissection. Together these results suggest that the proposed index is capable of predicting relative dissection risk.

Independent of the computational biaxial data shown in Chapter 5, Figures 6.9 and 6.9 show that the LONG stress and strength are the limiting values for dissection in the aorta. While the stress in the circumferential direction was elevated with respect to the longitudinal stress, the locations of highest circumferential stress did not occur in the clinically extracted dissection initiation sites. The conclusions of these data are contrary to the majority of the literature. Finite element simulations published by our group and others have highlighted the region of highest stress (either von Mises or CIRC) as potential dissection sites [162, 58, 75, 68, 1]. One exception to this is the work by Beller et al[64] who, as in this work, suggest that the longitudinal stress is higher in areas of interest.

Beyond showing that the LONG stress and strength are the limiting factors in aortic dissection, this chapter has shown that dissection must be controlled by more than purely the aortic diameter. Figure 6.8 shows that while DPI tracks aortic diameter for control (non-aneurysmal) patients, there is minimal increase in DPI with diameter for patients known to experience dissection. This shows that the full shape of the aorta, instead of the diameter alone, controls the dissection risk. Also note that the DPI in the figure appears to be capped at approximately 0.55. Conceptually, a limit below 1.0 is not unexpected as

uncertainty in model parameters in addition to phenomena not able to be captured by our model: localized damage to the aortic wall (such as an intimal tear) or a spike in the blood pressure may elevate the DPI to the failure limit. Further study will be required to quantify the response under these conditions to determine the effect on the DPI and whether there is an upper limit to the metric. In general however, for dissection to occur two things must occur. The biaxiality ratio must be high. Under this condition, the dissection event will be controlled by the LONG stress and strength of the aorta. Second, the LONG stress in the aorta must be elevated. Low LONG stress will not lead to failure, even if the aorta is limited by the behavior in that direction.

6.4.1 Limitations

This study was based on a relatively small sample size. The rarity of patients presenting with aortic dissection with pre-dissection CTA imaging available is a small subset of the entire TAAD surgical repair population. More patients will be required to show that the data presented herein apply to a broader population. Moreover, we considered only patients with a tricuspid aortic valve and no genetic disease. Again this is only a subset of the entire population with increased risk of aortic dissection for the two excluded groups well discussed in the literature. However, we don't anticipate a marked change in the results by increasing the number of patients or adding the previously excluded groups. The rational for the DPI is based on well established failure mechanics principals. The proposed DPI divides the stress in the aorta by the strength. For use in a clinical setting, the strength of the aorta must be estimated in a non-invasive manner. We have used an average cohort-specific value for this value, but the literature[75] shows a large variation in the strength. While the average strength is sufficient for determining an approximate risk, an individualized estimate would allow for more meaningful assessment. We are currently working on developing a model of patient-specific strength based on patient age, gender, hypertension status, and aortic diameter. A preliminary study based on this idea is shown in Appendix B. This study only included patients with a tricuspid aortic valve as no patients with a bicuspid aortic valve and fitting our inclusion criteria for the dissection cohort were available. This patient group

is of significant interest in the clinical community however and inclusion in a future study would improve the utility of the proposed DPI. Finally, we assumed no movement of the boundaries of the aorta models for the simulations. While such assumptions are common in the literature[58, 68, 1], recent work has shown that there is significant longitudinal strain in the ascending thoracic aorta due to motion of the aortic root during the cardiac cycle[166, 167, 168]. While the inclusion of such data is not expected to significantly change the primary conclusions of this work, it is likely to increase the longitudinal stress and thus the DPI. The magnitude of the change is a topic for a future work.

6.5 CONCLUSIONS

The work shown in this chapter demonstrates a potential improvement over the current 5.5 cm criterion for aortic dissection risk. Through comparison with non-aneurysmal patients, we show that the proposed DPI is significantly higher in patients experiencing dissection - even with aortic diameters below the current threshold. Further, we show that the DPI increases over time as the aorta shape evolves. Finally, the locations of higher DPI correspond to clinically determined regions for aortic dissection initiation. Together these results suggest that the proposed metric could be the basis for a new evidence based non-invasive method for assessing the risk of aortic dissection. This metric is simple, relying only on estimated cohort averaged tissue strength and a finite element analysis of CT image derived aortic geometry.

7.0 CONCLUSIONS

This thesis has presented a structurally motivated model of the aortic media which captures the tissue response across the entire loading regime. Both the prefailure and failure response follows experimentally gathered data. All parameters are physically motivated and may be gathered through experimental testing. These microscale simulations show the complex interplay between the non-fibrous matrix components and the fibrous networks embedded within. The microstructurally based model of the aortic media was used to determine the behavior of the tissue under biaxial loading. These results were used in conjunction with patient-specific aortic geometries to predict the risk of aortic dissection. We found that there was an elevated risk of dissection, as computed by our proposed dissection risk index (DPI), in patients known to have presented with acute Type A aortic dissection when compared to a control set of patients. The DPI presented has the potential to become a clinically viable tool in the assessment of patients at high risk of aortic dissection.

7.1 SPECIFIC AIM 1: DEVELOPMENT OF AN ASCENDING THORACIC AORTIC WALL MEDIA EMBEDDED-FIBER FINITE ELEMENT MODEL

This aim developed a structural microscale model of the aortic media. From simple material behavior of the constituents of the model, the fibers were modeled with a bilinear stress-stretch response and the non-fibrous matrix with a 1-parameter neoHookean material, the RVE was able to accurately capture the non-linear stress-stretch response of the tissue. The elastin fibers and non-fibrous matrix controlled the response in the initial portion of the

stress-stretch curve while the stiff region of the curve was dominated by the contribution of the collagen fibers.

The RVE developed was based on physically meaningful parameters. All inputs to the model were physically meaningful. The fiber network properties: areal density, fiber orientation, fiber diameter, fiber length, and intersection density can all be gathered through well known imaging techniques such as multiphoton microscopy. The fitted fiber properties: fiber stiffness and fiber recruitment stretch were both found to fall within the experimentally gathered range. Recruitment stretch (or fiber crimp), the amount of stretch before the fiber bears load, may be experimentally estimated via microscopy. The only non-fibrous material parameter was the shear modulus of the non-fibrous matrix.

The model developed in this aim illustrated the importance of a structural model of the tissue. While macroscale stresses were equivalent to those gathered through physical experimentation, the local stress-state in the tissue was highly heterogeneous after recruitment of the collagen fibers. This heterogeneity was caused by disruption in the collagen network, with disruptions of "stress-paths" leading to localized stresses double that seen in the stress-stretch response. Indeed the local fiber density was inversely correlated with the local non-fibrous matrix stress.

We showed that there was significant reorientation of the collagen network over the course of the analysis although those fibers orthogonal to the loading direction experienced minimal reorientation. Interestingly, an evaluation of the percentage of load bearing fibers showed a rapid increase in the fibers bearing load. Saturation of the load-bearing fibers was at 90%, the 10% not bearing load corresponding to the orthogonal fibers in the network.

7.2 SPECIFIC AIM 2: DETERMINE HOW THE MICROSCALE FAILURE RESPONSE AFFECTS FAILURE UNDER PHYSIOLOGICALLY RELEVANT LOADING

Within this aim, the previous aim was expanded to the failure regime. A similar model of the lamellar unit of the aortic media was constructed using the embedded-fiber finite

element model previously developed. The relatively low contribution of the elastin to the stress-stretch response influenced our decision to forgo explicit modeling of the elastin fibers. Instead, the dense elastin fiber network of the previous model was included as an isotropic solid. As the stress-state in the aorta is not uniaxial, the simulations performed in this chapter loaded the RVE uniaxially in the two directions described in the literature: CIRC and LONG. Failure was introduced via an addition to the constitutive relationship of the collagen fibers. To better highlight the utility of the model, three clinically relevant patient populations were considered: non-aneurysmal with tricuspid aortic valve (CTRL), aneurysmal with tricuspid aortic valve (TAV), and aneurysmal with bicuspid aortic valve (BAV).

The model parameters were fit to the experimental data in the CIRC direction. We then predicted the response in the LONG direction and compared to the experimental data. The fitted model was not statistically different from the experimental data in either the CIRC or LONG directions.

Simulations showed that there was a significant difference in the percentage of the load-bearing fibers when loaded in the CIRC versus the LONG direction. Roughly 85% of the fibers were loaded when load was applied in the CIRC direction. When loaded in the LONG direction however, only 30% of the fibers bore load. This corresponds well with the strength data in those directions. The strength in the LONG direction was approximately half that in CIRC.

As with the prefailure experiments, significant localized stress concentrations were seen in the non-collagenous matrix in areas of localized fiber disruption. As that stress was well in excess of the failure stress of elastin, this suggests full failure of the material in those regions.

We propose a simple rule of mixtures to predict the tissue strength of the aorta. This model is able to predict the strength fairly well for all populations. The only parameter in the simplified model that can not be gathered from physical experiment is the percentage of loaded fibers. The importance of this parameter suggests that the tissue strength is dependent on this percentage and further that the percentage is governed by the fiber network. The effect of network properties on the mechanical response of the tissue is a future area of study for this work.

After simulation of the tissue response under uniaxial loading, we devised a biaxial loading scenario that was able to simulate all likely ratios of CIRC and LONG stress *in vivo*. We showed that the biaxial loading simulations were able to match the existing experimental data - both uniaxial and equibiaxial. In alignment with experimental data, we found that equibiaxial loading on the tissue was governed by the longitudinal strength of the tissue. Moreover, we found that there was a sharp transition from a physiological strength approximating the uniaxial strength to a strength approximating the uniaxial longitudinal strength. The transition point was observed at 0.59 for control and 0.69 for aneurysmal tissues. Based on theoretical knowledge of the stress-state in idealized cylinders and spheres, we know that the ratio is likely to be between 0.5 and 1.0. Our previous simulations show a significantly higher circumferential strength. Further, we know that the ratio will rise in aneurysmal tissues. Together, these data suggests that aortic strength is likely governed by the longitudinal strength, with aneurysmal aortas more likely to be limited by that value.

7.3 SPECIFIC AIM 3: CONSTRUCTION OF A PREDICTIVE DISSECTION RISK METRIC

Using the results from the previous two aims as well as patient-specific aorta geometries, we have proposed a new dissection risk index as an alternative over the current clinical used 5.5 cm aortic diameter criterion. We showed that the proposed DPI is significantly higher in patients who presented with acute Type A dissection versus control patients. Further, the DPI increased over time for all dissection cohort patients studied. As validation of our new metric, we compared the locations of elevated DPI with clinically observed dissection initiation sites. These data suggest that the proposed metric has potential as a improved assessment of dissection risk.

7.4 LIMITATIONS

The first two aims are limited primarily by the difficulty in gathering the input parameters for the model. The microscopy and uniaxial stress-stretch testing required to fit the model are, by necessity, destructive tests. This removes the ability for simulation with patient specific parameters. The literature is also sparse on physiologically relevant loading conditions. The predominantly available mechanical data are done uniaxially whereas the stress-state in the aortic wall is biaxial. Finally, while the RVE includes only the aortic media, we believe this to be a valid assumption as dissection occurs within the media.

In aim 3, the difficulty in obtaining patients for whom pre-dissection CT imaging is available limits the sample size. While a novel study, more data are needed to ensure that the proposed metric is able to accurately predict the dissection risk.

7.5 FUTURE WORK

The model developed in this work has been specialized for the aortic wall. This is not an inherent limitation of the model, it is applicable to a wide array of fibrous tissues. At its heart, we have constructed a model which includes a number of discrete fibers (represented as bar elements) embedded within an isotropic non-fibrous matrix. Expanding this work beyond the aorta into tissues (e.g. vasculature in other parts of the body, tendon, etc.) is an obvious direction for future research.

To further the utility of the structural model for aortic tissue, one potential area of future study is the effect of the network parameters on the tissue response. A preliminary study of these effects was conducted in Chapter 2, but it used an exponential fiber model and a voronoi tessellation for the fiber network. The material model did not allow for fiber failure and a different network generation procedure used in Chapter 4. A parametric study of the parameters with a network based on the current model would allow for better understanding of the tissue behavior under varying fiber direction, degree of orientation, and areal density.

Utilizing the method described in Chapter 6 will require additional validation. Specifically, the cohorts used consisted of nine patients each. Expanding to more patient geometries is needed to prove that the metric is more widely applicable. Further, this method could include more patient specific data in the DPI calculation. An non-invasive estimate of a patient-specific tissue strength (described in Appendix B) could provide a method for doing so. Finally, work could also be done to increase the usability in a clinical setting. While the current method is feasible for use in a clinical setting - requiring model creation from CT imaging and a finite element simulation, moving towards a shape based metric is a tantalizing next step. Completion of such a model would require a better understanding of the curvature of the aorta. Data reported in Chapter 6 suggests that curvature may prove a significant effect on the DPI. While the diameter remains relatively constant over time, we showed that the DPI increased. This suggests that it is shape change in the aorta causing a higher risk of dissection over time. A study of the relevant curvatures, in the circumferential and longitudinal directions, is likely to be a fruitful area of interest. This would include both a comparison of the curvature between cohorts as well as within a patient over time. Further improvement of the DPI may be obtained through the inclusion of additional patient-specific parameters. In addition to a patient-specific strength (as detailed above), inclusion of patient-specific root motion and regionally varying material parameters are potential future work. Inclusion of patient-specific strength and an estimate of the degree of variation in the strength within the aorta would both require additional biomechanical testing. As these would require *ex vivo* testing, they would not be capable of providing patient-specific parameters directly, but instead a statistical model for the estimate of the values based on clinically obtainable data (diameter, age, gender, BMI, etc.). Patient-specific aortic root motion could be obtained non-invasively via echocardiograph gated CT imaging. As stated in the discussion of the dissection potential index chapter, patients with a bicuspid aortic valve were excluded from the study due to lack of patients meeting the rest of the inclusion criteria. However these patients are of significant interest clinically and study of them would improve the utility of the proposed DPI. Future work should attempt to include these patients. Finally, the importance of the shape and strength of the aorta on the DPI is not fully understood. A

parametric study of these parameters, either on patient of idealized geometry would show which material properties and aortic geometries are at elevated risk of aortic dissection.

APPENDIX A

FINITE ELEMENT DETAILS

A.1 FINITE ELEMENT FORMULATION

Consider a body Ω in $\mathbb{R}^3$ subjected to external traction loads $\mathbf{T}$. Γ^{ex} denotes the external boundary of the body and Γ^{in} any internal boundaries. $\mathbf{T}$ and $\boldsymbol{\Delta}$ denote the traction and jump across the internal bodies, respectively. We define the following prinicpal of virtual work

$$\int_{\Omega_0} \mathbf{S} : \delta\mathbf{E} \mathrm{d}\Omega_0 + \int_{\Omega_0} \rho_0 \ddot{\mathbf{d}} \cdot \delta\mathbf{d} \mathrm{d}\Omega_0 - \int_{\Gamma_0^{ex}} \mathbf{T}_{ex} \cdot \delta\mathbf{d} \mathrm{d}\Gamma_0^{ex} - \int_{\Gamma_0^{in}} \mathbf{T} \cdot \delta\boldsymbol{\Delta} \mathrm{d}\Gamma_0^{in} = 0 \tag{A.1}$$

with $\mathbf{E}$ the Green-Lagrange strain tensor and $\mathbf{S}$ the second Piola-Kirchhoff stress tensor. The subscripts 0 refer to values in the initial configuration.

The membrane code used in Chapter 6 uses an explicit, central difference, time-stepping algorithm to determine the displacement for each time-step of the simulation. The algorithm is derived from Belytschko ([164], box 6.1). Pseudocode is given in Algorithm 3.

Where n is the time step number with $n+1$ denoting the next step and Δt denoting the time step size. $\mathbf{R}_{in}$ and $\mathbf{R}_{co}$ are the global internal and cohesive force vectors and $\mathbf{M}^{-1}$ is the mass matrix. The nodal displacement, velocity, and acceleration vectors are given by $\mathbf{d}$, $\mathbf{v} = \dot{\mathbf{d}}$ and $\mathbf{a} = \dot{\mathbf{v}} = \ddot{\mathbf{d}}$, respectively.

For both the dynamic membrane code and the quasi-static volumetric code, the local internal force vector for element e is given by

$$\mathbf{R}_{in}^e = \int_{\Omega^e} \mathbf{B}_I^0 T \mathbf{S} \mathrm{d}\Omega^e \tag{A.2}$$

Algorithm 3 Explicit time stepping algorithm for membrane analysis

for $n = 0$ to n_{max} **do**

Compute $\mathbf{R}_{in}$ and $\mathbf{R}_{co}$

$\mathbf{a}^{(n+1)} \leftarrow \mathbf{M}^{-1}\left(\mathbf{R}_{in}^{(n+1)} - \mathbf{R}_{co}^{(n+1)}\right)$

$\mathbf{v}^{(n+1)} \leftarrow \mathbf{v}^{(n)} + \Delta t/2\left(\mathbf{a}^{(n+1)} + \mathbf{a}^{(n)}\right)$

$\mathbf{d}^{(n+1)} \leftarrow \mathbf{d}^{(n)} + \Delta t\mathbf{v}^{(n)} + 1/2\Delta t^2\mathbf{a}^{(n)}$

end for

with the volume of the element Ω^e and $\mathbf{B}_I^0$ the strain displacement matrix.

THe local cohesive force vector is given by

$$\mathbf{R}_{coh}^e = \int_{\Gamma^e} \mathbf{N}^T \mathbf{T} \mathrm{d}\Gamma^e \tag{A.3}$$

where Γ^e is the area of the cohesive element. $\mathbf{N}$ denotes the shape functions for the element.

Global internal force and cohesive force vectors are constructed by summing over the elements.

$$\mathbf{R} = \sum_{i=1}^{n} \mathbf{R}^i \tag{A.4}$$

The cohesive tractions are governed by the bilinear traction-separation law developed by Geubelle and Baylor [169]. The tractions in the shear and normal directions are given by

$$T_i = \frac{S}{1-S}\frac{\Delta_i}{\Delta_{ic}}\frac{\sigma_{max}}{S_{init}} \tag{A.5}$$

where the subscript i defines the direction of the traction. S represents a monotonically decreasing damage parameter, S_{init} the initial damage, σ_{max} the cohesive strength in the normal (or shear direction), Δ_i the current opening in the i direction, and Δ_{ic} the critical opening in the i direction.

$S \in [0, 1]$ with $S = 1$ denoting no damage to and $S = 0$ denoting full failure of the cohesive element. The parameter is computed with

$$S = \min\left(S_{min}, \langle 1 - \left\|\tilde{\Delta}\right\|\rangle\right) \tag{A.6}$$

with $|\cdot\|$ the l_2 norm. $\tilde{\Delta}$ is the normalized displacement jump $\tilde{\Delta} = \Delta/\Delta_c$. $\langle\cdot\rangle$ is defined as

$$\langle x \rangle = \begin{cases} x, & \text{if } x > 0 \\ 0, & \text{else} \end{cases} \tag{A.7}$$

To construct the local internal force array, we consider a particle $\mathbf{X}$ in the reference configuration and the same particle, $\mathbf{x}$, in the current configuration. The deformation gradient is defined as

$$\mathbf{F} = \frac{\partial \mathbf{x}}{\partial \mathbf{X}} \tag{A.8}$$

From the deformation gradient, the right Cauchy-Green deformation tensor is given as

$$\mathbf{C} = \mathbf{F}^T\mathbf{F} \tag{A.9}$$

To account for large deformation of rotations, the non-linear Lagranian strain tensor $\mathbf{E}$ is used.

$$\mathbf{E} = \frac{1}{2}(\mathbf{C} - \mathbf{I}) \tag{A.10}$$

where $\mathbf{I}$ is the identity tensor.

The stress is then given by

$$\mathbf{S} = \frac{\partial \Psi(\mathbf{E})}{\partial \mathbf{E}} \tag{A.11}$$

where Ψ is the strain energy density functional for the material. Many different material models may be used to define the constitutive behavior of the material. One potential model, used to simulate the non-fibrous portion of aortic tissue in Chapters 3 and 4 is given in Section A.2.

A.2 AN ISOTROPIC NEARLY ISOTROPIC NEOHOOKEAN MATERIAL

The strain-energy functional for a material may be additively decomposed into its volumetric and isochoric parts as

$$\Psi = \Psi_{vol}(J) + \Psi_{iso}(\mathbf{C}) \tag{A.12}$$

where the volumetric contribution, Ψ_{vol} is a function of the Jacobian $J = \det\mathbf{F}$ of the material and the isochoric contribution, Ψ_{iso} is a function of the right Cauchy-Greeen deformation tensor $\mathbf{C} = \mathbf{F}^T\mathbf{F}$. The deformation gradient tensor $\mathbf{F} = \mathrm{d}\mathbf{x}/\mathrm{d}\mathbf{X}$ relates the material point in the reference configuration ($\mathbf{X}$) and the current configuration ($\mathbf{x}$).

For the isochoric portion of the strain energy, a 1-parameter neoHookean material model has been chosen.

$$\Psi_{iso} = \frac{\mu}{2}\left(I_1 - 3\right) \tag{A.13}$$

where μ is the shear modulus of the material and $I_1 = \mathrm{tr}\mathbf{C}$ is the first invariant of the right Cauchy-Green deformation tensor.

The volumetric part of the strain energy functional is given by

$$\Psi_{vol} = \frac{1}{2}\kappa\left(J - 1\right)^2 \tag{A.14}$$

where κ is a penalty term related to the bulk modulus of the material.

The Second Piola-Kirchhoff stress is given by

$$\mathbf{S} = 2\frac{\partial\Psi}{\partial\mathbf{C}} \tag{A.15}$$

Or, equivalently, due to the additive decomposition of the strain energy functional,

$$\mathbf{S} = 2\frac{\partial\Psi}{\partial\mathbf{C}} = \mathbf{S}_{vol} + \mathbf{S}_{iso} \tag{A.16}$$

The volumetric and isochoric parts of the stress are equal to

$$\mathbf{S}_{vol} = Jp\mathbf{C}^{-1} \tag{A.17}$$

$$\mathbf{S}_{iso} = J^{-2/3}\mathbb{P} : \mu\mathbf{I} \tag{A.18}$$

$\mathbf{I}$ denotes the rank 2 identity tensor. The pressure, p, is defined as $p = \partial\Psi_{vol}/\partial J$.

Following the derivation given by [170], $\mathbb{P}$ denotes a projection tensor in the reference configuration $\mathbb{P} = \mathbb{I} - \mathbf{C}^{-1} \otimes \mathbf{C}$ where $\mathbb{P} = P_{ijkl} e_i \otimes e_j \otimes e_k \otimes e_l$ and $\mathbb{I} = \delta_{ik}\delta_{jl} e_i \otimes e_j \otimes e_k \otimes e_l$ where δ_{ij} denotes the Kronecker delta.

APPENDIX B

A NON-INVASIVE STRENGTH MEASURE OF ASCENDING THORACIC AORTA TISSUE

This appendix provides a potential method for a non-invasive estimate of the strength of ascending thoracic aorta tissue. A preliminary study is conducted using a mixed-effect model to construct an equation of tissue strength in both the circumferential and longitudinal directions developed from a retrospective study of uniaxial tensile stress-strain data previously reported by Pichamuthu et al.[75].

B.1 METHODS

Uniaxial tensile testing was performed on tissue samples collected from 43 patients who underwent elective ascending thoracic aorta surgery. IRB approval and informed patient consent was obtained prior to tissue harvest. Full details of the tissue collection and experimental testing is provided in Pichamuthu et al.[75]. Following the work of Vande Geest et al.[171], patient statistics expected to be predictors of tissue strength were collected from each patient. Using a linear mixed-effect model (fitlme, Matlab 2017a, Mathworks, Natick, MA), an equation of tissue strength was created. Variables were removed from the model if their associated p-value was greater than 0.10. Four patient statistics were explored in the model: the patient gender (G=0 for females, 1 for males), age (A in years), aortic diameter (D in mm), and valve type (either TAV=0 or BAV=1). Strength, S, is reported in

N/cm^2. Patients with missing data were excluded from the study (2 of 43). The generalized statistical model was of the form

$$S = \beta_0 + \beta_1 \times G + \beta_2 \times A + \beta_3 \times D + \beta_4 \times V \tag{B.1}$$

where $\beta_0 \ldots \beta_4$ are the regression coefficients.

Models were constructed for both the strength in the circumferential and longitudinal directions. Depending on the size of the excised tissue, multiple uniaxial tests were performed in the circumferential and longitudinal directions. The 41 patients provided 189 strength values (97 circumferential, 91 longitudinal). Patient ID was considered as a grouping variable to account for the repeated measures.

B.2 RESULTS

B.2.1 Circumferential strength

A mixed-effect model for circumferential strength yielded the following equation

$$S_{CIRC} = 267.0 - 1.9 \times A - 38.6 \times V \tag{B.2}$$

with the strength in N/cm^2m the age in years and the valve type (TAV=0, BAV=1). The data for the mixed-effect model are given in Table B1. The model shows that there is a decrease in circumferential strength for both TAV patients and older patients. The p-values for gender and diameter were greater than the cutoff of 0.10 and were thus not included in the final model.

Table B1: Mixed-effect model for circumferential strength

S_{CIRC} (MPa)						
Effect	valve type	Estimate	Std Error	DF	t value	$Pr > \|t\|$
Intercept		267.0	49.1	38	5.44	¡0.0001
valve type	0	-38.6	18.6	52	-2.07	0.0434
valve type	1	0	-	-	-	-
age		-1.88	0.90	52	-2.09	0.0418

B.2.2 Longitudinal strength

For the strength in the longitudinal direction, the same process was repeated. After fitting the mixed-effect model, the following equation was found.

$$S_{LONG} = 70.8 - 13.8 \times V \tag{B.3}$$

with the strength in N/cm^{2}m and the valve type (TAV=0, BAV=1). The data for the mixed-effect model are given in Table B2. The valve type was the only significant variable in the final model. The p-values for the age, gender, and diameter were all above the exclusion threshold.

B.3 CONCLUSIONS

The mixed-effect modeling showed that there was a significant effect of valve-type on the strength in both the circumferential and longitudinal directions. This follows reported data, where there is significant difference in the strengths in those directions. While age was a significant factor in the circumferential direction, it was not significant in the longitudinal direction. Interestingly, the diameter was not a significant factor in either direction. This

Table B2: Mixed-effect model for longitudinal strength

S_{CIRC} (MPa)						
Effect	valve type	Estimate	Std Error	DF	t value	$Pr > \|t\|$
Intercept		70.8	4.4	33	16.1	¡0.0001
valve type	0	-13.8	6.7	52	-2.04	0.0460
valve type	1	0	-	-	-	-

suggests that the increase in dissection risk with aortic diameter is not due to a reduction in tissue strength. This preliminary study was hampered by the fact that this was a retrospective study of previously collected data. For this reason, only a subset of the potentially important patient statistics were available. Future work should include more patients and other risk factors for aortic dissection: body mass index, hypertension, atherosclerosis, and family history of aortic dissection.

BIBLIOGRAPHY

[1] S. Pasta, J. A. Phillippi, A. Tsamis, A. D'Amore, G. M. Raffa, M. Pilato, C. Scardulla, S. C. Watkins, W. R. Wagner, T. G. Gleason, D. A. Vorp, Constitutive modeling of ascending thoracic aortic aneurysms using microstructural parameters, Medical Engineering and Physics 38 (2016) 121–130. doi:10.1016/j.medengphy.2015.11.001.

[2] R. G. Koch, A. Tsamis, A. D'Amore, W. R. Wagner, S. C. Watkins, T. G. Gleason, D. a. Vorp, A custom image-based analysis tool for quantifying elastin and collagen micro-architecture in the wall of the human aorta from multi-photon microscopy, Journal of Biomechanics 47 (5) (2014) 935–943. doi:10.1016/j.jbiomech.2014.01.027.
URL http://dx.doi.org/10.1016/j.jbiomech.2014.01.027

[3] T. P. Tran, A. Khoynezhad, Current management of type B aortic dissection, Vascular Health and Risk Management 5 (2009) 53–63.

[4] H. Gray, Anatomy of the Human Body, 20th Edition, Lea & Febiger, Philidelphia, 1918.
URL http://www.bartleby.com/107/

[5] J. A. Phillippi, B. R. Green, M. A. Eskay, M. P. Kotlarczyk, M. R. Hill, A. M. Robertson, S. C. Watkins, D. A. Vorp, T. G. Gleason, Mechanism of aortic medial matrix remodeling is distinct in patients with bicuspid aortic valve, Journal of Thoracic and Cardiovascular Surgery 147 (2014) 1056–1064. doi:10.1016/j.jtcvs.2013.04.028.
URL http://dx.doi.org/10.1016/j.jtcvs.2013.04.028

[6] S. Pasta, A. Rinaudo, A. Luca, M. Pilato, C. Scardulla, T. G. Gleason, D. A. Vorp, Difference in hemodynamic and wall stress of ascending thoracic aortic aneurysms with bicuspid and tricuspid aortic valve, Journal of Biomechanics 46 (10) (2013) 1729–1738. doi:10.1016/j.jbiomech.2013.03.029.
URL http://dx.doi.org/10.1016/j.jbiomech.2013.03.029

[7] S. A. Lemaire, L. Russell, Epidemiology of thoracic aortic dissection, Nature Reviews Cardiology 8 (2011) 103–113. doi:10.1038/nrcardio.2010.187.
URL http://dx.doi.org/10.1038/nrcardio.2010.187

[8] D. Pacini, L. Di Marco, D. Fortuna, L. M. B. Belotti, D. Gabbieri, C. Zussa, F. Pigini, A. Contini, M. C. Barattoni, R. De Palma, R. Di Bartolomeo, Acute aortic dissection

: Epidemiology and outcomes, International Journal of Cardiology 167 (2013) 2806–2812. doi:10.1016/j.ijcard.2012.07.008.
URL http://dx.doi.org/10.1016/j.ijcard.2012.07.008

[9] I. Meszaros, J. Morocz, J. Szlavi, J. Schmidt, L. Tornoci, L. Nagy, L. Szep, Epidemiology and Clinicopathology of Aortic Dissection*: A Population-Based Longitudinal Study Over 27 Years, Chest 117 (5) (2000) 1271–1278. doi:10.1378/chest.117.5.1271.

[10] Y. Masuda, Z. Yamada, N. Morooka, S. Watanabe, Y. Inagaki, Prognosis of patients with medically treated aortic dissections, Circulation 84 (5 Suppl) (1991) III7–13.
URL http://europepmc.org/abstract/MED/1934444http://intl-circ.ahajournals.org/cgi/content/abstract/84/5/III7

[11] V. S. Ramanath, J. K. Oh, T. M. Sundt, K. a. Eagle, Acute aortic syndromes and thoracic aortic aneurysm., Mayo Clinic proceedings. Mayo Clinic 84 (5) (2009) 465–81. doi:10.1016/S0025-6196(11)60566-1.
URL http://www.pubmedcentral.nih.gov/articlerender.fcgi?artid=2676130{&}tool=pmcentrez{&}rendertype=abstract

[12] L. F. Hiratzka, G. L. Bakris, J. A. Beckman, R. M. Bersin, V. F. Carr, D. E. Casey, K. A. Eagle, L. K. Hermann, E. M. Isselbacher, E. A. Kazerooni, N. T. Kouchoukos, B. W. Lytle, D. M. Milewicz, D. L. Reich, S. Sen, J. A. Shinn, L. G. Svensson, D. M. Williams, 2010 ACCF/AHA/AATS/ACR/ASA/SCA/SCAI/SIR/STS/SVM Guidelines for the Diagnosis and Management of Patients With Thoracic Aortic Disease, Journal of the American College of Cardiology 55 (14) (2010) e27–e129. doi:10.1016/j.jacc.2010.02.015.
URL http://dx.doi.org/10.1016/j.jacc.2010.02.015

[13] E. Girdauskas, K. Disha, M. A. Borger, T. Kuntze, Risk of proximal aortic dissection in patients with bicuspid aortic valve: How to address this controversy?, Interactive Cardiovascular and Thoracic Surgery 18 (3) (2014) 355–359. doi:10.1093/icvts/ivt518.

[14] P. G. Hagan, C. A. Nienaber, E. M. Isselbacher, D. Bruckman, D. J. Karavite, P. L. Russman, A. Evangelista, A. G. Moore, J. F. Malouf, L. A. Pape, C. Gaca, W. F. Armstrong, G. M. Deeb, K. A. Eagle, The International Registry of Acute Aortic Dissection (IRAD) 283 (7).

[15] M. Pepin, U. Schwarze, A. Superti-Furga, P. H. Byers, Clinical and Genetic Features of Ehlers-Danlos Syndrome Type IV, the Vascular Type, N Engl J Med 342 (10) (2016) 673–680.

[16] B. L. Loeys, H. C. Dietz, A. C. Braverman, B. L. Callewaert, J. De Backer, R. B. Devereux, Y. Hilhorst-Hofstee, G. Jondeau, L. Faivre, D. M. Milewicz, R. E. Pyeritz, P. D. Sponseller, P. Wordsworth, A. M. De Paepe, The revised Ghent nosology for the Marfan syndrome., Journal of medical genetics 47 (7) (2010) 476–85. doi:10.1136/

jmg.2009.072785.
URL http://www.ncbi.nlm.nih.gov/pubmed/20591885

[17] I. A. Khan, C. K. Nair, Clinical, diagnostic, and management perspectives of aortic dissection, Chest 122 (1) (2002) 311–328. doi:10.1378/chest.122.1.311.
URL http://dx.doi.org/10.1378/chest.122.1.311

[18] D. P. J. Howard, E. Sideso, A. Handa, P. M. Rothwell, Incidence, risk factors, outcome and projected future burden of acute aortic dissection, Ann Cardiothorac Surg 3 (3) (2014) 278–284. doi:10.3978/j.issn.2225-319X.2014.05.14.

[19] W. D. Clouse, J. W. Hallett, H. V. Schaff, P. C. Spittell, C. M. Rowland, D. M. Ilstrup, L. J. Melton, Acute Aortic Dissection: Population-Based Incidence Compared with Degenerative Aortic Aneurysm Rupture, Mayo Clinic Proceedings 79 (2) (2004) 176–180. arXiv:arXiv:1011.1669v3, doi:10.4065/79.2.176.

[20] R. Erbel, F. Alfonso, C. Boileau, O. Dirsch, B. Eber, A. Haverich, H. Rakowski, J. Struyven, K. Radegran, U. Sechtem, J. Taylor, C. Zollikofer, W. W. Klein, B. Mulder, L. A. Providencia, Diagnosis and management of aortic dissection: Recommendations of the Task Force on Aortic Dissection, European Society of Cardiology, European Heart Journal 22 (18) (2001) 1642–1681. arXiv:euhj.2001.2782, doi:10.1053/euhj.2001.2782.

[21] M. A. Coady, J. A. Rizzo, G. L. Hammond, D. Mandapati, G. S. Kopf, J. A. Elefteriades, What is the Appropriate Size Criterion for Resection of Thoracic Aortic Aneurysms?, Journal of Thoracic and Cardiovascular Surgery 113 (3) (1997) 476–491.

[22] J. A. Elefteriades, Natural History of Thoracic Aortic Aneurysms: Indications for Surgery, and Surgical Versus Nonsurgical Risks, Annals of Thoracic Surgery 74 (5) (2002) S1877–S1880.

[23] F. A. Lederle, S. E. Wilson, G. R. Johnson, D. B. Reinke, F. N. Littooy, C. W. Acher, D. J. Ballard, L. M. Messina, I. L. Gordon, E. P. Chute, W. C. Krupski, S. J. Busuttil, G. W. Barone, S. Sparks, L. M. Graham, J. H. Rapp, M. S. Makaroun, G. L. Moneta, R. A. Cambria, R. G. Makhoul, D. Eton, H. J. Ansel, J. A. Freischlag, D. Bandyk, Immediate Repair Compared with Surveillance of Small Abdominal Aortic Aneurysms, New England Journal of Medicine 346 (19) (2002) 1437–1444. doi:10.1056/NEJMoa012573.
URL http://www.nejm.org/doi/abs/10.1056/NEJMoa012573

[24] D. C. Brewster, J. L. Cronenwett, J. W. Hallett, K. W. Johnston, W. C. Krupski, J. S. Matsumura, Guidelines for the treatment of abdominal aortic aneurysms: Report of a subcommittee of the Joint Council of the American Association for Vascular Surgery and Society for Vascular Surgery, Journal of Vascular Surgery 37 (5) (2003) 1106–1117. doi:10.1067/mva.2003.363.

[25] R. T. Hahn, M. J. Roman, A. H. Mogtader, R. B. Devereux, Association of aortic dilation with regurgitant, stenotic and functionally normal bicuspid aortic valves., Journal of the American College of Cardiology 19 (2) (1992) 283–8.
URL http://www.ncbi.nlm.nih.gov/pubmed/1732353

[26] R. R. Davies, L. J. Goldstein, M. A. Coady, S. L. Tittle, J. A. Rizzo, G. S. Kopf, J. A. Elefteriades, Yearly rupture or dissection rates for thoracic aortic aneurysms: Simple prediction based on size, Annals of Thoracic Surgery 73 (1) (2002) 17–28. doi:10.1016/S0003-4975(01)03236-2.

[27] D. M. Milewicz, Treatment of Aortic Disease in Patients With Marfan Syndrome, Circulation 111 (11) (2005) e150–e157. doi:10.1161/01.CIR.0000155243.70456.F4.
URL http://circ.ahajournals.org/cgi/doi/10.1161/01.CIR.0000155243.70456.F4

[28] D. J. Sahn, A. DeMaria, J. Kisslo, A. Weyman, Recommendations regarding quantitation in M-mode echocardiography: results of a survey of echocardiographic measurements., Circulation 58 (6) (1978) 1072–83. doi:10.1161/01.cir.58.6.1072.
URL http://www.ncbi.nlm.nih.gov/pubmed/709763

[29] A. Evangelista, F. A. Flachskampf, R. Erbel, F. Antonini-Canterin, C. Vlachopoulos, G. Rocchi, R. Sicari, P. Nihoyannopoulos, J. Zamorano, M. Pepi, O. A. Breithardt, E. Płońska-Gościniak, Echocardiography in aortic diseases: EAE recommendations for clinical practice, European Journal of Echocardiography 11 (8) (2010) 645–658. doi:10.1093/ejechocard/jeq056.

[30] K. Johnston, R. B. Rutherford, M. Tilson, D. M. Shah, L. Hollier, J. C. Stanley, Suggested standards for reporting on arterial aneurysms, Journal of Vascular Surgery 13 (3) (1991) 452–458. doi:10.1067/mva.1991.26737.
URL http://linkinghub.elsevier.com/retrieve/pii/0741521491700518

[31] G. G. Hartnell, Imaging of aortic aneurysms and dissection: CT and MRI, Journal of Thoracic Imaging 16 (1) (2001) 35–46. doi:10.1097/00005382-200101000-00006.

[32] G. J. Nollen, M. Groenink, J. G. P. Tijssen, E. E. Van Der Wall, B. J. M. Mulder, Aortic stiffness and diameter predict progressive aortic dilatation in patients with Marfan syndrome, European Heart Journal 25 (13) (2004) 1146–1152. doi:10.1016/j.ehj.2004.04.033.

[33] L. A. Pape, T. T. Tsai, E. M. Isselbacher, J. K. Oh, P. T. O'Gara, A. Evangelista, R. Fattori, G. Meinhardt, S. Trimarchi, E. Bossone, T. Suzuki, J. V. Cooper, J. B. Froehlich, C. A. Nienaber, K. A. Eagle, Aortic diameter 5.5 cm is not a good predictor of type A aortic dissection: Observations from the International Registry of Acute Aortic Dissection (IRAD), Circulation 116 (10) (2007) 1120–1127. doi:10.1161/CIRCULATIONAHA.107.702720.

[34] L. M. Parish, I. I. I. Gorman Joseph H., S. Kahn, T. Plappert, M. G. St. John-Sutton, J. E. Bavaria, R. C. Gorman, Aortic size in acute type A dissection: implications for preventive ascending aortic replacement, European Journal of Cardio-Thoracic Surgery 35 (6) (2009) 941–946.
URL http://dx.doi.org/10.1016/j.ejcts.2008.12.047

[35] B. Rylski, E. Branchetti, J. E. Bavaria, P. Vallabhajosyula, W. Y. Szeto, R. K. Milewski, N. D. Desai, Modeling of predissection aortic size in acute type A dissection: More than 90% fail to meet the guidelines for elective ascending replacement, Journal of Thoracic and Cardiovascular Surgery 148 (3) (2014) 944–948. doi:10.1016/j.jtcvs.2014.05.050.
URL http://dx.doi.org/10.1016/j.jtcvs.2014.05.050

[36] J. B. Kim, M. Spotnitz, M. E. Lindsay, T. E. MacGillivray, E. M. Isselbacher, T. M. Sundt, Risk of Aortic Dissection in the ModeratelyDilated Ascending Aorta, Journal of the American College of Cardiology 68 (11) (2016) 1209–1219. doi:10.1016/j.jacc.2016.06.025.

[37] C. T. Dotter, D. J. Roberts, I. Steinberg, Aortic Length: Angiocardiographic Measurements, Circulation 2 (6) (1950) 915–920. doi:10.1161/01.CIR.2.6.915.
URL http://circ.ahajournals.org/cgi/doi/10.1161/01.CIR.2.6.915

[38] M. J. Roman, R. B. Devereux, R. Kramer-Fox, J. O'Loughlin, Two-dimensional echocardiographic aortic root dimensions in normal children and adults, The American Journal of Cardiology 64 (8) (1989) 507–512. doi:10.1016/0002-9149(89)90430-X.
URL http://linkinghub.elsevier.com/retrieve/pii/000291498990430X

[39] J. I. E. Hoffman, S. Kaplan, The incidence of congenital heart disease, Journal of the American College of Cardiology 39 (12) (2002) 1890–1900. arXiv:NIHMS150003, doi:10.1016/S0735-1097(02)01886-7.
URL http://dx.doi.org/10.1016/S0735-1097(02)01886-7

[40] V. Garg, A. N. Muth, J. F. Ransom, M. K. Schluterman, R. Barnes, I. N. King, P. D. Grossfeld, D. Srivastava, Mutations in NOTCH1 cause aortic valve disease., Nature 437 (7056) (2005) 270–274. doi:10.1038/nature03940.

[41] E. W. Larson, W. D. Edwards, Risk factors for aortic dissection: A necropsy study of 161 cases, The American Journal of Cardiology 53 (6) (1984) 849–855. doi:10.1016/0002-9149(84)90418-1.

[42] B. H. Wolinsky, S. Glagov, A Lamellar Unit of Aortic Medial Structure and Function in Mammals, Circulation Research XX (1967) 99–112.

[43] J. M. Clark, S. Glagov, Transmural organization of the arterial media. The lamellar unit revisited., Arteriosclerosis (Dallas, Tex.) 5 (1) (1985) 19–34. doi:10.1161/01.ATV.5.1.19.

[44] M. K. O'Connell, S. Murthy, S. Phan, C. Xu, J. Buchanan, R. Spilker, R. L. Dalman, C. K. Zarins, W. Denk, C. A. Taylor, The three-dimensional micro- and nanostructure of the aortic medial lamellar unit measured using 3D confocal and electron microscopy imaging., Matrix biology : journal of the International Society for Matrix Biology 27 (3) (2008) 171–81. doi:10.1016/j.matbio.2007.10.008.
URL http://www.pubmedcentral.nih.gov/articlerender.fcgi?artid=2679973{&}tool=pmcentrez{&}rendertype=abstract

[45] H. Wolinsky, S. Glagov, Nature of species differences in the medial distribution of aortic vasa vasorum in mammals., Circulation research 20 (4) (1967) 409–421. doi:10.1161/01.RES.20.4.409.

[46] K. P. Dingemans, P. Teeling, J. H. Lagendijk, a. E. Becker, Extracellular matrix of the human aortic media: an ultrastructural histochemical and immunohistochemical study of the adult aortic media., The Anatomical record 258 (1) (2000) 1–14. doi:10.1002/(SICI)1097-0185(20000101)258:1<1::AID-AR1>3.0.CO;2-7.

[47] A. E. Li, I. Kamel, F. Rando, M. Anderson, B. Kumbasar, J. a. C. Lima, D. a. Bluemke, Using MRI to assess aortic wall thickness in the multiethnic study of atherosclerosis: distribution by race, sex, and age., AJR. American journal of roentgenology 182 (3) (2004) 593–597. doi:10.2214/ajr.182.3.1820593.
URL http://www.ncbi.nlm.nih.gov/pubmed/14975953

[48] M. J. Collins, J. F. Eberth, E. Wilson, J. D. Humphrey, Acute mechanical effects of elastase on the infrarenal mouse aorta: Implications for models of aneurysms, Journal of Biomechanics 45 (4) (2012) 660–665. doi:10.1016/j.jbiomech.2011.12.013.

[49] H. Weisbecker, C. Viertler, D. M. Pierce, G. A. Holzapfel, The role of elastin and collagen in the softening behavior of the human thoracic aortic media., Journal of biomechanics 46 (11) (2013) 1859–65. doi:10.1016/j.jbiomech.2013.04.025.
URL http://www.ncbi.nlm.nih.gov/pubmed/23735660

[50] M. D. Kertai, E. Boersma, C. M. Westerhout, R. van Domburg, J. Klein, J. J. Bax, H. van Urk, D. Poldermans, Association between long-term statin use and mortality after successful abdominal aortic aneurysm surgery, The American Journal of Medicine 116 (2) (2004) 96–103. doi:10.1016/j.amjmed.2003.08.029.
URL http://linkinghub.elsevier.com/retrieve/pii/S0002934303006314

[51] J. A. Elefteriades, E. A. Farkas, Thoracic Aortic Aneurysm. Clinically Pertinent Controversies and Uncertainties, Journal of the American College of Cardiology 55 (9) (2010) 841–857. doi:10.1016/j.jacc.2009.08.084.
URL http://dx.doi.org/10.1016/j.jacc.2009.08.084

[52] H. Ince, C. A. Nienaber, Etiology, pathogenesis and management of thoracic aortic aneurysm., Nature clinical practice. Cardiovascular medicine 4 (8) (2007) 418–427. doi:10.1038/ncpcardio0937.

[53] D. R. Gersony, M. A. McClaughlin, Z. Jin, W. M. Gersony, The effect of beta-blocker therapy on clinical outcome in patients with Marfan's syndrome: A meta-analysis, International Journal of Cardiology 114 (3) (2007) 303–308. doi:10.1016/j.ijcard.2005.11.116.
URL http://linkinghub.elsevier.com/retrieve/pii/S0167527306002373

[54] H. E. Achneck, J. A. Rizzo, M. Tranquilli, J. A. Elefteriades, Safety of Thoracic Aortic Surgery in the Present Era, Annals of Thoracic Surgery 84 (4) (2007) 1180–1185. doi:10.1016/j.athoracsur.2007.05.038.
URL http://dx.doi.org/10.1016/j.athoracsur.2007.05.038

[55] F. Lohse, N. Lang, W. Schiller, W. Roell, O. Dewald, C.-j. Preusse, A. Welz, C. Schmitz, Quality of Life after, Texas Heart Institute Journal 36 (2) (2009) 104–110.

[56] A. Karthikesalingam, S. S. Bahia, B. O. Patterson, G. Peach, A. Vidal-Diez, K. K. Ray, R. Sharma, R. J. Hinchliffe, P. J. Holt, M. M. Thompson, The shortfall in long-term survival of patients with repaired thoracic or abdominal aortic aneurysms: Retrospective case-control analysis of hospital episode statistics, European Journal of Vascular and Endovascular Surgery 46 (5) (2013) 533–541. doi:10.1016/j.ejvs.2013.09.008.
URL http://dx.doi.org/10.1016/j.ejvs.2013.09.008

[57] M. L. Raghavan, D. A. Vorp, Toward a biomechanical tool to evaluate rupture potential of abdominal aortic aneurysm : identification of a finite strain constitutive model and evaluation of its applicability, Journal of biomechanics 33 (4) (2000) 475–482. doi:10.1016/S0021-9290(99)00201-8.

[58] D. P. Nathan, C. Xu, J. H. Gorman, R. M. Fairman, J. E. Bavaria, R. C. Gorman, K. B. Chandran, B. M. Jackson, Pathogenesis of acute aortic dissection: a finite element stress analysis., The Annals of thoracic surgery 91 (2) (2011) 458–63. doi:10.1016/j.athoracsur.2010.10.042.
URL http://www.ncbi.nlm.nih.gov/pubmed/21256291

[59] L. Speelman, E. M. H. Bosboom, G. W. H. Schurink, J. Buth, M. Breeuwer, M. J. Jacobs, F. N. van de Vosse, Initial stress and nonlinear material behavior in patient-specific AAA wall stress analysis, Journal of Biomechanics 42 (11) (2009) 1713–1719. doi:10.1016/j.jbiomech.2009.04.020.

[60] S. Polzer, T. C. Gasser, J. Bursa, R. Staffa, R. Vlachovsky, V. Man, P. Skacel, Importance of material model in wall stress prediction in abdominal aortic aneurysms, Medical Engineering and Physics 35 (9) (2013) 1282–1289. doi:10.1016/j.medengphy.2013.01.008.
URL http://dx.doi.org/10.1016/j.medengphy.2013.01.008

[61] P. Rissland, Y. Alemu, S. Einav, J. Ricotta, D. Bluestein, Abdominal aortic aneurysm risk of rupture: patient-specific FSI simulations using anisotropic model., Journal of

biomechanical engineering 131 (3) (2009) 31001. doi:10.1115/1.3005200.
URL http://www.ncbi.nlm.nih.gov/pubmed/19154060

[62] K. Y. Volokh, Prediction of arterial failure based on a microstructural bi-layer fiber-matrix model with softening., Journal of biomechanics 41 (2) (2008) 447–53. doi:10.1016/j.jbiomech.2007.08.001.
URL http://www.ncbi.nlm.nih.gov/pubmed/17880984

[63] S. Roccabianca, G. A. Ateshian, J. D. Humphrey, Biomechanical roles of medial pooling of glycosaminoglycans in thoracic aortic dissection, Biomechanics and Modeling in Mechanobiology 13 (1) (2014) 13–25. doi:10.1007/s10237-013-0482-3.

[64] C. J. Beller, M. R. Labrosse, M. J. Thubrikar, F. Robicsek, Role of Aortic Root Motion in the Pathogenesis of Aortic Dissection, Circulation 109 (6) (2004) 763–769. doi:10.1161/01.CIR.0000112569.27151.F7.

[65] A. Tsamis, S. Pal, J. a. Phillippi, T. G. Gleason, S. Maiti, D. a. Vorp, Effect of aneurysm on biomechanical properties of radially-oriented collagen fibers in human ascending thoracic aortic media, Journal of Biomechanics 47 (16) (2014) 3820–3824. doi:10.1016/j.jbiomech.2014.10.024.
URL http://linkinghub.elsevier.com/retrieve/pii/S0021929014005454

[66] S. Pal, A. Tsamis, S. Pasta, A. D'Amore, T. G. Gleason, D. A. Vorp, S. Maiti, A mechanistic model on the role of "radially-running" collagen fibers on dissection properties of human ascending thoracic aorta, Journal of Biomechanics 47 (5) (2014) 981–988. doi:10.1016/j.jbiomech.2014.01.005.
URL http://dx.doi.org/10.1016/j.jbiomech.2014.01.005

[67] C. Martin, W. Sun, T. Pham, J. Elefteriades, Predictive biomechanical analysis of ascending aortic aneurysm rupture potential, Acta Biomaterialia 9 (12) (2013) 9392–9400. doi:10.1016/j.actbio.2013.07.044.
URL http://linkinghub.elsevier.com/retrieve/pii/S1742706113003929

[68] C. Martin, W. Sun, J. Elefteriades, Patient-specific finite element analysis of ascending aorta aneurysms, American Journal of Physiology - Heart and Circulatory Physiology 308 (10) (2015) H1306–H1316. doi:10.1152/ajpheart.00908.2014.
URL http://ajpheart.physiology.org/lookup/doi/10.1152/ajpheart.00908.2014

[69] A. Duprey, O. Trabelsi, M. Vola, J. P. Favre, S. Avril, Biaxial rupture properties of ascending thoracic aortic aneurysms, Acta Biomaterialia 42 (2016) 273–285. doi:10.1016/j.actbio.2016.06.028.
URL http://dx.doi.org/10.1016/j.actbio.2016.06.028

[70] O. Trabelsi, F. M. Davis, J. F. Rodriguez-Matas, A. Duprey, S. Avril, Patient specific stress and rupture analysis of ascending thoracic aneurysms, Journal of Biomechanics

48 (10) (2015) 1836–1843. doi:10.1016/j.jbiomech.2015.04.035.
URL http://dx.doi.org/10.1016/j.jbiomech.2015.04.035

[71] M. Cotrufo, A. Della Corte, L. S. De Santo, C. Quarto, M. De Feo, G. Romano, C. Amarelli, M. Scardone, F. Di Meglio, G. Guerra, M. Scarano, S. Vitale, C. Castaldo, S. Montagnani, Different patterns of extracellular matrix protein expression in the convexity and the concavity of the dilated aorta with bicuspid aortic valve: Preliminary results, Journal of Thoracic and Cardiovascular Surgery 130 (2) (2005) 504–511. doi:10.1016/j.jtcvs.2005.01.016.

[72] S. Pasta, J. a. Phillippi, T. G. Gleason, D. a. Vorp, Effect of aneurysm on the mechanical dissection properties of the human ascending thoracic aorta, Journal of Thoracic and Cardiovascular Surgery 143 (2) (2012) 460–467. doi:10.1016/j.jtcvs.2011.07.058.
URL http://dx.doi.org/10.1016/j.jtcvs.2011.07.058

[73] J. D. Humphrey, M. A. Schwartz, G. Tellides, D. M. Milewicz, Role of mechanotransduction in vascular biology: Focus on thoracic aortic aneurysms and dissections, Circulation Research 116 (8) (2015) 1448–1461. arXiv:15334406, doi:10.1161/CIRCRESAHA.114.304936.

[74] O. Trabelsi, A. Duprey, J. P. Favre, S. Avril, Predictive Models with Patient Specific Material Properties for the Biomechanical Behavior of Ascending Thoracic Aneurysms, Annals of Biomedical Engineering 44 (1) (2016) 84–98. doi:10.1007/s10439-015-1374-8.

[75] J. E. Pichamuthu, J. A. Phillippi, D. A. Cleary, D. W. Chew, J. Hempel, D. A. Vorp, T. G. Gleason, Differential tensile strength and collagen composition in ascending aortic aneurysms by aortic valve phenotype, Annals of Thoracic Surgery 96 (6) (2013) 2147–2154. doi:10.1016/j.athoracsur.2013.07.001.
URL http://dx.doi.org/10.1016/j.athoracsur.2013.07.001

[76] Y. Zou, Y. Zhang, An Experimental and Theoretical Study on the Anisotropy of Elastin Network, Annals of Biomedical Engineering 37 (8) (2009) 1572–1583. doi:10.1007/s10439-009-9724-z.

[77] B. B. Aaron, J. M. Gosline, Elastin as a Random-Network Elastomer: A Mechanical and Optical Analysis of Single Elastin Fibers, Biopolymers 20 (6) (1981) 1247–1260. doi:10.1002/bip.1981.360200611.

[78] M. Lillie, J. Gosline, The viscoelastic basis for the tensile strength of elastin, International Journal of Biological Macromolecules 30 (2) (2002) 119–127. doi:10.1016/S0141-8130(02)00008-9.
URL http://linkinghub.elsevier.com/retrieve/pii/S0141813002000089

[79] H. Miyazaki, K. Hayashi, Tensile tests of collagen fibers obtained from the rabbit patelar tendon, Biomedical Microdevices 2 (2) (1999) 151–157.

[80] Y. C. Fung, Elasticity of soft tissues in simple elongation., The American journal of physiology 213 (6) (1967) 1532–44.
URL http://www.ncbi.nlm.nih.gov/pubmed/6075755

[81] Y. C. Fung, K. Fronek, P. Patitucci, Pseudoelasticity of arteries and the choice of its mathematical expression., The American journal of physiology 237 (5) (1979) H620–31.
URL http://www.ncbi.nlm.nih.gov/pubmed/495769

[82] C. J. Chuong, Y. C. Fung, Three-Dimensional Stress Distribution in Arteries, Journal of Biomechanical Engineering 105 (3) (1983) 268. doi:10.1115/1.3138417.
URL http://biomechanical.asmedigitalcollection.asme.org/article.aspx?articleid=1396295

[83] E. K. Rodriguez, A. Hoger, A. D. McCulloch, D. Carter, W. Hayes, C. Choung, Y. Fung, K. Costa, K. May-Newman, A. McCulloch, J. Omens, S. Cowin, S. Cowin, S. Cowin, S. Cowin, K. Firoozbakhsh, K. Firoozbakhsh, M. Aleyaasin, Y. Fung, B. Gairola, W. Grossman, J. Guccione, A. McCulloch, L. Waldman, X. Guo, S. Cowin, M. Gurtin, H. Han, Y. Fung, T. Harrigan, J. Hamilton, R. Hart, A. Hoger, A. Hoger, A. Hoger, D. Carlson, F. Hsu, E. Kroner, S. Liu, Y. Fung, G. Luo, S. Cowin, A. Sadegh, F. Manasek, C. Mattheck, H. Huber-Betzer, F. Nabarro, J. Omens, J. Covell, J. Omens, Y. Fung, F. Pauwels, E. Rodriguez, J. Omens, O. Mathieu-Costello, A. McCulloch, J. Sadoshima, L. Jahn, T. Takahshi, T. Kulik, S. Izumo, R. Skalak, R. Skalak, G. Dasgupta, M. Moss, E. Otten, P. Dullemeijer, H. Vilmann, A. Spencer, H. Stalsberg, L. Taber, N. Hu, T. Pexieder, E. Clark, B. Keller, K. Takamizawa, K. Hayashi, L. Terracio, A. Tingstorm, W. Peters, T. Borg, J. Xie, S. Liu, R. Yang, Y. Fung, J. Xie, S. Liu, R. Yang, Y. Fung, Stress-dependent finite growth in soft elastic tissues., Journal of biomechanics 27 (4) (1994) 455–67. doi:10.1016/0021-9290(94)90021-3.
URL http://www.ncbi.nlm.nih.gov/pubmed/8188726

[84] G. A. Holzapfel, Determination of material models for arterial walls from uniaxial extension tests and histological structure, Journal of Theoretical Biology 238 (2) (2006) 290–302. doi:10.1016/j.jtbi.2005.05.006.
URL http://linkinghub.elsevier.com/retrieve/pii/S0022519305002080

[85] W. Sun, M. S. Sacks, Finite element implementation of a generalized Fung-elastic constitutive model for planar soft tissues., Biomechanics and modeling in mechanobiology 4 (2-3) (2005) 190–9. doi:10.1007/s10237-005-0075-x.
URL http://www.ncbi.nlm.nih.gov/pubmed/16075264

[86] M. Mooney, A Theory of Large Elastic Deformation, Journal of Applied Physics 11 (9) (1940) 582–592. doi:10.1063/1.1712836.
URL http://aip.scitation.org/doi/10.1063/1.1712836

[87] R. S. Rivlin, Large Elastic Deformations of Isotropic Materials. IV. Further Developments of the General Theory, Philosophical Transactions of the Royal Society A: Mathematical, Physical and Engineering Sciences 241 (835) (1948) 379–397.

doi:10.1098/rsta.1948.0024.
URL http://rsta.royalsocietypublishing.org/cgi/doi/10.1098/rsta.1948.0024

[88] J. A. Weiss, B. N. Maker, S. Govindjee, Finite element implementation of incompressible , transversely isotropic hyperelasticity, Computer Methods in Applied Mechanics and Engineering 135 (1-2) (1996) 107–128.

[89] C. Lally, A. J. Reid, P. J. Prendergast, Elastic behavior of porcine coronary artery tissue under uniaxial and equibiaxial tension, Annals of Biomedical Engineering 32 (10) (2004) 1355–1364. doi:10.1114/B:ABME.0000042224.23927.ce.

[90] D. Bluestein, Y. Alemu, I. Avrahami, M. Gharib, K. Dumont, J. J. Ricotta, S. Einav, Influence of microcalcifications on vulnerable plaque mechanics using FSI modeling, Journal of Biomechanics 41 (5) (2008) 1111–1118. doi:10.1016/j.jbiomech.2007.11.029.
URL http://linkinghub.elsevier.com/retrieve/pii/S0021929007005106

[91] P. P. Purslow, A. Bigi, A. Ripamonti, N. Roveri, Collagen fibre reorientation around a crack in biaxially stretched aortic media, Int. J. Biol. Macromol. 6 (1984) 21–25.

[92] M. S. Sacks, D. B. Smith, E. D. Hiester, A Small Angle Light Scattering Device for Planar Connective Tissue Microstructural Analysis, Annals of Biomedical Engineering 25 (17) (1997) 678–689.

[93] W. Denk, J. H. Strickler, W. W. Webb, Two-photon laser scanning fluorescence microscopy, Science 248 (4951) (1990) 73–76.

[94] G. A. Holzapfel, T. C. Gasser, R. W. Ogden, A New Constitutive Framework for Arterial Wall Mechanics and a Comparative Study of Material Models, Journal of Elasticity 61 (2000) 1–48.

[95] K. Volokh, Hyperelasticity with softening for modeling materials failure, Journal of the Mechanics and Physics of Solids 55 (10) (2007) 2237–2264. doi:10.1016/j.jmps.2007.02.012.
URL http://linkinghub.elsevier.com/retrieve/pii/S0022509607000403

[96] A. Ferrara, A. Pandolfi, Numerical modelling of fracture in human arteries., Computer methods in biomechanics and biomedical engineering 11 (5) (2008) 553–67. doi:10.1080/10255840701771743.
URL http://www.ncbi.nlm.nih.gov/pubmed/19230149

[97] E. Maher, A. Creane, C. Lally, D. J. Kelly, An anisotropic inelastic constitutive model to describe stress softening and permanent deformation in arterial tissue., Journal of the mechanical behavior of biomedical materials 12 (2012) 9–19. doi:10.1016/j.jmbbm.2012.03.001.
URL http://www.ncbi.nlm.nih.gov/pubmed/22659364

[98] D. M. Pierce, F. Maier, H. Weisbecker, C. Viertler, P. Verbrugghe, N. Famaey, I. Fourneau, P. Herijgers, G. A. Holzapfel, Human thoracic and abdominal aortic aneurysmal tissues : Damage experiments, statistical analysis and constitutive modeling, Journal of the Mechanical Behavior of Biomedical Materials 41 (2015) 92–107. doi:10.1016/j.jmbbm.2014.10.003.
URL http://dx.doi.org/10.1016/j.jmbbm.2014.10.003

[99] G. A. Holzapfel, R. W. Ogden, Constitutive modelling of arteries, Proceedings of the Royal Society A: Mathematical, Physical and Engineering Sciences 466 (2118) (2010) 1551–1597. doi:10.1098/rspa.2010.0058.
URL http://rspa.royalsocietypublishing.org/cgi/doi/10.1098/rspa.2010.0058

[100] A. Pandolfi, M. Vasta, Fiber distributed hyperelastic modeling of biological tissues, Mechanics of Materialsdoi:10.1016/j.mechmat.2011.06.004.
URL http://linkinghub.elsevier.com/retrieve/pii/S0167663611000998

[101] H. Weisbecker, M. J. Unterberger, G. A. Holzapfel, Constitutive modelling of arteries considering fibre recruitment and three-dimensional fibre distribution, Journal of The Royal Society Interface 12 (105) (2015) 20150111–20150111. doi:10.1098/rsif.2015.0111.
URL http://rsif.royalsocietypublishing.org/cgi/doi/10.1098/rsif.2015.0111

[102] P. Sáez, E. Peña, M. Doblaré, M. Á. Martínez, An anisotropic microsphere-based approach for fiber orientation adaptation in soft tissue., IEEE transactions on biomedical engineering 58 (12) (2011) 3500–3. doi:10.1109/TBME.2011.2166154.
URL http://www.ncbi.nlm.nih.gov/pubmed/21878407

[103] P. Sáez, A. García, E. Peña, T. C. Gasser, M. A. Martínez, Microstructural quantification of collagen fiber orientations and its integration in constitutive modeling of the porcine carotid artery, Acta Biomaterialia 33 (2016) 183–193. doi:10.1016/j.actbio.2016.01.030.

[104] S. B. Shah, C. Witzenburg, H. P. Wagner, J. M. Goodrich, P. W. Alford, V. H. Barocas, Prefailure and Failure Mechanics of the Porcine Ascending Thoracic Aorta: Experiments and a Multiscale Model, Journal of Biomechanical Engineering 136 (February 2014) (2014) 1–7. doi:10.1115/1.4026443.

[105] T. Stylianopoulos, V. H. Barocas, Multiscale, structure-based modeling for the elastic mechanical behavior of arterial walls., Journal of biomechanical engineering 129 (4) (2007) 611–618. doi:10.1115/1.2746387.

[106] J. R. Thunes, S. Pal, R. N. Fortunato, J. A. Phillippi, T. G. Gleason, D. A. Vorp, S. Maiti, A structural finite element model for lamellar unit of aortic media indicates heterogeneous stress field after collagen recruitment, Journal of Biomechanics 49 (9) (2016) 1562–1569. doi:10.1016/j.jbiomech.2016.03.034.

URL http://dx.doi.org/10.1016/j.jbiomech.2016.03.034http://linkinghub.elsevier.com/retrieve/pii/S0021929016303608

[107] J. O'Rourke, Computational Geometry in C, 2nd Edition, Cambridge University Press, Cambridge, United Kingdom, 1998.

[108] P. L. Chandran, V. H. Barocas, Affine Versus Non-Affine Fibril Kinematics in Collagen Networks: Theoretical Studies of Network Behavior, Journal of Biomechanical Engineering 128 (2) (2005) 259. doi:10.1115/1.2165699.
URL http://biomechanical.asmedigitalcollection.asme.org/article.aspx?doi=10.1115/1.2165699

[109] G. A. Holzapfel, T. C. Gasser, R. W. Ogden, Comparison of a multi-layer structural model for arterial walls with a fung-type model, and issues of material stability., Journal of biomechanical engineering 126 (April 2004) (2004) 264–275. doi:10.1115/1.1695572.

[110] J. B. Carleton, A. D. Amore, K. R. Feaver, G. J. Rodin, M. S. Sacks, Geometric characterization and simulation of planar layered elastomeric fibrous biomaterials, Acta Biomaterialia 12 (2015) 93–101. doi:10.1016/j.actbio.2014.09.049.
URL http://dx.doi.org/10.1016/j.actbio.2014.09.049

[111] S. Polzer, T. Gasser, K. Novak, V. Man, M. Tichy, P. Skacel, J. Bursa, Structure-based constitutive model can accurately predict planar biaxial properties of aortic wall tissue, Acta Biomaterialia 14 (2015) 133–145. doi:10.1016/j.actbio.2014.11.043.
URL http://linkinghub.elsevier.com/retrieve/pii/S1742706114005467

[112] R. C. Picu, Mechanics of random fiber networksa review, Soft Matter 7 (15) (2011) 6768. arXiv:79960787636, doi:10.1039/c1sm05022b.

[113] F. Cacho, P. Elbischger, J. Rodríguez, M. Doblaré, G. A. Holzapfel, A constitutive model for fibrous tissues considering collagen fiber crimp, International Journal of Non-Linear Mechanics 42 (2) (2007) 391–402. doi:10.1016/j.ijnonlinmec.2007.02.002.
URL http://linkinghub.elsevier.com/retrieve/pii/S0020746207000558

[114] M. R. Hill, X. Duan, G. A. Gibson, S. Watkins, A. M. Robertson, A theoretical and non-destructive experimental approach for direct inclusion of measured collagen orientation and recruitment into mechanical models of the artery wall, Journal of Biomechanics 45 (5) (2012) 762–771. doi:10.1016/j.jbiomech.2011.11.016.
URL http://linkinghub.elsevier.com/retrieve/pii/S0021929011006981

[115] J. Ferruzzi, D. A. Vorp, J. D. Humphrey, On constitutive descriptors of the biaxial mechanical behaviour of human abdominal aorta and aneurysms., Journal of the Royal Society, Interface / the Royal Society 8 (56) (2011) 435–450. doi:10.1098/rsif.2010.0299.

[116] T. C. Gasser, R. W. Ogden, G. A. Holzapfel, Hyperelastic modelling of arterial layers with distributed collagen fibre orientations., Journal of the Royal Society, Interface / the Royal Society 3 (6) (2006) 15–35. doi:10.1098/rsif.2005.0073.
URL http://www.pubmedcentral.nih.gov/articlerender.fcgi?artid=1618483{&}tool=pmcentrez{&}rendertype=abstract

[117] W. Wan, J. B. Dixon, R. L. Gleason, Constitutive modeling of mouse carotid arteries using experimentally measured microstructural parameters, Biophysical Journal 102 (12) (2012) 2916–2925. doi:10.1016/j.bpj.2012.04.035.
URL http://dx.doi.org/10.1016/j.bpj.2012.04.035

[118] M. a. Zulliger, N. Stergiopulos, Structural strain energy function applied to the ageing of the human aorta, Journal of Biomechanics 40 (14) (2007) 3061–3069. doi:10.1016/j.jbiomech.2007.03.011.

[119] A. D'Amore, J. A. Stella, W. R. Wagner, M. S. Sacks, Characterization of the complete fiber network topology of planar fibrous tissues and scaffolds, Biomaterials 31 (20) (2010) 5345–5354. doi:10.1016/j.biomaterials.2010.03.052.
URL http://dx.doi.org/10.1016/j.biomaterials.2010.03.052

[120] G. A. Holzapfel, J. A. Niestrawska, R. W. Ogden, A. J. Reinisch, A. J. Schriefl, Modelling non-symmetric collagen fibre dispersion in arterial walls, Journal of The Royal Society Interface 12. doi:10.1098/rsif.2015.0188.

[121] A. D'Amore, N. Amoroso, R. Gottardi, C. Hobson, C. Carruthers, S. Watkins, W. R. Wagner, M. S. Sacks, From single fiber to macro-level mechanics: A structural finite-element model for elastomeric fibrous biomaterials, Journal of the Mechanical Behavior of Biomedical Materials 39 (2014) 146–161. doi:10.1016/j.jmbbm.2014.07.016.
URL http://linkinghub.elsevier.com/retrieve/pii/S1751616114002094

[122] C. M. Witzenburg, R. Y. Dhume, S. B. Shah, C. E. Korenczuk, H. P. Wager, P. W. Alford, V. H. Barocas, Failure of the Porcine Ascending Aorta: Multidirectional Experiments and a Unifying Microstructural Model, Journal of Biomechanical Engineeringdoi:10.1115/1.4035264.

[123] J. Thunes, R. Matthew Miller, S. Pal, S. Damle, R. E. Debski, S. Maiti, The Effect of Size and Location of Tears in the Supraspinatus Tendon on Potential Tear Propagation, Journal of Biomechanical Engineering 137 (8) (2015) 081012. doi:10.1115/1.4030745.
URL http://biomechanical.asmedigitalcollection.asme.org/article.aspx?doi=10.1115/1.4030745

[124] J. Ahrens, B. Geveci, C. Law, ParaView: An End-User Tool for Large Data Visualization, Elsevier, 2005.

[125] Y.-C. Fung, Biomechanics: Mechanical Properties of Living Tissue, 2nd Edition, Springer-Verlag, New York, 1993.

[126] G. Žagar, P. Onck, E. vanderGiessen, Two Fundamental Mechanisms Govern the Stiffening of Cross-linked Networks, Biophysical Journal 108 (6) (2015) 1470–1479. doi:10.1016/j.bpj.2015.02.015.
URL http://linkinghub.elsevier.com/retrieve/pii/S0006349515001782

[127] A. Benninghoff, Uber die Beziehungen zwischen elastichen Gerust und glatter Muskulatur in der Arterienwand und ihre funktionelle Bedeutung, Z. Zellforsch. Mikroskop. Anat. Abt. Histochem. 6 (1928) 348.

[128] L. Zhang, S. P. Lake, V. K. Lai, C. R. Picu, V. H. Barocas, M. S. Shephard, A Coupled Fiber-Matrix Model Demonstrates Highly Inhomogeneous Microstructural Interactions in Soft Tissues Under Tensile Load, Journal of Biomechanical Engineering 135 (January 2013) (2012) 011008. doi:10.1115/1.4023136.
URL http://biomechanical.asmedigitalcollection.asme.org/article.aspx?doi=10.1115/1.4023136

[129] L. Zhang, S. P. Lake, V. H. Barocas, M. S. Shephard, R. C. Picu, Cross-linked fiber network embedded in an elastic matrix, Soft Matter 9 (2013) 6398–6405. doi:10.1039/c3sm50838b.

[130] S. P. Lake, M. F. Hadi, V. K. Lai, V. H. Barocas, Mechanics of a fiber network within a non-fibrillar matrix: Model and comparison with collagen-agarose co-gels, Annals of Biomedical Engineering 40 (10) (2012) 2111–2121. doi:10.1007/s10439-012-0584-6.

[131] J. H. Haga, Y.-S. J. Li, S. Chien, Molecular basis of the effects of mechanical stretch on vascular smooth muscle cells, Journal of Biomechanics 40 (5) (2007) 947–960. doi:10.1016/j.jbiomech.2006.04.011.
URL http://linkinghub.elsevier.com/retrieve/pii/S0021929006001436

[132] K. B. Acampora, J. Nagatomi, E. M. Langan, M. LaBerge, Increased Synthetic Phenotype Behavior of Smooth Muscle Cells in Response to In Vitro Balloon Angioplasty Injury Model, Annals of Vascular Surgery 24 (1) (2010) 116–126. doi:10.1016/j.avsg.2009.07.019.
URL http://linkinghub.elsevier.com/retrieve/pii/S0890509609001642

[133] C. Forsell, H. M. Björck, P. Eriksson, A. Franco-Cereceda, T. C. Gasser, Biomechanical Properties of the Thoracic Aneurysmal Wall: Differences Between Bicuspid Aortic Valve and Tricuspid Aortic Valve Patients, The Annals of Thoracic Surgery 98 (1) (2014) 65–71. doi:10.1016/j.athoracsur.2014.04.042.
URL http://linkinghub.elsevier.com/retrieve/pii/S0003497514008261

[134] D. P. Sokolis, E. P. Kritharis, A. T. Giagini, K. M. Lampropoulos, S. A. Papadodima, D. C. Iliopoulos, Biomechanical response of ascending thoracic aortic aneurysms: association with structural remodelling, Computer Methods in Biomechanics and Biomedical Engineering 15 (3) (2012) 231–248. doi:10.1080/10255842.2010.522186.
URL http://www.tandfonline.com/doi/abs/10.1080/10255842.2010.522186

[135] J. R. Thunes, J. A. Phillippi, T. G. Gleason, D. A. Vorp, S. Maiti, Structural Modeling Reveals Microstructure-Strength Relationship for Human Ascending Thoracic Aorta, Journal of Biomechanics (2018) 1–10doi:10.1016/j.jbiomech.2018.01.037.
URL http://linkinghub.elsevier.com/retrieve/pii/S0021929018300745

[136] R. A. Nishimura, C. M. Otto, R. O. Bonow, B. A. Carabello, J. P. Erwin, R. A. Guyton, P. T. O'Gara, C. E. Ruiz, N. J. Skubas, P. Sorajja, 2014 AHA / ACC Guideline for the Management of Patients With Valvular Heart Disease A Report of the American College of Cardiology / American Heart Association Task Force on Practice Guidelines, Circulation 129 (23) (2014) e521–643. doi:10.1161/CIR.0000000000000031/-/DC1.The.

[137] L. G. Svensson, D. H. Adams, R. O. Bonow, N. T. Kouchoukos, D. C. Miller, P. T. O'Gara, D. M. Shahian, H. V. Schaff, C. W. Akins, J. Bavaria, E. H. Blackstone, T. E. David, N. D. Desai, T. M. Dewey, R. S. D'Agostino, T. G. Gleason, K. B. Harrington, S. Kodali, S. Kapadia, M. B. Leon, B. Lima, B. W. Lytle, M. J. Mack, T. B. Reece, G. R. Reiss, E. Roselli, C. R. Smith, V. H. Thourani, E. M. Tuzcu, J. Webb, M. R. Williams, Aortic Valve and Ascending Aorta Guidelines for Management and Quality Measures: Executive Summary, The Annals of Thoracic Surgery 95 (4) (2013) 1491–1505. doi:https://doi.org/10.1016/j.athoracsur.2012.12.027.
URL http://www.sciencedirect.com/science/article/pii/S0003497512028780

[138] D. P. Sokolis, E. M. Kefaloyannis, M. Kouloukoussa, E. Marinos, H. Boudoulas, P. E. Karayannacos, A structural basis for the aortic stress-strain relation in uniaxial tension, Journal of Biomechanics 39 (9) (2006) 1651–1662. doi:10.1016/j.jbiomech.2005.05.003.

[139] N. Shahmansouri, M. Alreshidan, A. Emmott, K. Lachapelle, R. Cartier, R. L. Leask, R. Mongrain, Evaluating ascending aortic aneurysm tissue toughness: Dependence on collagen and elastin contents, Journal of the Mechanical Behavior of Biomedical Materials 64 (2016) 262–271. doi:10.1016/j.jmbbm.2016.08.006.
URL http://linkinghub.elsevier.com/retrieve/pii/S1751616116302636

[140] M. L. Raghavan, M. W. Webster, D. A. Vorp, Ex vivo biomechanical behavior of abdominal aortic aneurysm: Assessment using a new mathematical model, Annals of Biomedical Engineering 24 (5) (1996) 573–582. doi:10.1007/BF02684226.
URL http://link.springer.com/10.1007/BF02684226

[141] A. J. Schriefl, T. Schmidt, D. Balzani, G. Sommer, G. A. Holzapfel, Selective enzymatic removal of elastin and collagen from human abdominal aortas: Uniaxial mechanical response and constitutive modeling, Acta Biomaterialia 17 (2015) 125–136. doi:10.1016/j.actbio.2015.01.003.
URL http://linkinghub.elsevier.com/retrieve/pii/S1742706115000045

[142] A. Ferrara, S. Morganti, P. Totaro, A. Mazzola, F. Auricchio, Human dilated ascending aorta: Mechanical characterization via uniaxial tensile tests, J Mech Behav Biomed

Mater 53 (2016) 257–71.
URL https://www-ncbi-nlm-nih-gov.proxy.library.uu.nl/pubmed/?term=Ferrara{%}2C+A.{%}2C+Morganti{%}2C+S.{%}2C+Totaro{%}2C+P.{%}2C+Mazzola{%}2C+A.{%}2C+{%}26+Auricchio{%}2C+F

[143] P. Sáez, V. Alastrué, E. Peña, M. Doblaré, M. A. Martínez, Anisotropic microsphere-based approach to damage in soft fibered tissue., Biomechanics and modeling in mechanobiology 11 (5) (2012) 595–608. doi:10.1007/s10237-011-0336-9.
URL http://www.ncbi.nlm.nih.gov/pubmed/21769621

[144] C. Forsell, J. Swedenborg, J. Roy, T. C. Gasser, The quasi-static failure properties of the abdominal aortic aneurysm wall estimated by a mixed experimental-numerical approach, Annals of Biomedical Engineering 41 (7) (2013) 1554–1566. doi:10.1007/s10439-012-0711-4.

[145] T. C. Gasser, An irreversible constitutive model for fibrous soft biological tissue: a 3-D microfiber approach with demonstrative application to abdominal aortic aneurysms., Acta biomaterialia 7 (6) (2011) 2457–66. doi:10.1016/j.actbio.2011.02.015.
URL http://www.ncbi.nlm.nih.gov/pubmed/21338718

[146] G. Sommer, T. C. Gasser, P. Regitnig, M. Auer, G. A. Holzapfel, Dissection Properties of the Human Aortic Media: An Experimental Study, Journal of Biomechanical Engineering 130 (2) (2008) 021007. doi:10.1115/1.2898733.
URL http://biomechanical.asmedigitalcollection.asme.org/article.aspx?articleid=1475489

[147] A. J. Schriefl, G. Zeindlinger, D. M. Pierce, P. Regitnig, G. A. Holzapfel, Determination of the layer-specific distributed collagen fibre orientations in human thoracic and abdominal aortas and common iliac arteries., Journal of the Royal Society, Interface / the Royal Society 9 (71) (2012) 1275–1286. doi:10.1098/rsif.2011.0727.
URL http://www.ncbi.nlm.nih.gov/pubmed/22171063

[148] S. Maiti, P. H. Geubelle, Mesoscale modeling of dynamic fracture of ceramic materials, Computer Modeling in Engineering and Sciences 5 (2) (2004) 91–102.
URL http://www.me.mtu.edu/{~}spandan/index{_}files/cmes.pdf

[149] S. Roccabianca, C. Bellini, J. D. Humphrey, Computational modelling suggests good, bad and ugly roles of glycosaminoglycans in arterial wall mechanics and mechanobiology, Journal of The Royal Society Interface 11 (97) (2014) 20140397–20140397. doi:10.1098/rsif.2014.0397.
URL http://rsif.royalsocietypublishing.org/cgi/doi/10.1098/rsif.2014.0397

[150] F. Robicsek, M. J. Thubrikar, Hemodynamic considerations regarding the mechanism and prevention of aortic dissection, The Annals of Thoracic Surgery 58 (4) (1994) 1247–1253. doi:10.1016/0003-4975(94)90523-1.
URL http://linkinghub.elsevier.com/retrieve/pii/0003497594905231

[151] M. J. Thubrikar, P. Agali, F. Robicsek, Wall stress as a possible mechanism for the development of transverse intimal tears in aortic dissections., Journal of medical engineering & technology 23 (4) (1999) 127–34.
URL http://www.ncbi.nlm.nih.gov/pubmed/10561823

[152] C. J. Beller, M. R. Labrosse, M. J. Thubrikar, F. Robicsek, Finite element modeling of the thoracic aorta: including aortic root motion to evaluate the risk of aortic dissection, Journal of Medical Engineering & Technology 32 (2) (2008) 167–170. doi:10.1080/03091900600687672.
URL http://www.tandfonline.com/doi/full/10.1080/03091900600687672

[153] D. C. Iliopoulos, R. P. Deveja, E. P. Kritharis, D. Perrea, G. D. Sionis, K. Toutouzas, C. Stefanadis, D. P. Sokolis, Regional and directional variations in the mechanical properties of ascending thoracic aortic aneurysms, Medical Engineering and Physics 31 (1) (2009) 1–9. doi:10.1016/j.medengphy.2008.03.002.

[154] I. M. Daniel, O. Ishai, Engineering Mechanics of Composite Materials, no. v. 13 in Engineering mechanics of composite materials, Oxford University Press, 2006.
URL https://books.google.com/books?id=x5S{_}QgAACAAJ

[155] J. S. Wilson, S. Baek, J. D. Humphrey, Importance of initial aortic properties on the evolving regional anisotropy, stiffness and wall thickness of human abdominal aortic aneurysms, Journal of The Royal Society Interface 9 (2012) 2047–2058. doi:10.1098/rsif.2012.0097.

[156] C. Bellini, N. J. Kristofik, M. R. Bersi, T. R. Kyriakides, J. D. Humphrey, A hidden structural vulnerability in the thrombospondin-2 deficient aorta increases the propensity to intramural delamination, Journal of the Mechanical Behavior of Biomedical Materials 71 (2017) 397–406. doi:https://doi.org/10.1016/j.jmbbm.2017.01.045.
URL http://www.sciencedirect.com/science/article/pii/S1751616117300504

[157] D. Mohan, J. W. Melvin, Failure properties of passive human aortic tissue. II-Biaxial tension tests, Journal of Biomechanics 16 (1). doi:10.1016/0021-9290(83)90044-1.

[158] J. M. Clark, S. Glagov, Structural integration of the arterial wall. I. Relationships and attachments of medial smooth muscle cells in normally distended and hyperdistended aortas., Laboratory investigation; a journal of technical methods and pathology 40 (6) (1979) 587–602.

[159] S. Krag, T. Olsen, T. T. Andreassen, Biomechanical characteristics of the human anterior lens capsule in relation to age., Investigative ophthalmology & visual science 38 (2) (1997) 357–63.
URL http://www.ncbi.nlm.nih.gov/pubmed/9040468

[160] E. J. Koay, G. Ofek, K. A. Athanasiou, Effects of TGF-β1 and IGF-I on the compressibility, biomechanics, and strain-dependent recovery behavior of single chondrocytes,

Journal of Biomechanics 41 (5) (2008) 1044–1052. doi:10.1016/j.jbiomech.2007.12.006.

[161] T. J. Schlatmann, A. E. Becker, Histologic changes in the normal aging aorta: Implications for dissecting aortic aneurysm, The American Journal of Cardiology 39 (1) (1977) 13–20. doi:10.1016/S0002-9149(77)80004-0.
URL http://linkinghub.elsevier.com/retrieve/pii/S0002914977800040

[162] M. F. Fillinger, M. L. Raghavan, S. P. Marra, J. L. Cronenwett, F. E. Kennedy, In vivo analysis of mechanical wall stress and abdominal aortic aneurysm rupture risk, Journal of Vascular Surgery 36 (3) (2002) 589–597. doi:10.1067/mva.2002.125478.

[163] A. Maier, M. W. Gee, C. Reeps, J. Pongratz, H. H. Eckstein, W. A. Wall, A comparison of diameter, wall stress, and rupture potential index for abdominal aortic aneurysm rupture risk prediction, Annals of Biomedical Engineering 38 (10) (2010) 3124–3134. doi:10.1007/s10439-010-0067-6.

[164] T. Belytschko, W. K. Lui, B. Moran, Nonlinear Finite Elements for Continua and Structures, John Wiley and Sons, 2000.

[165] R. L. Taylor, E. Oñate, P.-A. Ubach, Finite Element Analysis of Membrane Structures, Computational Methods in Applied Sciences 3 (2005) 47–68. doi:10.1007/1-4020-3317-6_4.
URL http://www.springerlink.com/index/10.1007/1-4020-3317-6

[166] H. W. de Beaufort, F. J. Nauta, M. Conti, E. Cellitti, C. Trentin, E. Faggiano, G. H. van Bogerijen, C. A. Figueroa, F. L. Moll, J. A. van Herwaarden, F. Auricchio, S. Trimarchi, Extensibility and Distensibility of the Thoracic Aorta in Patients with Aneurysm, European Journal of Vascular and Endovascular Surgery 53 (2) (2017) 199–205. doi:10.1016/j.ejvs.2016.11.018.
URL http://dx.doi.org/10.1016/j.ejvs.2016.11.018

[167] A. Wittek, K. Karatolios, C. P. Fritzen, J. Bereiter-Hahn, B. Schieffer, R. Moosdorf, S. Vogt, C. Blase, Cyclic three-dimensional wall motion of the human ascending and abdominal aorta characterized by time-resolved three-dimensional ultrasound speckle tracking, Biomechanics and Modeling in Mechanobiology 15 (5) (2016) 1375–1388. doi:10.1007/s10237-016-0769-2.

[168] V. Bell, W. A. Mitchell, S. Sigurdsson, J. J. Westenberg, J. D. Gotal, A. A. Torjesen, T. Aspelund, L. J. Launer, A. de Roos, V. Gudnason, T. B. Harris, G. F. Mitchell, Longitudinal and circumferential strain of the proximal aorta, Journal of the American Heart Association 3 (6) (2014) 1–12. doi:10.1161/JAHA.114.001536.

[169] P. H. Geubelle, J. S. Baylor, Impact-induced delamination of composites: a 2D simulation, Composites Part B: Engineering 29 (5) (1998) 589–602. doi:10.1016/S1359-8368(98)00013-4.
URL http://linkinghub.elsevier.com/retrieve/pii/S1359836898000134

[170] G. A. Holzapfel, Nonlinear Solid Mechanics: A Continuum Approach for Engineering, Wiley, 2000.

[171] J. P. Vande Geest, D. H. J. Wang, S. R. Wisniewski, M. S. Makaroun, D. A. Vorp, Towards A Noninvasive Method for Determination of Patient-Specific Wall Strength Distribution in Abdominal Aortic Aneurysms, Annals of biomedical engineering 34 (7) (2006) 1098–1106. doi:10.1007/s10439-006-9132-6.